The University Of Sheffield.

Access To Thesis.

- A bound copy of every thesis which is accepted as worthy for a higher degree, must be deposited in the University of Sheffield Library, where it will be made available for borrowing or consultation in accordance with University Regulations.
- All students registering from 2008–09 onwards are also required to submit an electronic copy of their final, approved thesis. Students who registered prior to 2008–09 may also submit electronically, but this is not required.

Author: MATTHEW JAMES HOBBS Dept: EEE

Thesis Title: INFRARED DETECTORS FOR RADIATION THERMOMETRY Registration No: 090140756

For completion by all students:

Submit in print form only (for deposit in the University Library): ☐

Submit in print form and also upload to the *White Rose eTheses Online* server: In full ☑

Edited eThesis ☐

Please indicate if there are any embargo restrictions on this thesis. Please note that if no boxes are ticked, you will have consented to your thesis being made available without any restrictions.

Embargo details: (complete only if requesting an embargo to either your print and/or eThesis)	Embargo required?		Length of embargo (in years)
Print Thesis	Yes ☐	No ☑	_____
eThesis	Yes ☐	No ☑	_____

Supervisor: I, the supervisor, agree to the named thesis being made available under the conditions specified above.

Name: CHEE HING TAN Dept: EEE

Signed: C H TAN Date: 13/02/14

Student: I, the author, agree to the named thesis being made available under the conditions specified above.

I give permission to the University of Sheffield to reproduce the print thesis in whole or in part in order to supply single copies for the purpose of research or private study for a non-commercial purpose.

I confirm that this thesis is my own work, and where materials owned by a third party have been used copyright clearance has been obtained. I am aware of the University's *Guidance on the Use of Unfair Means* (www.sheffield.ac.uk/lets/design/unfair)

I confirm that all copies of the thesis submitted to the University (including electronic copies on CD/DVD) are identical in content.

Name: MATTHEW JAMES HOBBS Dept: EEE

Signed: M HOBBS Date: 20/02/14

For completion by students also submitting an electronic thesis (eThesis):

I, the author, agree that the University of Sheffield's eThesis repository (currently WREO) will make my eThesis available over the internet via an entirely non-exclusive agreement and that, without changing content, WREO may convert my thesis to any medium or format for the purpose of future preservation and accessibility.

I, the author, agree that the metadata relating to the eThesis will normally appear on both the University's eThesis server and the British Library's EThOS service, even if the thesis is subject to an embargo. I agree that a copy of the eThesis may be supplied to the British Library.

I confirm that the upload is identical to the final, examined and awarded version of the thesis as submitted in print to the University for deposit in the Library (unless edited as indicated above).

Name: MATTHEW JAMES HOBBS Dept: EEE

Signed: M HOBBS Date: 20/02/14

THIS SHEET MUST BE BOUND IN THE FRONT OF THE PRINTED THESIS BEFORE IT IS SUBMITTED

Infrared Detectors for Radiation Thermometry

Matthew James Hobbs

A thesis submitted for the degree of Doctor of Philosophy

Department of Electronic and Electrical Engineering

The University of Sheffield

August 2014

Contents

Abstract

This work presents an investigation into the potential next generation of infrared detectors for radiation thermometry. Motivations for this work include increased detector sensitivity, development of minimally cooled mid-wave infrared (MWIR) arrays and longer wavelength multi-colour ratio radiation thermometers.

The high sensitivity of the Si avalanche photodiode (APD) is highly attractive for radiation thermometry. A Si APD is shown to offer increased sensitivity by measuring a lower temperature than a Si photodiode in order to satisfy specific threshold voltages. The Si APD is also shown to offer improvement in the signal-to-noise ratio (SNR) and temperature error. By combining the Si APD with a phase sensitive detection (PSD) method, further improvement is achieved.

The MWIR InAs/GaSb type-II superlattice (T2SL) offers the potential development of minimally cooled MWIR arrays for radiation thermometry, as well as longer wavelength multi-colour detectors for ratio radiation thermometry. An uncooled T2SL detector on a GaSb substrate is demonstrated for measurement of a target temperature of 25 ^{o}C with SNR > 1. Cooling improves the detector's performance, allowing operation at the thermo-electric cooler compatible temperature of 200 K. Further characterisation of a T2SL detector on a GaAs substrate demonstrates similar temperature dependence, suggesting challenges to the material growth for improved detector performance. Other potential challenges with T2SL development are identified and discussed.

The quantum dot infrared photodetector (QDIP) also offers the potential for longer wavelength multi-colour detection. Combination with an infrared algorithmic spectrometer (IRAS) offers flexibility for development of a versatile ratio radiation thermometer. The QDIP-IRAS combination is demonstrated to successfully reproduce arbitrary filter shapes from blackbody photocurrent measurements. Ratios computed using the IRAS correspond well with ratios computed from the arbitrary target filters.

Acknowledgements

I would like to thank my supervisor Prof. Chee Hing Tan for his support and guidance throughout my PhD studies. His comments during the writing stages of my publications and thesis I am particularly thankful for, and the time he has given to helping me. I would like to thank Prof. John David for introducing me and encouraging me in the area of photodiode research as well as his constant interest in my development. I would like to thank Dr. Jon Willmott for his valuable input and knowledge of radiation thermometry, helping me to understand how my research fits into applications outside of academia.

I am grateful for the assistance of Dr. Peter Vines and Dr. Sankha Dip Das during the early stages of my research, and I would like to acknowledge Xinxin Zhou, Dr. Yu Ling Goh and Syahrin Idris for fabrication of wafers in Chapter 5, Chapter 6 and Chapter 7, respectively. I am grateful for the support and friendship of all the members of the group; Dr. Jo Shien Ng, Dr. Pin Jern Ker, Dr. Jingjing Xie, Dr. Rajiv Gomes, Dr. James Green, Dr. Daniel Ong, Dr. Ian Sandall, Dr. Siew Li Tan, Dr. Andrew Marshall, Dr. Shiyu Xie, Dr. Jennifer Ong, Dr. Rahman Mohmad, Akeel, Xiao, Benjamin, Simon, Jeng Shiuh and Graham.

I would like to thank Hilary Levesley for helping with some of the practicalities during my studies. I acknowledge the EPSRC for my personal funding which enabled me to carry out my studies. I also acknowledge University of Sheffield KTA (R/131314) projects and MOD contract FTS2//DTICWN/09 for providing resources.

I would like to thank my family, especially my parents, for encouragement and support throughout my time in Sheffield. I would like to thank my friends at Christ Church Fulwood, and would like to thank Melanie Skilbeck especially for proof reading my thesis. I thank you for all your support and prayers throughout my studies, but particularly during my writing up period.

Publications

Journal publications

1. C. H. Tan, P. Vines, **M. Hobbs**, B. Anderson, M. Hugues, and J. David, "Implementation of an algorithmic spectrometer using Quantum Dot Infrared Photodetectors," *Infrared Physics & Technology,* vol. 54, pp. 228-232, 2011.

2. **M. J. Hobbs**, C. H. Tan, and J. R. Willmott, "Evaluation of phase sensitive detection method and Si avalanche photodiode for radiation thermometry," *Journal of Instrumentation,* vol. 8, p. P03016, 2013.

3. **M. J. Hobbs**, F. Bastiman, C. H. Tan, J. P. R. David, S. Krishna, and E. Plis, "Uncooled MWIR InAs/GaSb type-II superlattice grown on a GaAs substrate," *Proc. SPIE, Emerging Technologies in Security and Defence; and Quantum Security II; and Unmanned Sensor Systems X,* vol. 8899, p. 889906, 2013.

4. X. Zhou, **M. J. Hobbs**, B. S. White, J. P. David, J. R. Willmott and C. H. Tan, "An InGaAlAs-InGaAs two colour photodetector for ratio thermometry," *IEEE Transactions on Electron Devices,* vol. 61, pp. 838-843, 2014.

5. **M. J. Hobbs**, C. H. Tan, X. Zhou, J. P. David, J. R. Willmott, E. Plis and S. Krishna, "InAs/GaSb type-II superlattice for radiation thermometry," *Accepted for publication in IEEE Transactions on Instrumentation and Measurement on* 19th June 2014.

Conferences

1. **M. Hobbs**, J. Xie, P. Vines, M. Hugues, J. P. R. David and C. H. Tan, "Temperature dependence of quantum dot infrared photodetectors with variable dot doping", *UK Compound Semiconductors Conference*, Sheffield, UK, July 2010.

2. P. Vines, **M. Hobbs**, J. Xie, B. Anderson, M. Hugues, J. P. David and C. H. Tan, "IR sensing using an algorithm based spectrometer", *EMRS DTC 7th Annual Conf. Proc.*, Edinburgh, UK, July 2010.

3. **M. J. Hobbs**, C. H. Tan, S. D. Das, J. P. R. David, S. Krishna, J. B. Rodriguez and E. Plis, "High detectivity MWIR type-II superlattice grown on a GaAs substrate", *IEEE Photonics Conference*, Arlington, Virginia, USA, October 2011.

4. **M. J. Hobbs**, S. D. Das, J. E. Green, J. P. David, C. H. Tan, S. Krishna, E. Plis and J. Willmott, "Uncooled GaSb/InAs type-II superlattice photodiode for radiation thermometry", *Photon 12 Conference*, Durham, UK, September 2012.

5. X. Zhou, I. Sandall, **M. J. Hobbs**, B. White and C. H. Tan, "InAs photodiode for radiation thermometry", *Semiconductor and Integrated Opto-electronics (SIOE) Conference*, Cardiff, UK, April 2013.

6. C. H. Tan, I. Sandall, X. Zhou, B. White, **M. Hobbs**, and J. P. R. David, "Mid-infrared detectors at Sheffield", *UK Compound Semiconductors Conference*, Sheffield, UK, July 2013.

Glossary of terms

$\%/^oC$	Percentage change for a 1 ^oC rise in the target object's temperature
$\%_{error}$	Percentage error in thermometer output
φ	Angle of incidence
1D	1-dimensional
2D	2-dimensional
3D	3-dimensional
A	Detector area
$\boldsymbol{A}$	IRAS QDIP responsivity matrix
$A(0)$	Absorption at a thickness of 0 cm
$A(x)$	Absorption at a thickness of x cm
AC	Alternating current
ADC	Analogue-to-digital converter
APD	Avalanche photodiode
C	Capacitance
c	Speed of light (3×10^8 m s^{-1})
c_1	Planck's first blackbody constant ($2\pi hc^2 = 1.1910 \times 10^{-16}$ W.m^2.sr^{-1})
c_2	Planck's second blackbody constant ($hc/k = 1.4388 \times 10^{-2}$ m.K)
CV	Capacitance-voltage
D	Distance between blackbody and photodiode
D*	Specific detectivity
DC	Direct current
DD	Direct detection
DWELL	Dot-in-a-well
E	Photon energy
E_A	Activation energy
E_C	Band diagram conduction band
$E_{continuum}$	Continuum level energy
$E_{excited}$	Higher excited energy state

E_g	Bandgap
E_{ground}	Ground energy state
ENF	Excess noise factor
E_V	Band diagram valance band
f	Frequency
F	Magnification factor of lens
FOV	Field of view
FPA	Focal plane array
FTIR	Fourier transform infrared
FWHM	Full-width half maximum
G	Circuit gain
g	Photoconductive gain
g-r	Generation-recombination
h	Planck's constant (6.626×10^{-34} m^2 kg s^{-1})
$\hbar$	Reduced Planck constant ($h/2\pi$ m^2 kg s^{-1})
I / *Perimeter*	Current over perimeter
I_d	Dark current
$I_{diffusion}$	Diffusion current
I_F	Forward current
$i_{g\text{-}r}$	Generation-recombination current
IMF	Interfacial misfit dislocations
$i_{n\ g\text{-}r}$	Generation-recombination noise
$i_{n\ shot}$	Shot noise
$i_{n\ thermal}$	Thermal noise
$i_{n\ total}$	Total noise
I_o	Saturation current
I_{ph}	Photocurrent
IR	Infrared
IRAS	Infrared algorithmic spectrometer
$I_{tunnelling}$	Tunnelling current
IV	Current-voltage

J	Dark current density
j	Square root of -1
k	Boltzmann constant (1.381×10^{-23} m^2 kg s^{-2} K^{-1})
L	Number of wavelength points in IRAS
LCR	Inductance-capacitance-impedance
LWF	Longer wavelength filter
LWIR	Long-wave infrared
$L_{\lambda 1}$	Radiance over spectral range of first wavelength band in two-colour detector
$L_{\lambda 2}$	Radiance over spectral range of second wavelength band in two-colour detector
M	Multiplication factor
m^*	Electron effective mass
MCT	HgCdTe
M_F	Chopper modulation factor
ML	Monolayer
MSE	Mean square error
MWIR	Mid-wave infrared
n	Ideality factor
N	Number of bias voltages in IRAS
N_a	Effective carrier concentration
NEDT	Noise equivalent differential temperature
NEP	Noise equivalent power
n_i	Intrinsic carrier concentration
NIR	Near infrared
$P(\lambda)$	Power per unit wavelength
PCB	Printed circuit board
PSD	Phase sensitive detection
q	Electron charge (1.602×10^{-19} C)
QD	Quantum dot
QDIP	Quantum dot infrared photodetector
QW	Quantum well

QWIP	Quantum well infrared photodiode
$\boldsymbol{R}$	IRAS arbitrary spectral shape vector
r	Reflectivity of photodiode material surface
R	Responsivity in IRAS
$R(\lambda)$	Responsivity as function of wavelength
R_0	Resistance
$\text{Ratio}_{\text{IRAS}}$	Ratio computed from IRAS
$\text{Ratio}_{\text{Target}}$	Ratio computed from target triangular filters
R_p	Peak responsivity
$\boldsymbol{R_{rep}}$	IRAS filter reproduction
RTD	Resistive temperature device
SLS	Strained layer superlattice
SMU	Source measurement unit
SNR	Signal-to-noise ratio
SPAD	Single photon avalanche diode
SRH	Shockley-Read-Hall
SWF	Shorter wavelength filter
SWIR	Short-wave infrared
T	Thermodynamic temperature
t	Time
T2SL	Type-II superlattice
T_{BB}	Blackbody temperature
T_F	Transmission factor
TIA	Transimpedance amplifier
TO	Transistor outline
T-QDIP	Tunnelling quantum dot infrared photodiode
V	Voltage
V_B	Diode built in voltage
VLWIR	Very-long wave infrared
V_M	PSD measured signal magnitude
V_{mean}	Mean output voltage
$V_{pk\text{-}pk}$	Peak-to-peak fluctuation in output voltage

V_R	DC reverse bias voltage
V_{REF}	PSD reference signal magnitude
w	IRAS calculated weights
W	Depletion region width
$\boldsymbol{w}$	IRAS weighting factor vector
$W(\lambda)$	Power per unit wavelength, per unit area
x	Absorption region thickness in cm
XRD	x-ray diffraction
α	Electron ionisation coefficient
α_A	Absorption coefficient
α_T	Tunnelling parameter
β	Hole ionisation coefficient
ΔE	Energy difference between valence band and conduction band
Δf	Bandwidth
ε_0	Permittivity of free space (8.854×10^{-12} m^{-3} kg^{-1} s^4 A^2)
ε_r	Relative permittivity
$\varepsilon_{\lambda 1}$	Emissivity over spectral range of first detector in two-colour detector
$\varepsilon_{\lambda 2}$	Emissivity over spectral range of second detector in two-colour detector
η	Quantum efficiency
θ	Optical field of view
θ_M	PSD measured signal phase
θ_{REF}	PSD reference signal phase
λ	Wavelength
λ_1	Mean effective wavelength of first wavelength band in two-colour detector
λ_2	Mean effective wavelength of second wavelength band in two-colour detector
$\lambda_{cut\text{-}off}$	Cut-off wavelength
λ_m	Mean effective wavelength
λ_p	Peak radiated power wavelength

λ_{peak}	Peak wavelength
ρ	Blackbody aperture radius
σ	Stefan-Boltzmann constant (5.670×10^{-8} J s^{-1} m^{-2} K^{-4})
τ_{eff}	Effective carrier lifetime
$\boldsymbol{\Phi}$	IRAS SNR term
ω_M	PSD measured signal frequency
ω_{REF}	PSD reference signal frequency

Chapter 1 – Introduction

1.1 The measurement of temperature

1.1.1 A brief history of temperature measurements

The measurement of temperature dates back to 170 AD by Claudius Galenus, a Greek physician, who used a mixture of boiling water and ice to create a temperature scale [1]. Galenus' scale incorporated "four degrees of heat" and "four degrees of cold" either side of a neutral point to measure the temperature of diseased gladiators [1][2]. However, it wasn't until Galileo Galilei between 1593 and 1597 that the first thermometer is attributed with being invented [3]. This instrument consisted of a thin glass tube with a hollow sphere on the end. The opposite end of the tube was then placed inside a glass vessel containing coloured water. As the temperature of the air inside the sphere increased the air expanded, hence making the liquid go down within the tube, whilst liquid rose with decrease in temperature. However, the instrument did not feature a temperature scale, meaning that it was actually a thermoscope rather than a thermometer [2].

Various thermometer variations developed from Galileo's first instrument over the following decades, with incorporation of numerical scales. However, these scales lacked standardisation and accuracy, which therefore resulted in thermometers not being reliable. However, this became possible by the determination of fixed points for thermometer calibration. The first modern temperature scale was developed by Daniel Fahrenheit in 1724 [1], and is what is known as the Fahrenheit scale today. Fahrenheit's original scale was based upon three fixed points. A zero point was defined by a water, ice and salt mixture; a middle point defined by a mixture of water and ice only; and a higher point defined by human body temperature. Fahrenheit later made adjustments to his scale, whilst scientists have since made further refinements to define the freezing and boiling points of water to be exactly 32 and 212 ºF, respectively. Although the Fahrenheit scale is still used today, the most commonly used scale is the Celsius scale. Developed by Anders Celsius in 1742, the

scale consisted of 100 degrees with the fixed points defined at the boiling and freezing points of water. These were originally defined on the scale at 0 and 100, respectively [1]. After Celsius died, this scale was reversed and the scale was used with thermometers. The development of such fixed points for thermometer calibration was essential for standardisation of thermometers, with additional fixed points incorporated over the years for the calibration of thermometers we use today [4].

Although the measurement of temperature progressed through the development of thermometers and temperature scales, there was no real understanding of the underlying physics of temperature. For instance, there was no basis in Lord Kelvin's formulation of the second law of thermodynamics. Kelvin, formally William Thomson, first suggested the modern definition of temperature [5]. His formulation of the second law was in terms of heat engine efficiency, which demonstrated the inseparable link between heat and energy. Kelvin is also responsible for determining the correct value for absolute zero, -273.15 ºC, which is the point where heat can no longer be removed from a system as atomic vibrations stop. This later lead to the Kelvin scale, which is used in science today [1], with kelvin being a base unit in the International System of Units. Absolute zero is defined as 0 K, with the scale using the same degree increment as the Celsius scale.

As the science of thermodynamics developed, four laws were defined which govern thermodynamic systems. The first law, which was an adaptation of the conservation of energy law, was adapted for thermodynamic systems. It states that change in a closed system's internal energy is equal to the heat supplied to that system minus the work done on the surroundings by the system. The second law, discussed above, states that an isolated system's entropy will never decrease as the isolated system will always evolve towards thermodynamic equilibrium. The third law states that, as the temperature of a system approaches absolute zero, the entropy of that system approaches a constant value. The fundamental law of thermodynamics, however, is the zeroth law, which was named in this way due to the first three laws already having been defined. It states that two systems, which are in thermal equilibrium

with a third system, must also be in thermal equilibrium with each other. It is by this fundamental law that contact thermometers operate.

Ultimately, the science of thermodynamics culminated with Maxwell-Boltzmann statistics, which describe the average distribution of material particles that are non-interacting over energy states that are in thermal equilibrium. This is the case when the particle density is low enough, or the temperature is high enough, such that quantum effects become negligible. This allowed the derivation of the Maxwell-Boltzmann distribution, which describes the probably of the speed of a particle as a function of a system's temperature.

1.1.2 Practical thermometry

Different techniques for the measurement of temperature have been developed over the years, resulting in several contact measurement thermometer technologies. Such methods measure the change in a physical property with temperature. Examples include glass thermometers, thermocouples, resistance temperature devices (RTDs) and thermistors.

Glass thermometers, involving the expansion of liquids within a glass tube, were used by both Fahrenheit and Celsius when developing their temperature scales. Mercury was the liquid of choice [1]. The measured temperature relates to the point on the temperature scale markings that the mercury has risen to as it expands to with increased temperature. However, the toxic nature of mercury has lead to the reduced use of glass thermometers, particularly for medical applications.

RTDs and thermistors are sensors which involve a change in their electrical resistance with temperature, with the resistance of the sensor relating to measured temperature [6]. The sensitive element of an RTD is a metal, whilst for a thermistor it is a semiconductor material. Thermistors are more sensitive to small changes in temperature, whereas RTDs are sensitive over a wider temperature range [6].

Thermocouples utilise the Seebeck effect, and consist of two junctions of dissimilar metals [6][7]. One of junctions is held at a reference temperature, whilst the other is placed in thermal equilibrium with the first. A temperature gradient exists between the junctions, and therefore a voltage difference is generated related to this gradient. The temperature can therefore be inferred from this gradient. Thermocouples are highly versatile, with different combinations of metals enabling the measurement of different temperatures [7]. Although they offer the measurement capability of high temperatures, they are less accurate than alternative contact thermometry methods at lower temperature.

Although effective for measurement scenarios where contact can be made with the object being measured, there are limitations to contact thermometry methods. Examples include the requirement for a fast measurement time, target objects which are unreachable or scenarios where contact with the target object would result in damage to that object or the thermometer [8]. Therefore, this lead to the requirement of non-contact thermometry based on the detection of emitted thermal radiation. This method is known as radiation thermometry. Radiation thermometers work on the principle of measuring the level of infrared (IR) radiation, or emission, from the target object and converting this to a temperature via several processing steps.

1.2 Infrared radiation

IR radiation can be considered as part of the electromagnetic spectrum, with wavelengths ranging from 0.7 to 30 μm. IR detectors can be used to convert an optical signal to an electrical signal. Equation (1.1) shows the relationship between photon energy, E, wavelength, λ, and frequency, f, where h is Planck's constant and c is the speed of light.

$$E = hf = \frac{hc}{\lambda} \tag{1.1}$$

Different photodiode technologies are used to detect different wavelength ranges, with this wavelength range largely determined by the bandgap of the material used.

Other than radiation thermometry, IR detectors are used for a wide range of applications, such as thermal imaging, night vision, spectroscopy, heat seekers and gas sensing. The choice of the detector used depends upon its application and its operating wavelength. The level of performance required for the detector and, ultimately, its cost also affects this choice. The IR spectrum can be split into five regions, which are shown in Table 1.1 along with typical applications for each wavelength band.

Band (μm)	Name	Typical applications
0.7 – 1	Near Infrared (NIR)	Fibre-optic communications, radiation thermometry > 600 ^{o}C
1 – 3	Short-wave Infrared (SWIR)	Remote sensing, long distance communications, radiation thermometry > 200 ^{o}C
3 – 5	Mid-wave Infrared (MWIR)	Missile and seeker applications,
8 – 12	Long-wave Infrared (LWIR)	Thermal imaging, low temperature radiation thermometry > -50 ^{o}C
12 – 30	Very-long wave Infrared (VLWIR)	Astronomy, earth observation

Table 1.1 – Infrared wavelength regions and typical applications

The atmospheric transmission with respect to wavelength varies across the wavelength range [9], although there are sections where the transmission becomes negligible. This is due to a large level of atmospheric absorption caused by molecules such as H_2O and CO_2. Therefore, such regions are not commonly used for sensing applications, whilst care needs to be taken across the entire spectrum to account for this varied transmission.

1.2.1 Planck's Law

The central law used in radiation thermometry, as well as performing investigations using ideal blackbody objects, is known as Planck's Law.

$$W(\lambda) = \frac{c_1}{\lambda^5}\left[\exp\left(\frac{c_2}{\lambda T}\right) - 1\right]^{-1} \qquad (1.2)$$

W(λ) is the power per unit wavelength per unit area of the emitted radiation from an ideal blackbody source, where *T* is the thermodynamic temperature. $c_1 = 2\pi hc^2$ and $c_2 = hc/k$, and are known as the first second radiation constants, respectively, where *k* is the Boltzmann constant. This law assumes a perfect blackbody, with emissivity = 1 across all wavelengths from the irradiating object. The emissivity of any object is a ratio between the energy radiated from that object and the energy radiated from a perfect blackbody at the same temperature. In reality, blackbody sources with emissivity = 1 do not exist, and this needs to be taken into account in the design of radiation thermometers. Figure 1.1(a) shows the blackbody emission spectrum for a perfect blackbody at different values of blackbody temperature, T_{BB}, with T_{BB} = 200, 400 and 600 °C.

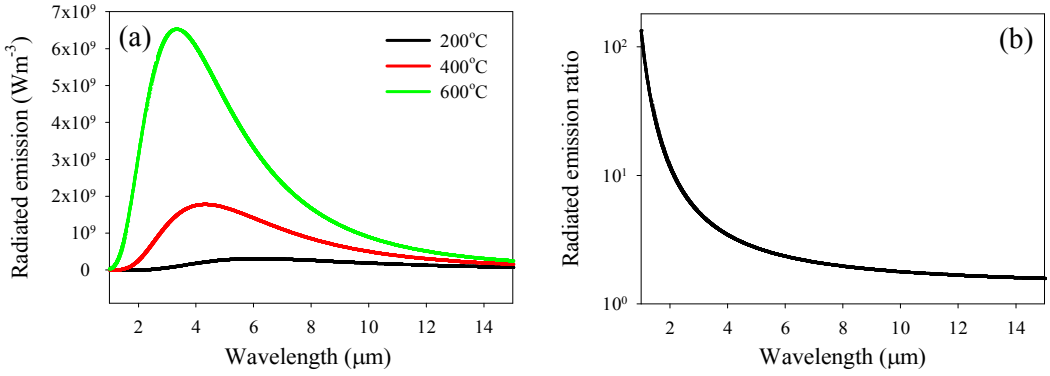

Figure 1.1 – (a) Radiated emission for perfect blackbody at T_{BB} = 200, 400 and 600 °C and (b) ratio of blackbody radiation emission at T_{BB} = 600 °C to that at T_{BB} = 400 °C

As T_{BB} increases, there is an increase in the radiated emission, as well as a blue-shift in the peak and cut-on wavelengths. This cut-on wavelength is defined as point where the radiated emission falls to 50 % of the peak wavelength at shorter

wavelength. The radiated emission changes more rapidly with temperature at shorter wavelengths, making shorter wavelength operation more desirable for radiation thermometry. This leads to reduced error from uncertainty in target object emissivity (as will be discussed in detail in section 2.2.2). This is illustrated in Figure 1.1(b) by comparing the ratio of the radiated emission at each wavelength at T_{BB} = 600 ^{o}C to that at T_{BB} = 400 ^{o}C. Clearly the ratio is smaller at longer wavelengths and hence more susceptible to measurement errors due to uncertainties in the emissivity and influence of the ambient conditions on the measurement.

1.2.2 Wien's Displacement Law

Wien's Displacement Law gives the wavelength at which the emitted radiation is at its maximum. As temperature rises, there is a shift in the peak energy to the shorter wavelengths, as described by equation (1.3), where λ_P is the peak radiated power wavelength.

$$\lambda_P = \frac{2898}{T}\mu m \tag{1.3}$$

Like radiated emission with temperature, this peak wavelength decreases with increasing temperature.

1.2.3 Wien Approximation

The Wien Approximation, equation (1.4), is a simplified version of Planck's Law, and therefore enables easier mathematical manipulation. This simplification can be used if the wavelength is restricted to shorter than λ_P for any given temperature. This leads to the exponential term becoming much greater than 1, allowing the '-1' term to be neglected, as shown in equation (1.4).

$$W(\lambda) = \frac{c_1}{\lambda^5}\exp\left(\frac{-c_2}{\lambda T}\right) \tag{1.4}$$

The Wien Approximation is highly relevant to this work, as it is used to relate the fluctuation in the measured signal to a temperature error, as will be discussed further in section 2.2.2.

1.2.4 Stefan-Boltzmann Law

The total energy emitted by a blackbody at all wavelengths, E_λ, at a given temperature is represented by the Stefan-Boltzmann Law, equation (1.5).

$$E_\lambda = \sigma T^4. \qquad (1.5)$$

Here σ is the Stefan-Boltzmann constant, and the law effectively represents the area below the Planck curve, indicating that the total energy emitted increases rapidly as temperature increases, by the power of 4. Figure 1.2 shows how this total energy varies with T_{BB}.

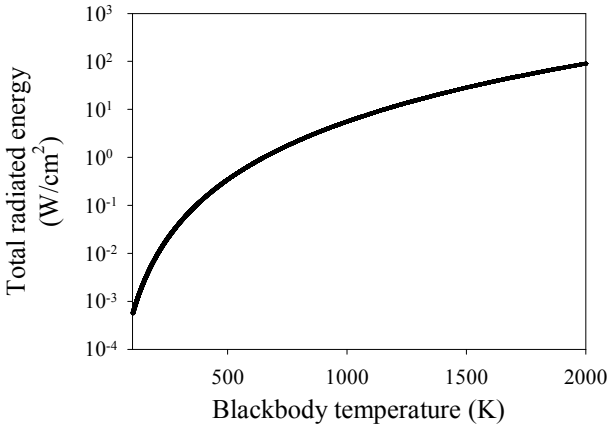

Figure 1.2 – Total radiated energy with T_{BB}

This is relevant as it allows an estimation of the amount of power which falls upon the detector's surface. This influences the choice of detector. For example, if the amount of power falling upon the detector becomes less than 1 nW, such that the signal is smaller than the amplifier noise, a more sensitive detector may be required. This reduction in power may be the case for measurement scenarios where the

thermometer is further away from the target object, such as long range temperature measurements. More sensitive detectors will be more suitable for such scenarios.

1.3 Radiation thermometers

1.3.1 Radiation thermometer system

A practical radiation thermometer system is composed of several elements in order to convert the IR radiation to an associated temperature. Figure 1.3 shows the system diagram for a typical practical radiation thermometer.

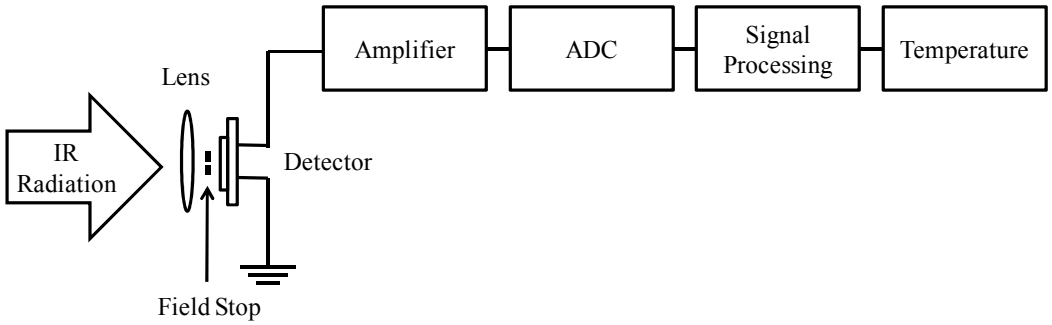

Figure 1.3 – Typical practical radiation thermometer system

The IR radiation from the target object is focused using a lens or mirror system onto the optical window of the detector. A field stop may be used to define the part of the object that is being measured. The detector then converts the IR radiation into a photocurrent which flows into an analogue circuit. This circuit usually contains a transimpedance amplifier (TIA) which amplifies the photocurrent and converts it to a voltage. The voltage can then be read off and converted into a digital signal using an analogue-to-digital converter (ADC), which is subsequently processed. The thermometer's software converts the data into a presentable form which can be displayed by the instrument.

1.3.2 Advantages and challenges of radiation thermometry

Radiation thermometry has several key advantages over contact thermometry. Radiation thermometers make it possible to measure the temperature of remote or

inaccessible targets, which are not possible by contact thermometry. One example is monitoring the surface temperature of semiconductor wafers during growth [10]. Contact methods would lead to contamination or damage to the wafers. In other applications, where the target object is excessively hot, typically above 1000 ^{o}C, contact thermometers may get damaged. Another measurement challenge for contact thermometers is the measurement of fast moving objects such as gas turbine blades [11].

Radiation thermometry can be used across a wide range of target object temperatures. However, the application dictates the choice of technology used, with different applications requiring different design considerations or level of performance. In some measurement scenarios, the application dictates the thermometer wavelength range due to wavelength dependent transmission properties.

Within the glass and plastic manufacturing industry, the measurement of temperature is critical to ensure the final product is of high quality, whilst also ensuring that energy costs are managed. The challenge in glass manufacture is that most glasses are transparent to wavelengths within the visible and NIR regions. If a thermometer in this wavelength range were to be used, the thermometer would measure the temperature of the object behind the glass instead. However, due to glass becoming opaque at wavelengths greater than 4.5 μm, a thermometer operating at this wavelength would make it possible to measure the glass temperature. Similarly, in plastics manufacture, windows at 3.43 μm and 7.9 μm are chosen, with most plastics opaque at these wavelengths [8].

Another application for narrow waveband radiation thermometers is industrial furnaces, where there are high concentrations of H_2O and CO_2 gases. However, a thermometer tuned to 3.9 μm can be used which ‘looks through the flames’; there is no H_2O and CO_2 absorption at this wavelength [8].

For certain measurements scenarios, the field of view (FOV) of the target may become obscured by fixed objects, dust and gases. Additionally, for other measurement scenarios, the emissivity of the target object may be unknown or change during the measurement. Examples are the measurement of the galvannealing process and titanium processing [12][13]. In these situations, use of conventional single wavelength thermometers will lead to inaccuracies in the measurement. Therefore, a ratio radiation thermometer, using two detectors operating over separate spectral ranges, could be used instead. Instead of the absolute photocurrent corresponding to the measured temperature, the temperature is determined by the ratio of photocurrents between each detector. With the wavelength range of each detector being different, the ratio between the photocurrents will vary with temperature. If the target object is obscured or its emissivity is equal at both wavelengths, the photocurrents of each detector reduce. However, the ratio between the photocurrents will stay the same and the temperature can hence be determined. The accuracy of ratio radiation thermometers are less than correctly calibrated single wavelength thermometers (this will be discussed further in section 2.2.3). However, they offer advantages for more challenging measurement scenarios.

1.3.3 Radiation thermometer development

Since the advent of the radiation thermometer, several key developments have taken place to produce the radiation thermometers we have today [14]. Several authors have published detailed descriptions of radiation thermometry theory and measurements, as well as other temperature measurement methods [15][16][17].

The first modern radiation thermometer, developed by Holborn and Kurlbaum, was known as a disappearing filament pyrometer [18]. This thermometer consisted of a thin wire, heated by a current, placed in front the target object. The user views the wire's brightness in comparison with the target object behind it, whilst altering the amount of power to the wire. Once the wire appears to have the same brightness as the target object, the temperature can be read off the instrument via its calibration scale. Due to the nature of the measurement, the instrument is limited to measuring

temperatures where the target object's emission is visible. This corresponds to target temperatures down to 600 ^{o}C.

A major limitation of the disappearing filament pyrometer is that, to ensure accuracy, a skilled user is required to be in control of the instrument. Additional limitations include its inability to be used in dangerous or inaccessible environments, and its unsuitability for continuous or high speed measurements [15]. Therefore, this led to the development of photoelectric pyrometers.

A further limitation of the disappearing filament pyrometer surrounded the uncertain emissivity of the target object. This led to the development of the two-colour technique for temperature measurement [19]. Two-colour radiation thermometers, or ratio radiation thermometers, make use of the greybody assumption that the emissivity of the target object is the same at each wavelength.

The first photoelectric thermometer utilised a photomultiplier tube (PMT) [20]. It was demonstrated above the gold point and resulted in 5 times improvement in measurement accuracy compared with using a disappearing filament pyrometer. In contrast to previous methods, the design also incorporated a field stop and a bandpass filter, which are still used in modern day instruments.

The next major development was the use of a Si photodiode within a radiation thermometer [21]. Its long term reliability led to its use in a broad range of measurement situations, including steel furnaces and turbine temperature measurement. Longer wavelength photon detector technologies were later introduced for radiation thermometry to meet lower temperature measurement requirements. The radiation thermometers which are used today use a wide range of thermal and photon detectors to meet various measurement requirements. The next section gives an overview of the various types of detector technology used.

1.4 Infrared detectors

The detector element within a radiation thermometer is the critical component, and is either a thermal detector or a photon detector. Thermal detectors function by heating up when they absorb a photon. This changes the physical properties of the material and hence results in a change in the electrical output. Thermal detectors are less dependent upon photon wavelength, and therefore will detect across a wider IR spectrum. They are mainly used for low cost room temperature applications where a low level of performance is sufficient; they are generally slow.

Photon detectors work by the absorption of photons which generate electron-hole pairs leading to a change in the electrical output signal. Their wavelength of detection is dependent upon the bandgap of the semiconductor material used, with a narrower bandgap corresponding to a longer detection wavelength. Short wavelength detectors, with wider bandgaps, do not need cooling to operate, just temperature stabilising. However, dark currents, leading to noise, created by thermally generated charge carriers are a problem with narrow bandgap photon detectors. Cooling is therefore required to reduce the dark current and ultimately the noise. Conventionally, cooling to temperatures of 200, 77 and 4.2 K is achieved with use of thermo-electric, nitrogen and helium cooling, respectively. This requirement for cooling makes narrow bandgap photon detectors potentially heavy, bulky and costly. However, they offer a higher level of performance than thermal detectors.

1.4.1 Current generation of infrared detectors used in radiation thermometry

The current generation of commercial radiation thermometers use both thermal and photon detectors. In the NIR to SWIR regions, detector technologies within radiation thermometers are dominated by uncooled photon detectors; Si [22], InGaAs [23] and Ge [24]. They are cheap, readily available, and offer direct detection (DD) operation (no optical modulation is required).

Si photodiodes operate in the 0.4-1.1 μm wavelength range. The cost of Si is very low, which has driven the use of Si in the electronics industry and as a detector in

radiation thermometry [25]. The short wavelength response of Si is ideal for the accurate measurement of high temperature target objects. However, this short wavelength response limits Si to the measurement of target object temperatures down to ~400 ^{o}C.

Conventional InGaAs photodiodes, composed of InP cladding layers and an InGaAs absorber, operate at longer wavelengths than Si, 0.9-1.7 μm. They are commonly used within radiation thermometer systems to measure lower temperature target objects than Si [26]. InGaAs is also commonly used in telecommunications; the low attenuation windows within optical fibres are within the spectral range of InGaAs. Extended wavelength InGaAs can also be grown, up to a cut-off wavelength of 2.6 μm, and allow for the measurement of lower target object temperatures. For example, conventional InGaAs may detect down to 150 ^{o}C [26], but extended InGaAs can measure as low as 50 ^{o}C [27], with use of an optical chopper.

Ge photodiodes operate over a similar spectral range to InGaAs. However, Ge photodiodes are indirect bandgap. Although this leads to very pure growth and potentially low dark current, it also leads to reduced quantum efficiency at longer wavelengths compared to the direct bandgap InGaAs. Therefore, InGaAs photodiodes may be preferred. Ge photodiodes have been used in radiation thermometers [28].

As the wavelength extends to the MWIR, other technologies are used. These include PbSe [29] and cooled HgCdTe (MCT) [30]. As the wavelength extends further into the LWIR, uncooled thermal detectors are used, such as bolometers [31], pyroelectric [32] and thermopiles [33].

PbSe is currently used in radiation thermometry [34]. PbSe photodetectors work using the photoconductive effect, with the detector resistance changing with incident IR photons. They are highly temperature sensitive, with change in the ambient temperature affecting their response and dark resistance. They are also strongly frequency dependent, which leads to changes in performance if the measurement system modulation is not optimised. For example, care needs to be taken within the

conditioning circuit to account for variation in the noise or thermal drift. In addition, use of an optical chopper at higher frequencies leads to mechanical variation in the frequency, which therefore leads to change in the performance of the highly frequency sensitive PbSe [35]. These detectors work at room temperature in the MWIR range, with a typical D* of 1×10^{9} $cmHz^{1/2}/W$ [36]. PbSe suffers from poor stability over time and high 1/f noise. It is grown using chemical bath deposition, with growth issues leading to non-uniform growth. This prevents the use of PbSe for large area arrays. However, linear arrays are available commercially, with alternative growth methods of PbSe being explored [37].

Cooled MCT is the leading photon detector technology at longer wavelengths, and is the leading technology used in focal plane arrays (FPAs). For MWIR and LWIR, its D* is around 1×10^{11} and 3×10^{10} $cmHz^{1/2}/W$, respectively [38]. It is also used in radiation thermometry [39]. As a photoconductor, it functions by its resistance dropping when IR radiation is incident upon it. MCT can be wavelength tuned from the SWIR to VLWIR regions, by altering the composition of the HgTe and CdTe materials, and exhibits high D* and high quantum efficiency with normal incidence operation. The main problem associated with MCT is the challenges arising during growth and processing. MCT suffers from high production cost and low yield; a limitation for growth of very large area arrays. Additionally, the high dark current of MCT requires the detector to be cooled cryogenically or thermo-electrically in order to operate.

Bolometers, pyroelectric and thermopiles have been used in radiation thermometry [40][41]. Bolometers function by incident photons raising the material temperature, leading to a change in its electrical resistance. It forms part of a potential divider circuit, with the output voltage read off by a readout circuit. A bolometer's typical specific detectivity (D*) is around 2×10^{8} $cmHz^{1/2}/W$ [38]. For pyroelectric detectors, a temperature change results in a change to the detector's spontaneous polarisation which causes a charge to flow; its D* can be related to this charge. Typical pyroelectric D* values are around 1×10^{9} $cmHz^{1/2}/W$ [38]. Thermopiles consist of several thermocouples connected together, with a voltage generated based on the

temperature change of a junction consisting of two dissimilar materials. The typical D* of a thermopile is 1×10^{8} cmHz$^{1/2}$/W [38].

As mentioned in section 1.3.2, a ratio radiation thermometer can be used to overcome the influence of the emissivity of a target object. Ratio radiation thermometers require the use of two-colour detectors to provide two separate spectral bands [42]. At present, economically viable two-colour detectors are limited to the NIR and SWIR regions, with Si-Si and Si-InGaAs [43] detectors commercially available. The basic principle of two-colour detectors involves two detectors stacked on top of each other. Shorter wavelength photons are absorbed by the top detector, whilst longer wavelength photons pass through and are absorbed by the bottom detector. At longer wavelengths, use of broadband detectors with filters can be used in ratio radiation thermometers. However, this approach is expensive and therefore undesirable.

1.4.2 Alternative potential detector technologies

In order to move towards the next generation of radiation thermometers, new detector technologies need to be explored. However, these detectors need to offer capabilities not offered by the current generation, with each technology offering its own specific capabilities. These benefits include increased sensitivity, the potential for array implementation, uncooled longer wavelength response and flexible longer wavelength multi-colour detection.

When photoelectric pyrometers were first introduced, the PMT was the first technology demonstrated for radiation thermometry [20]. PMTs are highly sensitive devices which can detect down to a single photon, therefore allowing them to be used in photon counting applications [44]. They have been demonstrated in radiation thermometry [45], although the main focus was the development of photoelectric pyrometers rather than for photon counting thermometry.

Avalanche photodiodes (APDs) are also highly sensitive; they make use of a high internal gain mechanism through the impact ionisation process [46]. A detailed description of APD operation is given in section 2.3.1. The high gain allows the

APD to overcome electronic noise, making them attractive for low light level applications, either due to weak emitted signal or long range measurements. When properly designed, APDs can achieve single photon sensitivity. Si and InGaAs/InP APDs are commercially available, although they are more expensive than their p-n or p-i-n counterparts. The increased sensitivity of APDs makes them highly attractive for use in radiation thermometry. They offer the potential detection of lower temperature target objects and longer range temperature measurements.

MWIR InAs/GaSb type-II superlattices (T2SLs) are a promising technology for longer wavelength detection beyond 3 μm [47]. The band structure of T2SL is shown in Figure 1.4, where E_C and E_V are the conduction band and valance band, respectively.

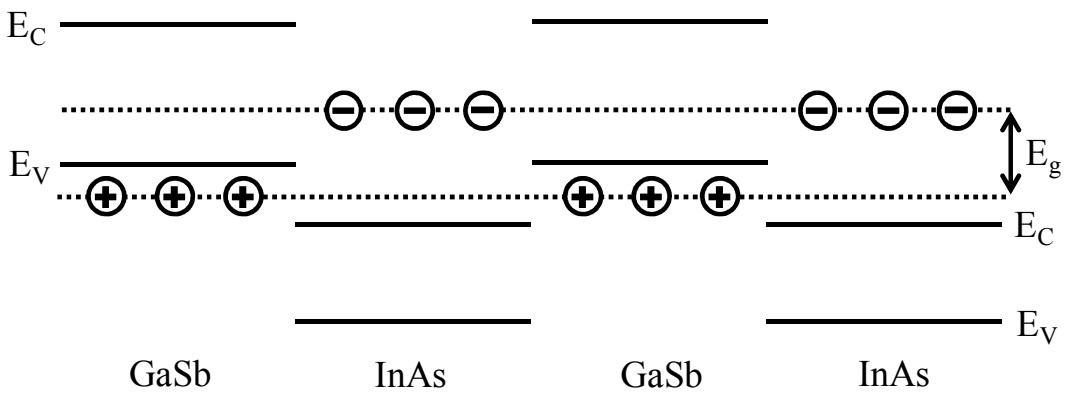

Figure 1.4 – InAs/GaSb T2SL band diagram

More details are given in section 2.3.2, but their basic operation is as follows. InAs/GaAs T2SLs feature alternative layers of InAs and GaSb, with the effective bandgap of the superlattice, E_g, determining the detection wavelength. This is tunable by varying the strained layer superlattice (SLS) period in terms of monolayers (MLs) of the InAs and GaSb materials (1 ML is a single layer of closely packed atoms). Therefore, the detection wavelength can be tuned to adjust the peak wavelength for specific applications. This is attractive for radiation thermometry, as it allows this peak wavelength to be tuned to match an application's specific wavelength window, with tunability between 3 – 30 μm. Combining this bandgap tunability with the ability of growing T2SL layers on top of each other leads to the

potential for multi-colour detection across several wavelength bands [48][49]. This is a capability currently only offered by MCT for MWIR.

An additional potential benefit of T2SL arises due to the spatial separation of the electron and hole within the structure. This leads to the T2SL having low Auger recombination, leading to potential low dark current, high operating temperature and high D*. However, in practice, current T2SL detectors still suffer from high dark currents, predominantly originating from surface leakage mechanisms [50]. In the MWIR wavelengths, D* values of above 1×10^{12} cmHz$^{1/2}$/W at 77 K are typical [51][52], whilst D* of greater than 1×10^{9} cmHz$^{1/2}$/W has been demonstrated at room temperature [53][54]. T2SLs have also been developed into arrays [55][56]. Combining all the advantages of T2SL, there is the potential to grow uncooled MWIR single- and multi-colour arrays for radiation thermometry.

Quantum well infrared photodiodes (QWIPs) consist of narrow bandgap material surrounded by larger bandgap material, as shown in Figure 1.5, which forms a quantum well (QW).

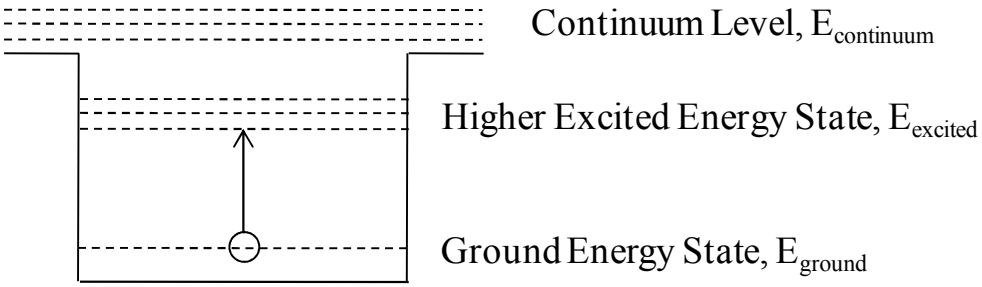

Figure 1.5 – QWIP band diagram

The structures consist of quantised energy states within the QW. When a photon is absorbed by the material, an electron is excited from the ground state to the higher excited energy states or to the continuum level. Electrons from higher energy states escape to the continuum states via tunnelling or thermionic processes. Photocurrent is formed when these electrons are swept by an electric field. Compared to MCT, QWIPs benefit from relatively mature growth and processing techniques, which

leads to high uniformity and large area arrays. However, they require a diffraction grating in order to absorb photons at normal incidence, due to their 1-dimensional (1D) carrier confinement. This 1D carrier confinement also leads to lower quantum efficiency, larger dark currents and prevents higher temperature operation. Currently QWIPs are used in LWIR thermal imaging cameras. *Gunapala et al.* [57] report a LWIR QWIP camera with a noise equivalent differential temperature (NEDT) of 36 mK and D* of 2×10^{11} cmHz$^{1/2}$/W at 70 K.

Similar in structure to QWIPs, the **quantum dot infrared photodetector (QDIP)** contains a quantum dot (QD) within a QW in order to provide 3-dimensional (3D) carrier confinement [47], as shown in Figure 1.6. This leads to low dark current, with the added advantage of normal incidence operation and long excited state lifetime. However, they suffer from non-uniformity in the distribution of the dot sizes and have a smaller quantum efficiency.

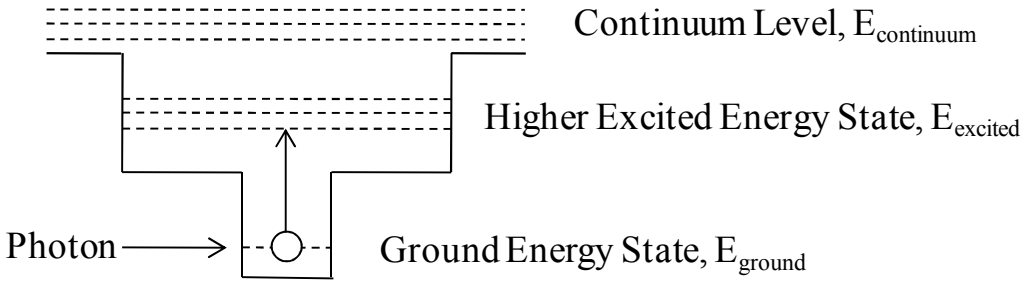

Figure 1.6 – QDIP band diagram

Like QWIPs, when photons are absorbed by the material, an electron is released, this time from the QD ground states. The electron will undergo a transition into either the higher excited states in the QW, or into the continuum level, depending on the energy of the photon. A unique feature of QDIPs is that they are bias tunable to different wavelengths, and therefore they are seen as a viable technology for multi-spectral sensing [58][59]. Although QDIPs are not used in radiation thermometry, their potential in ratio radiation thermometry has been demonstrated [60]. QDIPs have also been developed into arrays [61], leading to potential growth of multi-colour arrays for radiation thermometry. The photoconductive gain of QDIPs also

leads to increased sensitivity, leading to QDIPs having higher responsivity. More QDIP theory is provided in section 2.3.3.

1.5 Literature review of infrared detector technologies investigated in this thesis

1.5.1 Avalanche photodiodes

APDs are attractive for use in radiation thermometry due to increased sensitivity provided by their high internal gain. However, another major attraction for their use in radiation thermometry is their current commercial availability. They are therefore suitable for immediate integration into radiation thermometers.

The most suitable APDs for immediate use in radiation thermometry are Si and InGaAs/InP APDs, which are commercially available from suppliers like Hamamatsu [62][63]. Additionally, Hamamatsu also offers APD arrays [64]. Other materials have been investigated for use as APDs, but will not be considered further here.

Historically the development of APDs was driven by optical communication requirements; their high internal gain provides the capability for high speed operation. Si APDs have been demonstrated for use as optical receivers [65]. Si is a very good material for APDs because, in Si, electrons ionise much more readily than holes, leading to minimal fluctuation in the ionisation statistics and hence very low excess avalanche noise. Si offers the lowest avalanche excess noise for detection of visible wavelengths. Si APDs are a mature technology, but like all mature technologies, significant work was undertaken to get them to the stage they are at today [66]. However, due to the move of optical communication to the 1.3-1.55 μm window, APD development has focused on III-V materials. InGaAs/InP based APDs, the preferred choice, have achieved 5-10 dB better sensitivity than p-i-n photodiodes [67]. InGaAs and materials used for avalanche region (InP and InAlAs) have comparable ionisation rates of the electrons and holes, leading to poorer noise and frequency performance compared with Si [68].

In addition to their high internal gain, the high sensitivity of APDs also offers the detection of low light level signals. Si single photon avalanche diodes (SPADs) have been demonstrated [69] by operating an APD in the so-called Geiger mode above the breakdown voltage. In this mode, the very high electric field of SPADs provides a very high avalanche multiplication. Absorption of a single photon can result in a signal which can be amplified to a level that is easily detected by conventional electronics. An example of an important application for SPADs is quantum key distribution [70]. The high sensitivity of APDs also leads to its use for long range optical detection, making APDs ideal for free-space optical communication [71][72]. This suggests that APDs would also be ideal for long distance temperature measurements.

Other potential applications of APDs include laser range finding [73] and high energy particle detection [74]. To the best of the author's knowledge, APDs had not previously been demonstrated for use in radiation thermometry until the work described in Chapter 4 was performed [75].

1.5.2 MWIR InAs/GaSb T2SLs

Research into MWIR InAs/GaSb T2SLs has been carried out by several groups. The main groups carrying out this research include the University of New Mexico, Northwestern University and the Fraunhofer Institute of Applied Physics. Such investigations are aimed at achieving high D* across the operating temperature range as well as driving up the operating temperature to achieve uncooled operation. A major aim of T2SL research is to develop uncooled large area T2SL FPAs for imaging applications [55][56], hence making MWIR imaging more affordable. The wavelength tunability of T2SLs, and the ability to grow one detector on top of another, also leads to the potential growth of multi-colour detectors [48][49]. Putting all these benefits together leads to the potential of uncooled, affordable, single- and multi-colour arrays for temperature measurement in the MWIR region. A review of some of the T2SL research which makes the technology attractive for radiation thermometry follows below, although more extensive reviews have been published [47][76].

T2SLs are traditionally grown upon GaSb substrates due to lattice matching. T2SLs grown on GaSb with high D* has been measured by several authors with the use of cooling. *Kim et al.* [50] report a 77 K MWIR photodiode with D* of 3.5×10^{12} $cmHz^{1/2}/W$ for single-pixel devices, with the same D* achieved for a FPA. Passivation of the etched surfaces resulted in 4 orders of magnitude reduction in dark current density for a single-pixel device at 77 K, with 3 orders of magnitude reduction achieved for the FPA. *Pour et al.* [55] achieved a D* of 1.05×10^{12} $cmHz^{1/2}/W$ at 150 K whilst measuring high bias-independent quantum efficiency. Their detector utilised a tunnelling barrier, which resulted in a decrease in the dark current. *Plis et al.* [51] presented a zero-bias D* of 2×10^{12} $cmHz^{1/2}/W$ at 82 K for a detector with p-on-n polarity. *Walther et al.* [52] reported diodes for FPA applications with a D* in excess of 1×10^{13} $cmHz^{1/2}/W$ at 77 K. Their FPA produced NEDT values below 12 mK, which are comparable with MCT detectors. *Chen et al.* [77] also presented single pixel diodes and a FPA, with a D* of 3×10^{12} $cmHz^{1/2}/W$ at 77 K. However, their NEDT of 33.4 mK is slightly larger.

In order to realise low cost and reduced size detectors, room temperature operation of T2SLs is highly desirable, and has been investigated for T2SLs on GaSb substrates. *Plis et al.* [78] presented a detector grown on a GaSb (111)B substrate with a 295 K D* of 8.5×10^{9} $cmHz^{1/2}/W$, which is significantly better than state-of-the-art T2SL detectors grown on conventional GaSb (100) substrates. A ~1.2 μm red shift in the cut-off wavelength was found compared with a similar detector grown on GaSb (100). This was due to the increase in the heavy hole effective mass in the (111) direction in comparison with the (100) direction. *Wei et al.* [54] demonstrated a D* of approximately 1×10^{9} $cmHz^{1/2}/W$ at 296 K with a 5 μm cut-off on a conventional (100) substrate. *Rodriguez et al.* [79], in early reported work, demonstrated 293 K operation of a TS2L with a responsivity of 0.7 mA/W at 3.5 μm, along with a cut-off wavelength of 5.9 μm.

In order for the cost of T2SLs to be reduced further, work has been carried out to achieve successful growth of T2SL detectors on cheaper GaAs substrates. This is essential in order to develop T2SLs for arrays. *Nguyen et al.* [80] achieved a D* of 6×10^{11} $cmHz^{1/2}/W$ at 77 K for a MWIR T2SL photodiode, with a quantum efficiency

of 36.4 %. At room temperature, the D* was lower, with 6×10^{8} cmHz$^{1/2}$/W achieved. They studied how D* and quantum efficiency varied with temperature, as well as investigating the temperature dependence of the dark current mechanisms. *Plis et al.* [53] evaluated an nBn T2SL detector grown on a GaAs substrate. Results were promising, with D* of around 1×10^{11} cmHz$^{1/2}$/W calculated at 77 K, and a room temperature D* of around 1×10^{9} cmHz$^{1/2}$/W. The nBn structure concept allows majority carriers to be blocked with the aim of removing surface currents. *Huang et al.* [56] presented what they believed to be the first photovoltaic T2SL FPA grown on GaAs. They found that the most appropriate operating temperature for it to be 67 K.

Another key challenge for T2SLs is the reduction of the high surface leakage currents. Surface passivation is a method of reducing this leakage current, with techniques such as SU-8 [81], polyimide [82] and SiO_2 [83] having been demonstrated. In addition to this, optimised wet and dry etching techniques are required [84].

The main qualities which motivate the use of T2SL for radiation thermometry are high D*, high temperature operation, array implementation and multi-colour detection, whilst growth on GaAs substrates offers development of cheaper detectors. Table 1.2 provides a summary of the best results which satisfy these motivations. These results suggest the performance of T2SL is approaching that of MCT when cooled to 77 K, while room temperature performance is moderate compared to the best uncooled MWIR PbSe photodetector.

Motivation	Author	Summary
High D* (at 77 K)	*Walther et al.* [52]	D* > 1×10^{13} cmHz$^{1/2}$/W
High operating temperature	*Plis et al.* [78]	D* = 8.5×10^{9} cmHz$^{1/2}$/W at 290 K
Array implementation	*Huang et al.* [56]	T2SL FPA on GaAs
Multi-colour detection	*Rehm et al.* [48]	Development of multi-colour T2SL FPA
Growth on GaAs substrate	*Nguyen et al* [80]	D* = 6×10^{11} cmHz$^{1/2}$/W at 77 K and 6×10^{8} cmHz$^{1/2}$/W at 290 K

Table 1.2 – Summary of best results for desirable T2SL qualities for use in radiation thermometry

1.5.3 QDIPs

Research into QDIP technology has been carried out by a wide range of groups with the aim of achieving high performance and high operating temperature photodetectors for multi-spectral imaging. High D* QDIPs have been demonstrated with cryogenic cooling, although higher operating temperature QDIPs have also been demonstrated. This leads to the potential for thermo-electrically cooled operation. Additionally, a QDIP has previously been suggested as a suitable detector for temperature measurements [60]. QDIPs have been demonstrated as arrays [61], leading to the potential for the technology to be developed for multi-colour arrays for temperature measurements. Other desirable features of QDIPs for use in radiation thermometry include their tunability for use in multi-spectral detection and the development of narrow spectral responses. Full reviews into QDIP research have been carried out [47][85][86][87], with some key results which make them attractive for radiation thermometry reviewed below.

High D* has been achieved in several cases for QDIPs. *Kim et al.* [88] evaluated a QDIP with a D* of 3×10^{11} cmHz$^{1/2}$/W, with a measured noise of below 10^{-14} A/Hz$^{1/2}$ and peaks at 9.3μm and 8.7 μm. A QDIP grown by *Tsao et al.* [89] was reported

with a high D* of 2.3×10^{11} cmHz$^{1/2}$/W at 120 K. This was achieved by the use of InAs QDs grown on $Al_{0.48}In_{0.52}As$ barriers capped by $Ga_{0.47}In_{0.53}As$ quantum wells. *Barve et al.* [90] improved on these results by increasing the D* at 77 K to 4×10^{11} cmHz$^{1/2}$/W using AlGaAs current blocking barriers.

The drive towards operating QDIPs closer to room temperature is essential for realising lower operating costs. The structure investigated by *Barve et al.* [90] also achieved a high operating temperature, resulting in the highest reported D* for a wavelength longer than 7 μm at 200 K of 7.4×10^{8} cmHz$^{1/2}$/W. *Bhattachaya et al.* [91] reported QDIPs operating between 240 and 300 K, with a peak value of D* found at 280 K of 1.5×10^{7} cmHz$^{1/2}$/W. Their method made use of a tunnelling QDIP (T-QDIP), which involves the dark current and photocurrent being decoupled using a double-barrier resonant tunnelling heterostructure. *Chakrabarti et al.* [92] reported a QDIP with a high D* of 6×10^{9} cmHz$^{1/2}$/W at 200 K. It featured 70 layers of doped InAs QDs, with an $Al_{0.3}Ga_{0.7}As$ barrier. *Tang et al.* [93] presented a QDIP operating at 250 K with a D* value of 2.45×10^{8} cmHz$^{1/2}$/W, with detection in the 2.5-7 μm range. This QDIP made use of large $Al_{0.3}Ga_{0.7}As$ barriers either side of the QDs to reduce the dark current. *Lim et al.* [94] evaluated a QDIP demonstrating a room temperature D* of 6.7×10^{7} cmHz$^{1/2}$/W, with peaks at 3.2 and 4.1 μm. It featured QDs grown inside $Ga_{0.47}In_{0.53}As$ wells, surrounded by $Al_{0.48}In_{0.52}As$ barriers.

QDIPs are highly attractive due to their tunable spectral response. However, greater control over the QDIP spectral response, as well as their bias tunability, can be achieved through use of dot-in-a-well (DWELL) structures. This is due to the ability to grow the QWs with a greater level of accuracy, allowing control over the energy level [95]. *Raghavan et al.* [96] reported the first DWELL structure, resulting in a D* of 2.7×10^{9} cmHz$^{1/2}$/W at 78 K, whilst several other QDIPs have been investigated with DWELL structures [90][97][98]. QDIPs have also been developed into FPAs using the DWELL structure [61][99].

QDIPs have been successfully demonstrated with an infrared algorithmic spectrometer (IRAS) for use as a multi-spectral imager, offering versatile choice of wavelength bands. It was proposed as an alternative to imagers which use costly

optical filters or scanning optics, therefore leading to more cost effective and compact systems. This approach was first proposed by *Sakoglu et al.* [58][59]. The IRAS involves a computation of bias dependent weighting factors, each assigned to bias dependent QDIP spectra, in order to approximate arbitrary filter shapes defined by the IRAS to reproduce spectral shapes. They demonstrated a highly tunable QDIP which offered a wide wavelength range configurable response. The work was used to successfully reproduce the power spectrum of a blackbody signal through a filter made of polyethylene. *Vines et al.* [100] and *Tan et al.* [101] took this further by demonstrating a similar system with a polyethylene sheet and an 800 ^{o}C blackbody source. *Jang et al.* [102] also demonstrated the IRAS for reproduction of LWIR bandpass filters, as well as looking into the choice of bias voltages used within the IRAS. This versatile approach is attractive to ratio radiation thermometry, with the potential development of a versatile ratio radiation thermometer; the filter positions can be optimised to cope with non-greyness in the target object. Ideally, the IRAS should be combined with a QDIP which has the narrowest possible spectral response to allow reproduction of narrower filters. The full-width half maximum (FWHM) of the QDIP spectra investigated by *Tan et al.* [101] was 0.4 μm for one transition, and 0.7 μm for another, making it suitable for reproducing filters down to such sizes. Other QDIPs with FWHM less than 1 μm include *Tsao et al.* [89] and *Lim et al.* [94], with FWHMs of 0.4 and 0.3 μm, respectively.

A summary of the most significant results for the desirable QDIP features follows in Table 1.3.

Motivation	Author	Summary
High D* (at 77 K)	*Barve et al.* [90]	D* = 4×10^{11} cmHz$^{1/2}$/W
High operating temperature	*Chakrabarti et al.* [92]	D* = 6×10^{9} cmHz$^{1/2}$/W at 200 K
Tunability, DWELL	*Krishna et al.* [95]	QDIPs with a DWELL structure
IRAS	*Sakoglu et al.* [58][59]	Initial development of IRAS
Narrowest FWHM	*Lim et al.* [94]	FWHM = 0.3 μm
Array implementation	*Krishna et al.* [61]	320×256 two-colour FPA

Table 1.3 – Summary of best results for desirable QDIP qualities for use in radiation thermometry

1.6 Motivation

The primary motivation behind this work is to introduce the potential next generation of infrared detectors for radiation thermometry. In order to offer improvement over currently available technologies, they need to demonstrate capabilities which the current generation do not. Such improvements include increased sensitivity, uncooled longer wavelength detection, flexible longer wavelength multi-colour detection and the potential for array implementation. This work is motivated by the following requirements:

I. **Increased sensitivity.** This provides the potential of measuring lower target object temperatures without the need of using longer wavelength detectors, particularly since shorter wavelength radiation thermometers offer reduced error from uncertainty in target object emissivity. More sensitive detectors also provide the opportunity for potential long distance temperature measurement. From the literature review presented, it is clear that a Si APD is affordable and provides excellent improvement to a number of low photon sensing solutions. It is therefore surprising that its performance in radiation thermometry has not been reported in the literature. Utilising their high

internal gain, Si APDs can provide additional amplification within radiation thermometers to allow the measurement of lower target object temperatures whilst still utilising shorter wavelength operation. **The performance of a commercial Si APD is evaluated and compared to a Si photodiode.**

II. **Minimally cooled MWIR arrays for radiation thermometry.** Alternative MWIR detectors are desirable due to the current limitations of commercially available detector technologies. Over the last few years the T2SL is the most intensively researched MWIR detector technology. Its fast improving performance and high temperature performance suggest its potential for MWIR thermometers, particularly when affordable arrays are needed. **Characterisation of MWIR T2SLs for radiation thermometry was therefore performed.**

III. **Multi-colour ratio radiation thermometers.** These currently utilise broadband detectors with filters and hence are expensive. Successful growth of affordable uncooled, or minimally cooled, MWIR multi-colour photon detectors will allow more cost effective ratio radiation thermometers to be developed. If optimised, they would make it easier to target "grey" areas in the emitted spectrum of surfaces. T2SL offers some degree of wavelength tunability via superlattice period thickness. The intersubband transitions in QDIPs on the other hand have been demonstrated to show much stronger wavelength tunability. Moreover, QDIPs combined with an IRAS offer an alternative approach to radiation thermometry, offering a versatile choice of wavelengths bands. **It could allow development of a versatile ratio thermometer with tunable wavelength responses. This QDIP-IRAS combination therefore allows optimised measurement of specific target objects.**

1.7 Thesis Overview

Chapter 2 discusses the background theory of radiation thermometry systems and considerations which are required in practical situations. It also discusses how the various detector technologies investigated in this work operate, as well as discussing

the various figures of merit for the detectors. It concludes by discussing the theory and operation of the IRAS demonstrated in Chapter 7.

Chapter 3 discusses the evaluation techniques used in this work. It discusses the methods used to electrically and optically characterise the detectors investigated in this work and photodetectors in general. It also outlines how room temperature and temperature dependent radiation thermometry measurements were performed in this work.

Chapter 4 demonstrates the use of a phase sensitive detection (PSD) method as an alternative to DD, and the benefits it provides. However, its main focus is the demonstration of a Si APD as an alternative to a Si photodiode, demonstrating and discussing the benefits of its increased sensitivity. PSD and DD are compared and contrasted using both detector technologies

Chapter 5 introduces the MWIR InAs/GaSb T2SL as a viable option as an uncooled MWIR detector for radiation thermometry. Three detectors are electrically characterised at room temperature, with the detector with the lowest absorption region doping fully characterised and demonstrated for use within a radiation thermometer system. Its temperature dependence is analysed, with discussion into the potential challenges faced by T2SL technology.

Chapter 6 presents the characterisation of an InAs/GaSb T2SL detector grown upon a GaAs substrate, as well as its use within a radiation thermometry system. The detector is compared against the T2SLs on GaSb substrates, with analysis and discussion on their differences and similarities.

Chapter 7 demonstrates a QDIP for use as a ratio radiation thermometer with use of an IRAS. A QDIP is characterised with its temperature dependence investigated. The QDIP-IRAS combination is then demonstrated for reproduction of arbitrary spectral shapes and computed ratios. Further analysis takes place by varying the IRAS filter properties.

Chapter 8 discusses the overall findings of this work and draws conclusions. Potential future work is then suggested.

References

[1] W. Dreyer, W. H. Müller, and W. Weiss, "Tales of thermodynamics and obscure applications of the second law," *Continuum Mechanics and Thermodynamics,* vol. 12, pp. 151-184, 2000.

[2] V. R. d. Nascimento, "Evaluation of thermometers for ear temperature measurement at the wards in a university hospital," Dissertation, Universidade Nova de Lisboa, Lisbon, Portugal, 2012.

[3] A. Milton, "Thermoregulatory actions of eicosanoids in the central nervous system with particular regard to the pathogenesis of fever," *Annals of the New York Academy of Sciences,* vol. 559, pp. 392-410, 1989.

[4] H. Preston-Thomas, "The International Temperature Scale of 1990(ITS-90)," *Metrologia,* vol. 27, pp. 3-10, 1990.

[5] J. Fischer, S. Gerasimov, K. Hill, G. Machin, M. Moldover, L. Pitre*, et al.*, "Preparative steps towards the new definition of the kelvin in terms of the Boltzmann constant," *International journal of thermophysics,* vol. 28, pp. 1753-1765, 2007.

[6] A. Tong, "Improving the accuracy of temperature measurements," *Sensor Review,* vol. 21, pp. 193-198, 2001.

[7] G. Machin, "Innovations in high temperature measurement," *Measurement and Control,* vol. 45, pp. 141-144, 2012.

[8] J. Dixon, "Radiation thermometry," *Journal of Physics E: Scientific Instruments,* vol. 21, pp. 425-436, 1988.

[9] University of California at Berkeley, http://www.cnr.berkeley.edu/~gong/textbook/chapter2/html/sect24.htm.

[10] G. Feng, K. Oe, and M. Yoshimoto, "Temperature dependence of Bi behavior in MBE growth of InGaAs/InP," *Journal of Crystal Growth,* vol. 301, pp. 121-124, 2007.

[11] M. De Lucia and G. Masotti, "A scanning radiation thermometry technique for determining temperature distribution in gas turbines," *Journal of Engineering for Gas Turbines and Power,* vol. 117, pp. 341-346, 1995.

[12] G. R. Peacock, "Ratio Radiation Thermometers in Hot Rolling and Galvannealing of Steel Strip," in *AIP Conference Proceedings*, 2003, pp. 789-794.

[13] R. Harding and M. Wickins, "Temperature measurements during induction skull melting of titanium aluminide," *Materials Science and Technology,* vol. 19, pp. 1235-1246, 2003.

[14] G. Ruffino, "Modern radiation thermometers: calibration and traceability to national standards," in *International Conference on High Temperatures and Energy Related Materials, IUPAC, Rome*, 1988.

[15] T. J. Quinn, *Temperature*, 2nd ed. London, UK: Academic Press Limited, 1990.

[16] P. Saunders, *Radiation Thermometry: Fundamentals and Applications in the Petrochemical Industry* vol. 78: SPIE press, 2007.

[17] J. Nicholas, D. R. White, and J. Wiley, *Traceable temperatures: an introduction to temperature measurement and calibration*: Wiley New York, 2001.

[18] W. Forsythe, "The disappearing filament type of optical pyrometer," *Transactions of the Faraday Society,* vol. 15, pp. 21-50, 1920.

[19] H. Hottel and F. Broughton, "Determination of true temperature and total radiation from luminous gas flames," *Industrial & Engineering Chemistry Analytical Edition,* vol. 4, pp. 166-175, 1932.

[20] R. Lee, "The NBS photoelectric pyrometer and its use in realizing the International Practical Temperature Scale above 1063 C," *Metrologia,* vol. 2, pp.150-161, 1966.

[21] G. Ruffino, "Comparison of Photomultiplier and Si Photodiode as Detectors in Radiation Pyrometry," *Applied optics,* vol. 10, pp. 1241-1245, 1971.

[22] Hamamatsu Photonics, *Si Photodiodes - S2386 series*. Available: http://www.hamamatsu.com/resources/pdf/ssd/s2386_series_kspd1035e06.pdf, (2013).

[23] Hamamatsu Photonics, *InGaAs PIN photodiodes – G12180 series*. Available: http://www.hamamatsu.com/resources/pdf/ssd/g12181_series_kird1121e01.pdf, (2013).

[24] Judson Technologies, "Germanium Detectors and Position Sensors," 2004.

[25] T. M. Goodman and P. J. Key, "The NPL radiometric realization of the candela," *Metrologia,* vol. 25, pp. 29-40, 1988.

[26] H. Yoon, C. Gibson, V. Khromchenko, and G. Eppeldauer, "SSE-and noise-optimized InGaAs radiation thermometer," *International Journal of Thermophysics,* vol. 28, pp. 2076-2086, 2007.

[27] H. W. Yoon and G. P. Eppeldauer, "Measurement of thermal radiation using Regular glass optics and short-wave infrared detectors," *Optics Express,* vol. 16, pp. 937-949, 2008.

[28] Y. Yasuji, A. Yoriko, and S. Fumihiro, "Development of a calibration standard of the spectral radiance for optical sensors," in *SICE 2002. Proceedings of the 41st SICE Annual Conference*, 2002, pp. 1885-1890.

[29] T. Moss, "Lead salt photoconductors," *Proceedings of the IRE,* vol. 43, 1955, pp. 1869-1881.

[30] A. Rogalski, "HgCdTe infrared detector material: history, status and outlook," *Reports on Progress in Physics,* vol. 68, pp. 2267-2336, 2005.

[31] P. Richards, "Bolometers for infrared and millimeter waves," *Journal of Applied Physics,* vol. 76, pp. 1-24, 1994.

[32] A. Hossain and M. H. Rashid, "Pyroelectric detectors and their applications," *Industry Applications, IEEE Transactions on,* vol. 27, pp. 824-829, 1991.

[33] S. Weckmann, "Dynamic electrothermal model of a sputtered thermopile thermal radiation detector for earth radiation budget applications," Dissertation, Virginia Polytechnic Institute and State University, 1997.

[34] F. J. Meca Meca, M. Mazo Quintas, F. J. Rodríguez Sánchez, and P. Ramos Sainz, "Infrared temperature measurement system using photoconductive PbSe sensors without radiation chopping," *Sensors and Actuators A: Physical,* vol. 100, pp. 206-213, 2002.

[35] F. J. Meca Meca, M. Mazo Quintas, and F. J. Rodriguez Sánchez, "Optimum conditioning of PbSe photoconductive detectors in measurements without chopping," *Sensors and Actuators A: Physical,* vol. 84, pp. 45-52, 2000.

[36] Hamamatsu Photonics, "Characteristics and use of infrared detectors," 2004.

[37] G. Vergara, M. Montojo, M. Torquemada, M. Rodrigo, F. Sánchez, L. Gómez*, et al.*, "Polycrystalline lead selenide: the resurgence of an old infrared detector," *Opto-Electronics Review,* vol. 15, pp. 110-117, 2007.

[38] A. Rogalski, K. Adamiec, and J. Rutkowski, *Narrow-Gap Semiconductor Photodiodes*, 1st ed. Bellingham, WA: SPIE Press, 2000.

[39] T. Iuchi and A. Jono, "New radiation thermometer for near room temperature," *Measurement,* vol. 16, pp. 257-263, 1995.

[40] W. Lang, K. Kühl, and E. Obermeier, "A thin-film bolometer for radiation thermometry at ambient temperature," *Sensors and Actuators A: Physical,* vol. 22, pp. 473-477, 1989

[41] J. Fischer, M. Battuello, M. Sadli, M. Ballico, S. N. Park, P. Saunders*, et al.*, "Uncertainty budgets for realization of ITS-90 by radiation thermometry," in *AIP Conference Proceedings*, Chicago, Illinois, USA, 2003, pp. 631-638.

[42] J. Novak and P. Elias, "A silicon-InGaAs tandem photodetector for radiation thermometry," *Measurement Science and Technology,* vol. 6, pp. 1547-1549, 1995.

[43] OSI Optoelectronics, "Dual Sandwich Detector Series," 2013.

[44] C. Oliver and E. Pike, "Measurement of low light flux by photon counting," *Journal of Physics D: Applied Physics,* vol. 1, pp. 1459-1468, 1968.

[45] P. Coates and J. Andrews, "Measurement of thermodynamic temperatures with the NPL photon-counting pyrometer," *Temperature, Its Measurement and Control in Science and Industry,* vol. 5, pp. 109-114, 1982.

[46] Hamamatsu Photonics, "Characteristics and use of Si APD (Avalanche Photodiode)," 2004.

[47] A. Rogalski, "New material systems for third generation infrared photodetectors," *Opto-Electronics Review,* vol. 16, pp. 458-482, 2008.

[48] R. Rehm, M. Walther, F. Rutz, J. Schmitz, A. Wörl, J.-M. Masur*, et al.*, "Dual-Color InAs/GaSb Superlattice Focal-Plane Array Technology," *Journal of electronic materials,* vol. 40, pp. 1738-1743, 2011.

[49] N. Gautam, M. Naydenkov, S. Myers, A. Barve, E. Plis, T. Rotter*, et al.*, "Three color infrared detector using InAs/GaSb superlattices with unipolar barriers," *Applied Physics Letters,* vol. 98, p. 121106, 2011.

[50] H. Kim, E. Plis, A. Khoshakhlagh, S. Myers, N. Gautam, Y. Sharma, L. Dawson, S. Krishna, S. Lee, and S. Noh, "Performance improvement of InAs/GaSb strained layer superlattice detectors by reducing surface leakage currents with SU-8 passivation," *Applied Physics Letters,* vol. 96, p. 033502, 2010.

[51] E. Plis, J. B. Rodriguez, H. S. Kim, G. Bishop, Y. D. Sharma, L. R. Dawson, S. Krishna, S. J. Lee, C. E. Jones, and V. Gopal, "Type II InAs/GaSb strain layer superlattice detectors with p-on-n polarity," *Applied Physics Letters*, vol. 91, p. 133512, 2007.

[52] M. Walther, J. Schmitz, R. Rehm, S. Kopta, F. Fuchs, J. Fleißner*, et al.*, "Growth of InAs/GaSb short-period superlattices for high-resolution mid-wavelength infrared focal plane array detectors," *Journal of Crystal growth,* vol. 278, pp. 156-161, 2005.

[53] E. Plis, J. Rodriguez, G. Balakrishnan, Y. Sharma, H. Kim, T. Rotter, and S. Krishna, "Mid-infrared InAs/GaSb strained layer superlattice detectors with nBn design grown on a GaAs substrate," *Semiconductor Science and Technology,* vol. 25, p. 085010, 2010.

[54] Y. Wei, A. Hood, H. Yau, A. Gin, M. Razeghi, M. Z. Tidrow, and V. Nathan, "Uncooled operation of type-II InAs/GaSb superlattice photodiodes in the midwavelength infrared range," *Applied Physics Letters*, vol. 86, p. 233106, 2005.

[55] S. A. Pour, E. Huang, G. Chen, A. Haddadi, B. M. Nguyen, and M. Razeghi, "High operating temperature midwave infrared photodiodes and focal plane arrays based on type-II InAs/GaSb superlattices," *Applied Physics Letters,* vol. 98, p. 143501, 2011.

[56] E. K. W. Huang, P. Y. Delaunay, B. M. Nguyen, S. A. Pour, and M. Razeghi, "Photovoltaic MWIR Type-II Superlattice Focal Plane Array on GaAs Substrate," *IEEE Journal of Quantum Electronics,* vol. 46, pp. 1704-1708, 2010.

[57] S. D. Gunapala, S. Bundara, J. K. Liu, W. Hong, M. Sundaram, P. D. Maker*, et al.*, "Long-wavelength 640×486 GaAs/AlGaAs quantum well infrared photodetector snap-shot camera," *IEEE Transactions on Electron Devices,* vol. 45, pp. 1890-1895, 1998.

[58] Ü. Sakoğlu, J. S. Tyo, M. M. Hayat, S. Raghavan, and S. Krishna, "Spectrally adaptive infrared photodetectors with bias-tunable quantum dots," *JOSA B,* vol. 21, pp. 7-17, 2004.

[59] Ü. Sakoglu, M. M. Hayat, J. S. Tyo, P. Dowd, S. Annamalai, K. T. Posani*, et al.*, "Statistical adaptive sensing by detectors with spectrally overlapping bands," *Applied optics,* vol. 45, pp. 7224-7234, 2006.

[60] H.-S. Ling, S.-Y. Wang, W.-C. Hsu, and C.-P. Lee, "Voltage-tunable dual-band quantum dot infrared photodetectors for temperature sensing," *Optics Express,* vol. 20, pp. 10484-10489, 2012.

[61] S. Krishna, D. Forman, S. Annamalai, P. Dowd, P. Varangis, T. Tumolillo, A. Gray, J. Zilko, K. Sun, and M. Liu, "Demonstration of a 320x256 two-color focal plane array using InAs/InGaAs quantum dots in well detectors," *Applied Physics Letters,* vol. 86, p. 193501, 2005.

[62] Hamamatsu Photonics, *Si APD - S2381 to S2385, S5139, S8611, S3884, S4315 series datasheet*. Available: http://sales.hamamatsu.com/assets/pdf/parts_S/s2381_etc_kapd1007e09.pdf, (2010).

[63] Hamamatsu Photonics, *InGaAs APD - G8931-04*. Available: http://www.hamamatsu.com/resources/pdf/ssd/g8931-04_kapd1018e03.pdf, (2009)

[64] Hamamatsu Photonics, *Si APD array – S8550-02*. Available: http://www.hamamatsu.com/resources/pdf/ssd/s8550-02_kapd1031e01.pdf, (2012).

[65] F. Laforce, "Low noise optical receiver using Si APD," *Proc. SPIE,* vol. 7212, p. 721210, 2009.

[66] R.J. McIntyre, "Recent developments in silicon avalanche photodiodes," *Measurement,* vol. 3, pp. 146-152, 1985.

[67] J. C. Campbell, S. Demiguel, F. Ma, A. Beck, X. Guo, S. Wang*, et al.*, "Recent advances in avalanche photodiodes," *IEEE Journal of Selected Topics in Quantum Electronics,* vol. 10, pp. 777-787, 2004.

[68] B. Streetman and S. Banerjee, *Solid State Electronic Devices*, 5 ed. vol. 1. Upper Saddle River, New Jersey: Prentice Hall, 2000.

[69] G. Buller and R. Collins, "Single-photon generation and detection," *Measurement Science and Technology,* vol. 21, p. 012002, 2010.

[70] R. H. Hadfield, "Single-photon detectors for optical quantum information applications," *Nature Photonics,* vol. 3, pp. 696-705, 2009.

[71] S. Bloom, E. Korevaar, J. Schuster, and H. Willebrand, "Understanding the performance of free-space optics ," *Journal of optical Networking,* vol. 2, pp. 178-200, 2003.

[72] P. Eardley and D. Wisely, "1 Gbit/s optical free space link operating over 40 m system and applications," in *IEE Proceedings-Optoelectronics*, 1996, pp. 330-333.

[73] M. Ren, X. Gu, Y. Liang, W. Kong, E. Wu, G. Wu*, et al.*, "Laser ranging at 1550 nm with 1-GHz sine-wave gated InGaAs/InP APD single-photon detector," *Optics Express,* vol. 19, pp. 13497-13502, 2011.

[74] J. Kataoka, T. Toizumi, T. Nakamori, Y. Yatsu, Y. Tsubuku, Y. Kuramoto*, et al.*, "In-orbit performance of avalanche photodiode as radiation detector on board the picosatellite Cute-1.7+ APD II," *Journal of Geophysical Research: Space Physics (1978–2012),* vol. 115, 2010.

[75] M. J. Hobbs, C. H. Tan, and J. R. Willmott, "Evaluation of phase sensitive detection method and Si avalanche photodiode for radiation thermometry," *Journal of Instrumentation,* vol. 8, p. P03016, 2013.

[76] M. Razeghi, S. A. Pour, E. Huang, G. Chen, A. Haddadi, and B. Nguyen, "Type-II InAs/GaSb photodiodes and focal plane arrays aimed at high operating temperatures," *Opto-Electronics Review,* vol. 19, pp. 261-269, 2011.

[77] J. Chen, Y. Zhou, Z. Xu, J. Xu, Q. Xu, H. Chen*, et al.*, "InAs/GaSb type-II superlattice mid-wavelength infrared focal plane array detectors grown by molecular beam epitaxy," *Journal of Crystal Growth,* vol. 378, pp. 596-599, 2013.

[78] E. Plis, B. Klein, S. Myers, N. Gautam, and S. Krishna, "(111) InAs/GaSb type-II strained layer superlattice material for high operating temperature detection," *physica status solidi (c),* vol. 10, pp. 748-751, 2013.

[79] J. B. Rodriguez, P. Christol, A. Ouvrard, F. Chevrier, P. Grech, and A. Joullie, “Uncooled InAs/GaSb superlattice photovoltaic detector operating in

the mid-wavelength infrared range," *Electronics Letters*, vol. 41, pp. 362-363, 2005.

[80] B. M. Nguyen, D. Hoffman, E. K. Huang, S. Bogdanov, P. Y. Delaunay, M. Razeghi, and M. Z. Tidrow, "Demonstration of midinfrared type-II InAs/GaSb superlattice photodiodes grown on GaAs substrate," *Applied Physics Letters,* vol. 94, p. 223506, 2009.

[81] H. S. Kim, E. Plis, N. Gautam, S. Myers, Y. Sharma, L. R. Dawson*, et al.*, "Reduction of surface leakage current in InAs/GaSb strained layer long wavelength superlattice detectors using SU-8 passivation," *Applied Physics Letters,* vol. 97, p. 143512, 2010.

[82] S. A. Pour, B. Nguyen, S. Bogdanov, E. Huang, and M. Razeghi, "Demonstration of high performance long wavelength infrared type II InAs/GaSb superlattice photodiode grown on GaAs substrate," *Applied Physics Letters,* vol. 95, p. 173505, 2009

[83] S. Bogdanov, B.-M. Nguyen, A. Hoang, and M. Razeghi, "Surface leakage current reduction in long wavelength infrared type-II InAs/GaSb superlattice photodiodes," *Applied Physics Letters,* vol. 98, p. 183501, 2011.

[84] S. L. Tan, Y. L. Goh, S. Dip Das, S. Zhang, C. H. Tan, J. P. David*, et al.*, "Dry etching and surface passivation techniques for type-II InAs/GaSb superlattice infrared detectors," in *SPIE Security + Defence*, p. 783814, 2010.

[85] A. V. Barve, S. J. Lee, S. K. Noh, and S. Krishna, "Review of current progress in quantum dot infrared photodetectors," *Laser & Photonics Reviews,* vol. 4, pp. 738-750, 2010.

[86] T. E. Vandervelde, M. C. Lenz, E. Varley, A. Barve, J. Shao, R. V. Shenoi*, et al.*, "Quantum dots-in-a-well focal plane arrays," *Selected Topics in Quantum Electronics, IEEE Journal of,* vol. 14, pp. 1150-1161, 2008.

[87] S. Krishna, S. D. Gunapala, S. V. Bandara, C. Hill, and D. Z. Ting, "Quantum dot based infrared focal plane arrays," *Proceedings of the IEEE,* vol. 95, pp. 1838-1852, 2007.

[88] E. T. Kim, A. Madhukar, Z. Ye, and J. C. Campbell, "High detectivity InAs quantum dot infrared photodetectors," *Applied physics letters,* vol. 84, p. 3277, 2004.

[89] S. Tsao, H. Lim, H. Seo, W. Zhang, and M. Razeghi, "InP-Based Quantum-Dot Infrared Photodetectors With High Quantum Efficiency and High-Temperature Imaging," *IEEE Sensors Journal,* vol. 8, pp. 936-941, 2008.

[90] A. V. Barve, T. Rotter, Y. Sharma, S. J. Lee, S. K. Noh, and S. Krishna, "Systematic study of different transitions in high operating temperature quantum dots in a well photodetectors," *Applied Physics Letters,* vol. 97, p. 061105, 2010.

[91] P. Bhattacharya, X. Su, S. Chakrabarti, G. Ariyawansa, and A. Perera, "Characteristics of a tunnelling quantum-dot infrared photodetector operating at room temperature," *Applied Physics Letters,* vol. 86, p. 191106, 2005.

[92] S. Chakrabarti, A. Stiff-Roberts, P. Bhattacharya, S. Gunapala, S. Bandara, S. Rafol, and S. Kennerly, "High-temperature operation of InAs-GaAs quantum-dot infrared photodetectors with large responsivity and detectivity," *Photonics Technology Letters, IEEE,* vol. 16, pp. 1361-1363, 2004.

[93] S. F. Tang, S. Y. Lin, and S. C. Lee, "Near-room-temperature operation of an InAs/GaAs quantum-dot infrared photodetector," *Applied Physics Letters,* vol. 78, p. 2428, 2001.

[94] H. Lim, S. Tsao, W. Zhang, and M. Razeghi, "High-performance InAs quantum-dot infrared photodetectors grown on InP substrate operating at room temperature," *Applied physics letters,* vol. 90, p. 131112, 2007.

[95] S. Krishna, "Quantum dots-in-a-well infrared photodetectors," *Infrared physics & technology,* vol. 47, pp. 153-163, 2005.

[96] S. Raghavan, P. Rotella, A. Stintz, B. Fuchs, S. Krishna, C. Morath*, et al.*, "High-responsivity, normal-incidence long-wave infrared ($\lambda \sim 7.2$ μm) InAs/$In_{0.15}Ga_{0.85}As$ dots-in-a-well detector," *Applied physics letters,* vol. 81, pp. 1369-1371, 2002.

[97] P. Aivaliotis, E. Zibik, L. Wilson, J. Cockburn, M. Hopkinson, and N. Vinh, "Two photon absorption in quantum dot-in-a-well infrared photodetectors," *Applied Physics Letters,* vol. 92, p. 023501, 2008.

[98] R. Attaluri, S. Annamalai, K. Posani, A. Stintz, and S. Krishna, "Effects of Si doping on normal incidence InAs⁄ InGaAs dots-in-well quantum dot infrared photodetectors," *Journal of applied physics,* vol. 99, p. 083105, 2006.

[99] S. D. Gunapala, S. V. Bandara, C. J. Hill, D. Z. Ting, J. K. Liu, B. Rafol*, et al.*, "640× 512 pixels long-wavelength infrared (LWIR) quantum-dot infrared photodetector (QDIP) imaging focal plane array," *IEEE Journal of Quantum Electronics,* vol. 43, pp. 230-237, 2007.

[100] P. Vines, C. H. Tan, J. P. R. David, R. S. Attaluri, T. E. Vandervelde, S. Krishna*, et al.*, "Versatile spectral imaging with an algorithm-based spectrometer using highly tuneable quantum dot infrared photodetectors," *IEEE Journal of Quantum Electronics,* vol. 47, pp. 190-197, 2011.

[101] C. H. Tan, P. Vines, M. Hobbs, B. Anderson, M. Hugues, and J. David, Implementation of an algorithmic spectrometer using Quantum Dot Infrared Photodetectors," *Infrared Physics & Technology,* vol. 54, pp. 228-232, 2011.

[102] W.-Y. Jang, M. M. Hayat, J. S. Tyo, R. S. Attaluri, T. E. Vandervelde, Y. D. Sharma*, et al.*, "Demonstration of bias-controlled algorithmic tuning of quantum dots in a well (DWELL) midIR detectors," *IEEE Journal of Quantum Electronics,* vol. 45, pp. 674-683, 2009.

Chapter 2 – Background theory

2.1 Introduction

This chapter describes the basic theory behind radiation thermometry and the detectors evaluated in this work, along with their various figures of merit. Various measurement precautions, which are required when performing practical radiation thermometry measurements, are highlighted, and how they affect the design of radiation thermometers. The chapter finishes by introducing the novel theory of the infrared algorithmic spectrometer (IRAS) implemented for ratio radiation thermometry.

2.2 Radiation thermometry theory

Detailed theory of radiation thermometry has been presented by other authors [1][2][3]. These are recommended for further reading.

2.2.1 Radiation thermometry modelling

To demonstrate the relationship between Planck's Law and radiation thermometry, theoretical modelling of the photocurrent can be performed. Here the analysis was carried out using data from a Hamamatsu Si photodiode model S2386-45K [4] and the setup parameters discussed in section 3.3.2. Planck's Law, equation (1.2), is used to calculate *W(λ)* emitted from the blackbody source. Equation (2.1) can then be used to calculate the power incident per unit wavelength upon the photodiode [5], *P(λ)*.

$$P(\lambda) = \mathrm{F}.\mathrm{W}(\lambda).\sin^2\left(\frac{\theta}{2}\right) A.M_F.T_F.\cos(\varphi) \qquad (2.1)$$

φ is the angle of incidence and θ is the optical FOV, assuming no focusing lens, where $\theta = 2\ tan^{-1}(\rho/D)$. D is the distance between the blackbody source and the photodiode, and ρ is the blackbody aperture radius. T_F is the transmission factor of the transmission medium (e.g: air) and F is the magnification provided by the

focusing lens. A chopper modulation factor, M_F, is included for PSD calculation, but is taken as 1 for DD calculation. Figure 2.1 shows a diagram illustrating these modelling parameters.

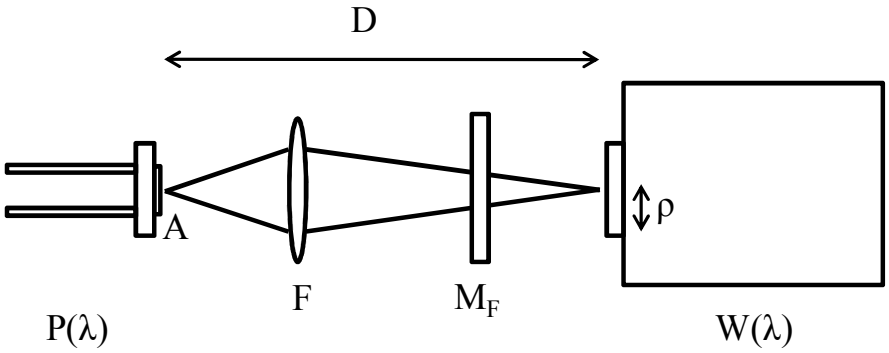

Figure 2.1 – Setup used for radiation thermometry modelling

The photocurrent generated by the photodiode can be calculated as

$$i_{ph} = \int_{\lambda_1}^{\lambda_2} R(\lambda)\mathrm{P}(\lambda).\,\mathrm{d}\lambda \tag{2.2}$$

where $R(\lambda)$ is the spectral response of the photodiode. This photocurrent can be converted into an expected output voltage by multiplying it by the circuit gain, G. The values of the parameters used in this model are listed in Table 2.1.

Parameter	**Value**	**Parameter**	**Value**
h	6.626×10^{-34} J.s	T_F	~1 over this short distance
c	2.998×10^{8} m.s^{-1}	ρ	5.1 mm
λ	300 to 1100 nm	D	300 mm
k	1.381×10^{-23} J.K^{-1}	F	~43.5
A	17.9 mm^2	M_F	0.37 for PSD (1 for DD)
T_{BB}	Blackbody temperature (K)	$R(\lambda)$	300 to 1100 nm, with peak of 0.6 A/W at 960 nm
φ	0 °	G	1×10^{6} V/A

Table 2.1 – Parameters used for modelling

The theoretical output voltage for the Si photodiode thermometer system is calculated as shown in Figure 2.2(a), for both PSD and DD. Figure 2.2(b) shows the natural logarithm of the output voltage plotted against the inverse of T_{BB} in kelvin.

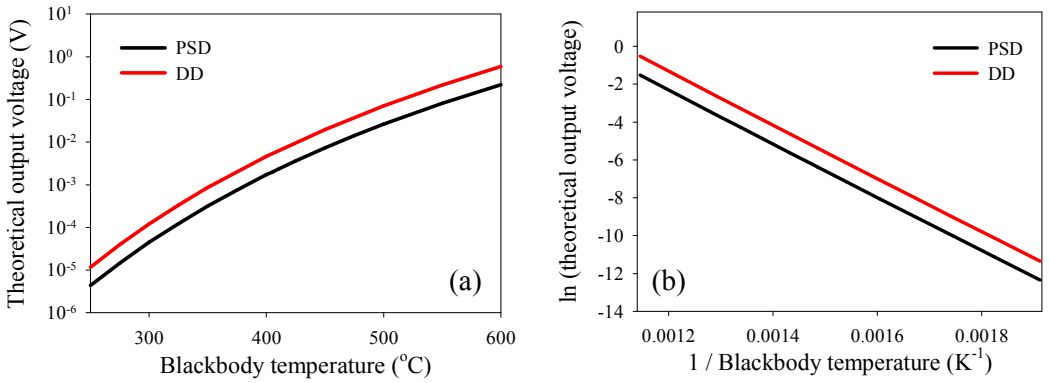

Figure 2.2 – (a) Theoretical output voltage with T_{BB} using PSD and DD methods and (b) natural logarithm of output voltage against inverse of T_{BB} using PSD and DD methods

Reduced T_{BB} leads to a reduced output voltage, corresponding to a reduction in the emitted blackbody power. There is also a clear reduction in the output voltage by a factor of 0.37 when using the PSD method; this corresponds to the chopper modulation factor. Additionally, Figure 2.2(b) shows that the natural logarithm of the output signal varies linearly with $1/T_{BB}$ for both the PSD and DD methods. This linearity helps to relate the output of the thermometer to the target object temperature in a practical system. This model does not incorporate the signal-to-noise ratio (SNR), a parameter which demonstrates the key benefits of PSD over DD. This parameter is discussed in the next section, along with the temperature error.

2.2.2 Radiation thermometer SNR, temperature error and *%/°C*

A measure of the stability and fluctuation of a radiation thermometer can be obtained by calculating the SNR and temperature error at the thermometer output. The SNR is defined as the mean output (voltage or photocurrent) of the measurement divided by the standard deviation of that output. The higher the SNR, the more stable the thermometer is. Essentially, its relationship is a ratio between the photocurrent and the noise.

Alternatively, the fluctuation at the thermometer output can be related directly to a practical temperature by calculation of the temperature error for the measurement. This is done by first calculating the thermometer's percentage change in its output for a 1 ^{o}C rise in the target object's temperature, $\%/^{o}C$ [6], as shown in equation (2.3), and can be derived from the Wien Approximation, with the full derivation included in Appendix B.

$$\%/°C = 100 \times \frac{c_2}{\lambda_m T^2} \tag{2.3}$$

λ_m is the thermometer's mean effective wavelength [6], and is the wavelength at which the photodiode's spectral response intercepts that of the blackbody emission spectrum. λ_m therefore represents a point weighted across the T_{BB} range [7] and this method is used to effectively simplify calculations by turning a broad range of wavelengths into a single monochromatic wavelength [8][9][10]. λ_m is calculated by dividing c_2 by the gradient of the natural logarithm of the output voltage against the inverse of T_{BB}. The percentage error in the thermometer's output, $\%_{error}$, can then be divided by $\%/^{o}C$ to produce a temperature error. Figure 2.3 shows the output voltage fluctuation for a Si photodiode over a 2 minute period at T_{BB} = 300 ^{o}C.

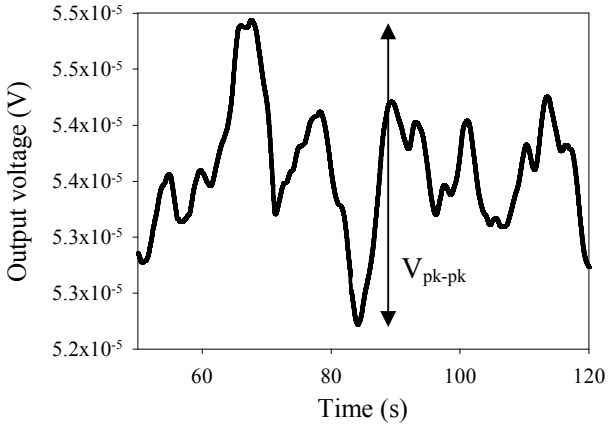

Figure 2.3 – Output voltage fluctuation for Si photodiode over a 2 minute period at T_{BB} = 300 ^{o}C

The output fluctuation can be converted to a percentage error using equation (2.4), where $V_{pk\text{-}pk}$ is the peak-to-peak fluctuation in the output voltage and V_{mean} is the mean output voltage.

$$\%_{error} = 100 \times \left(\frac{V_{pk-pk}/2}{V_{mean}} \right) \tag{2.4}$$

In addition, $\%/^{o}C$ can also be used to estimate the amount of error in the measured temperature due to uncertainty in the target object's emissivity. A high value of $\%/^{o}C$ leads to a reduction in the error due to such emissivity uncertainty. Figure 2.4 shows how this theoretical value varies with temperature for the Si photodiode modelled in section 2.2.1 for both PSD and DD, with both methods producing identical results.

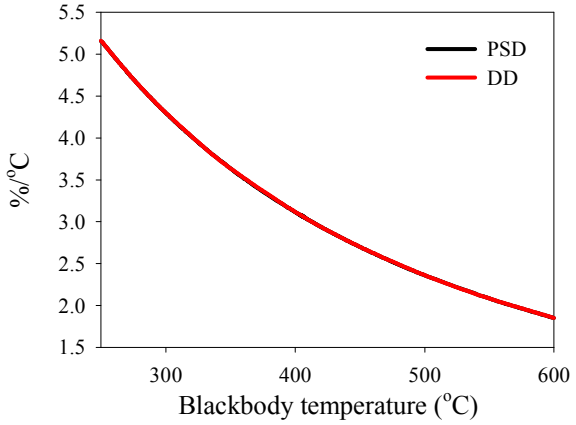

Figure 2.4 – $\%/^{o}C$ with T_{BB} for Si photodiode

It can be deduced from equation (2.3) that $\%/^{o}C$ is higher at shorter wavelengths. Figure 2.5(a) shows $\%/^{o}C$ for thermometers operating at different wavelengths. Across the T_{BB} range, the shorter wavelength thermometer produces the highest $\%/^{o}C$, and will therefore result in the lowest error due to emissivity uncertainty. An example of such reduction in the measurement error is shown in Figure 2.5(b), assuming that the target object has an emissivity uncertainty of ±10 %.

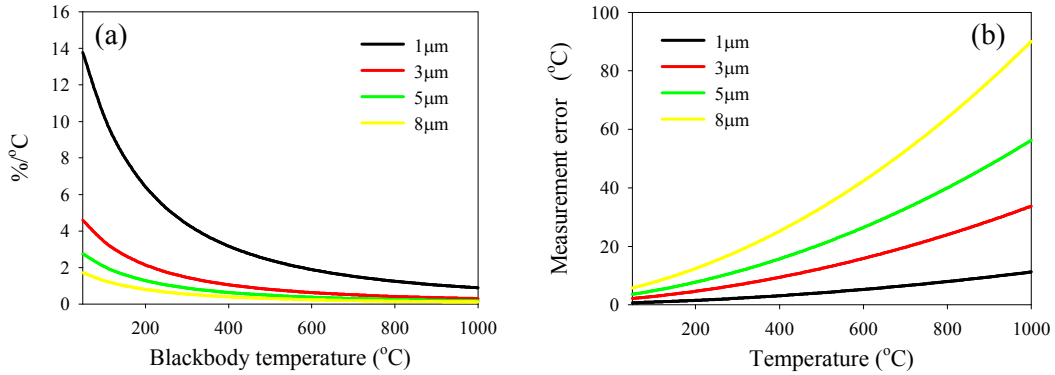

Figure 2.5 – (a) *%/°C* with T_{BB} for varied wavelength thermometers and (b) measurement error for a target object with ±10 % uncertainty in emissivity with temperature for varied wavelength thermometers

The measurement error is clearly lower when using a shorter wavelength thermometer, with this becoming particularly clear at higher temperature. This therefore confirms that shorter wavelength detectors should be the preferred choice of detector within the thermometer. However, this is not always possible due to the need for the detector to also satisfy the wavelength requirements which correspond to the target object's radiated emission. This highlights the need for more sensitive detectors operating at shorter wavelengths for the measurement of lower temperatures.

2.2.3 Ratio radiation thermometry

The ratio radiation thermometry technique is another way of dealing with the temperature measurement of target objects with unknown emissivity. The basic principle of this technique is the calculation of a ratio between the photocurrents produced by detectors operating over two separate wavelengths bands. This ratio is therefore proportional to the temperature of the target object. Equations (2.5) and (2.6) show the radiance over the spectral range for a detector with two different wavelengths, using the Wien Approximation.

$$L_{\lambda_1} = \varepsilon_{\lambda_1} c_1 \lambda_1^{-5} \exp\left(\frac{-c_2}{\lambda_1 T}\right) \quad (2.5)$$

$$L_{\lambda_2} = \varepsilon_{\lambda_2} c_1 \lambda_2^{-5} \exp\left(\frac{-c_2}{\lambda_2 T}\right) \quad (2.6)$$

$L_{\lambda 1}$ and $\varepsilon_{\lambda 1}$ are the radiance and emissivity over the spectral range of the first wavelength band, and $L_{\lambda 2}$ and $\varepsilon_{\lambda 2}$ are the radiance and emissivity over the spectral range of the second wavelength band. λ_1 and λ_2 are the mean effective wavelengths of the first and second wavelength band, respectively. Dividing equation (2.5) by equation (2.6) gives the ratio, which can be shown by equation (2.7).

$$Ratio = \frac{L_{\lambda_1}}{L_{\lambda_2}} = \frac{\varepsilon_{\lambda_1}}{\varepsilon_{\lambda_2}} \left(\frac{\lambda_1}{\lambda_2}\right)^{-5} \exp\left[\frac{c_2}{T}\left(\frac{1}{\lambda_2} - \frac{1}{\lambda_1}\right)\right] \quad (2.7)$$

Therefore, using the greybody assumption (as will be discussed further in section 2.2.4) that emissivity is independent of wavelength, i.e. $\varepsilon_{\lambda 1} = \varepsilon_{\lambda 2}$, the measured signal will therefore be independent of emissivity [11] and the temperature can be successfully measured.

Taking this principle further, this technique also allows the thermometer to cope with an obscured FOV. For instance, if the FOV becomes obscured, the amount of photocurrent produced by each detector is reduced equally, whilst the ratio stays the same. Hence, the temperature can still be successfully measured.

A ratio radiation thermometer can be analysed in the same way as a single wavelength thermometer. However *%/°C,* in this case, allows for an analysis of the effect of the non-greyness in the target object's emission upon the measurement. For such an analysis, λ_m for a ratio radiation thermometer can be calculated by combining λ_1 and λ_2, as in equation (2.8).

$$\lambda_m = \frac{\lambda_1 \lambda_2}{\lambda_1 - \lambda_2} \tag{2.8}$$

It should be noted that λ_m for a ratio radiation thermometer will be longer than for a single wavelength thermometer. Any variation in the non-greyness will lead to greater error in a ratio radiation thermometer than variation in emissivity for single wavelength thermometers. However, in practice, non-greyness varies less than emissivity [6].

Although ratio radiation thermometers are used for the measurement of targets with unknown emissivity values, the measurement may well contain a large amount of error. Therefore, it is often better to use a single wavelength instrument with a 'best guess' of the emissivity, which leads to reduced error. However, a ratio radiation thermometer is still a very useful tool for temperature measurement with unknown emissivity.

2.2.4 Radiation thermometry measurement precautions

The measurement of temperature using radiation thermometry requires several measurement precautions in practical systems. These will be discussed in this section.

I. **Emissivity:** As discussed in section 1.2.1, the emissivity of any object is a ratio between the energy radiated from that object and the energy radiated from a perfect blackbody at the same temperature [12]. It is an indication of the ability of that object to radiate energy. The emissivity of a perfect blackbody is 1, so the emissivity of all materials will be less than 1. It should be noted that perfect blackbody emitters do not exist in reality, with blackbody sources, such as those used in this work, having emissivities > 0.99. In contrast, the reflectivity of an object is a measure of the energy reflected off that object's surface. It is related to emissivity such that for opaque objects emissivity = 1 – reflectivity. Figure 2.6 demonstrates this principle for an object with an emissivity of 0.7. Emissivity presents

challenges to radiation thermometry measurements. For example, if the emissivity is not taken into account when the thermometer is used, the measured temperature will be incorrect. If the emissivity of a target object is, say, 0.7, only 70 % of the energy will escape the object, as in Figure 2.6. In practice, due to the variable nature of emissivity across different target objects, a variable emissivity control can be built into the system for thermometers used for multiple applications. The determination of, and accounting for, target object emissivity is a particular challenge in radiation thermometry.

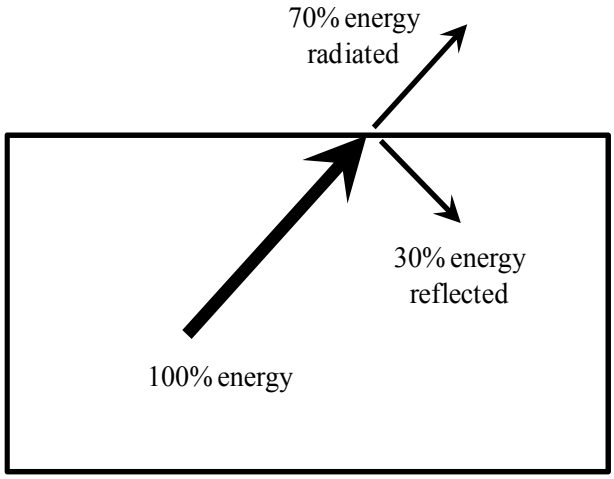

Figure 2.6 – Radiated and reflected energy for an object with emissivity = 0.7

Several measurement and design techniques have been developed to cope with unknown emissivity [6]. The emitted energy from hot target objects varies rapidly at shorter wavelengths, whilst it varies more slowly at longer wavelengths. Therefore, shorter wavelength thermometers are chosen due to being able to cope better with unknown emissivity, as discussed in section 2.2.2. For some applications, it is possible to paint the target object with high and constant emissivity paint [13]. This means that the object will appear to have a large and constant emissivity across the wavelength range, making the measurement of the temperature more accurate. Alternatively, a ratio radiation thermometer could be utilised to cope with the emissivity being less than 1.

II. **Non-greyness:** If a ratio radiation thermometer is used, care needs to be taken over the target object emission's non-greyness. Using the greybody assumption that emissivity is independent of wavelength, Figure 2.7 shows the radiated emission comparison between a perfect blackbody, a perfect greybody and a non-perfect greybody at T_{BB} = 600 ^{o}C. For the perfect greybody with an emissivity of 0.7, it is clear that any reduction in the spectral radiance is equal across the wavelength range. However, for a non-perfect greybody, the spectral radiance has stronger wavelength dependence. For such measurement scenarios, care needs to be taken to ensure this non-greyness is accounted for. One such precaution is to use narrow spectral filters to make it easier to target grey areas in the emitted spectrum of surfaces. This scenario also highlights the need to develop a ratio radiation thermometer with adjustable filters. Such versatile thermometers would allow the filters to be tuned to wavelengths which have the same emissivity, and therefore remove the error due to non-greyness.

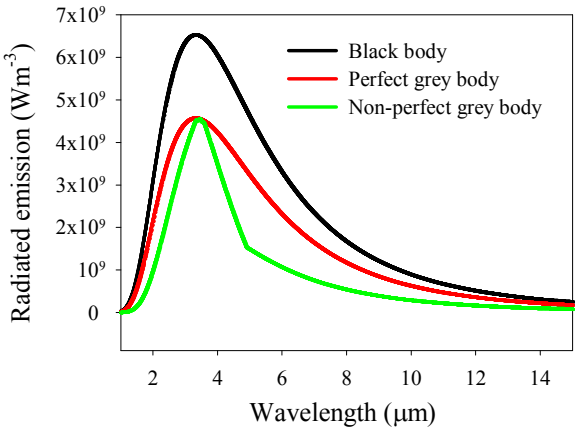

Figure 2.7 – Radiated emission for blackbody, perfect greybody and non-perfect greybody at T_{BB} = 600 ^{o}C

III. **Field of view:** The FOV, illustrated in Figure 2.8, of a radiation thermometer is effectively what the thermometer 'sees'. The FOV is optimised for the thermometer in order to focus the target object onto the detector. If the FOV were to become obscured, or the lens system damaged, inaccuracies would arise in the measurement. Therefore, it is important to design the optics

system such that it sees the target object with nothing else obscuring the FOV.

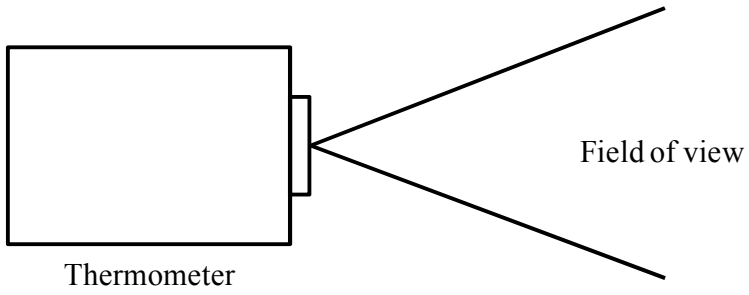

Figure 2.8 – FOV of radiation thermometer

IV. **Size-of-source effect:** Ideally the FOV of a radiation thermometer is well defined, but this can be prevented by imperfections within the optical system. This can lead to radiation from outside the FOV contributing to the measurement, whilst not including radiation within the FOV. This leads to the measured signal becoming dependent on the target's size, as well as the distribution of the radiance surrounding the target object [2]. This is known as the size-of-source effect. It can be corrected for by normalising the fixed point calibration of the thermometer to a given reference diameter [14].

V. **Transmission medium:** There are specific atmospheric windows within the IR spectrum, as defined in section 1.2. There are wavelengths where the transmission through the atmosphere is very poor due to atmospheric absorption caused by molecules such as H_2O and CO_2. The exact amount of signal loss between the target object and the thermometer is dependent upon the distance between the two as well as the atmospheric conditions. The amount of such molecules in the atmosphere can vary daily due to aspects such as humidity. This will therefore correspond to daily variations in the measurement if precautions are not taken. In order to account for this, the thermometer needs to operate within the atmospheric windows, where the transmission is high. This minimises the influence of the atmospheric conditions. Detectors with tunable wavelength are desirable in order to

develop thermometers operating away from wavelengths with low transmission, whilst still maximising the detector's performance.

VI. **Transmission characteristics of target object:** Specific target objects, such as glass and plastic, have wavelength dependent transmission properties. Therefore, at wavelengths where the target is semi-transparent, radiation emitted from objects behind the target will contribute to the measurement, leading to an inaccurate reading. This is overcome by tuning the thermometer's wavelength to a specific target window where the target object is opaque. In the measurement of plastic and glass, for example, such windows are centred at 3.43 and 4.5 μm, respectively. Such measurement applications will also benefit from the use of detectors with tailored spectral response.

VII. **Reflected temperature:** The temperature of the surrounding environment also leads to challenges with temperature measurement, particularly if the background temperature is greater than the target temperature. The radiated energy from the higher temperature background will cause reflections which add to the signal measured by the thermometer, leading to measurement error. Corrections can be made by measuring the background signal separately and subtracting it from the total measured signal. The measurement of low temperature target objects faces a similar problem, with the detector itself causing a source of reflected energy radiation. A solution in a practical system would involve the measurement of the detector temperature using an internal sensor and then making suitable corrections.

VIII. **Detector characteristics:** The choice of infrared detector defines the temperature range which the radiation thermometer can measure. Use of the shortest possible wavelength detector is preferred due to reduced error from emissivity uncertainty. However, the measurement of lower temperature objects requires the use of longer wavelength detectors, but at the expense of increased error with emissivity variation. As well as low temperature measurements, longer wavelength detectors are required for applications

where transmission properties dictate the choice of wavelength. Unfortunately, longer wavelength detectors suffer from increased dark current which leads to increased noise. When taking all this into account, it is clear that there are a lot of considerations when choosing the detector technology to use. By developing and increasing the detector technologies available, it will offer greater flexibility for optimising radiation thermometers for specific applications. More sensitive detectors and wavelength tunable detectors are particular examples of where optimising the detector will improve radiation thermometer performance for specific applications.

2.3 Infrared detector technologies

This section describes the details of the three detector technologies evaluated in this work. More comprehensive descriptions of APDs [15][16][17], T2SLs [18][19][20] and QDIPs [19][21][22] can be found elsewhere.

2.3.1 Si APD

The advantage of APDs over simple p-n or p-i-n photodiodes is their large internal gain mechanism. This makes the APD more sensitive than simple photodiodes and leads to increased signal amplification, detection of weaker signals and faster speed operation. This increased sensitivity makes APDs highly attractive for radiation thermometry.

APDs are only beneficial to applications where the noise of the detector-amplifier combination is dominated by the amplifier. Figure 2.9 shows how the SNR for an APD-amplifier system varies with APD gain.

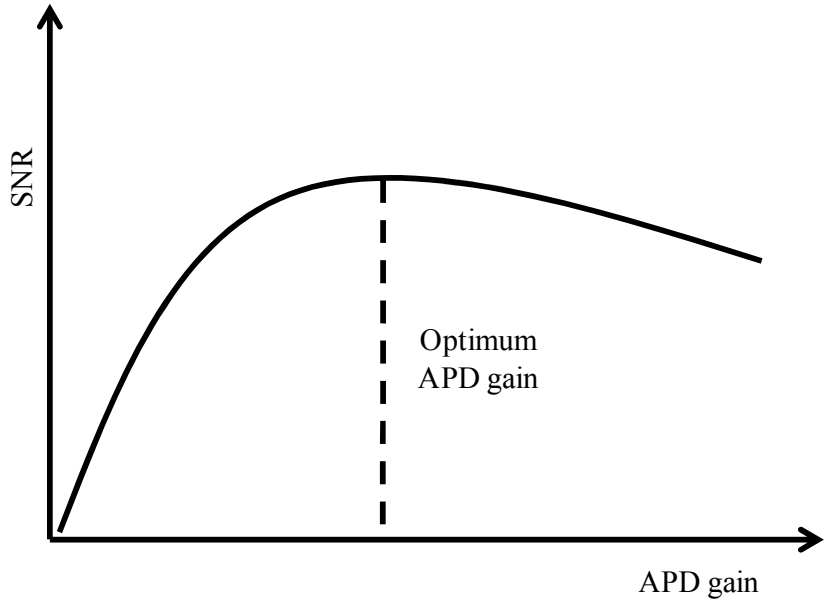

Figure 2.9 – SNR with APD gain for APD-amplifier system

As the gain of the APD increases, the SNR of the system increases until a point at which the APD gain is optimum for the APD-amplifier system. However, further increase in APD gain beyond this point leads to reduced SNR due to the dominance of excess avalanche noise at high gain. Below this optimum point, the APD's gain provides benefit to the system; above this point, the performance starts to degrade. The APD therefore offers increased amplification with no decrease in the overall SNR.

APDs achieve high internal gain by the impact ionisation process. In the presence of a high electric field, the free electrons in the conduction band, and the free holes in the valence band, can gain an energy that is greater than the threshold energy of impact ionisation. When the carriers subsequently collide into the lattice, impact ionisation occurs where they lose most of their energy. This results in electrons (holes) being promoted to the conduction (valence) band. The original and the new carriers drift, continue to gain energy, and repeat the impact ionisation process to produce an avalanche multiplication that yields a larger number of carriers collected than the number of photon generated carriers which started the process. The amount

of multiplication provided by the APD is known as the multiplication factor, *M*. Figure 2.10 shows how carriers impact ionise, leading to avalanche multiplication.

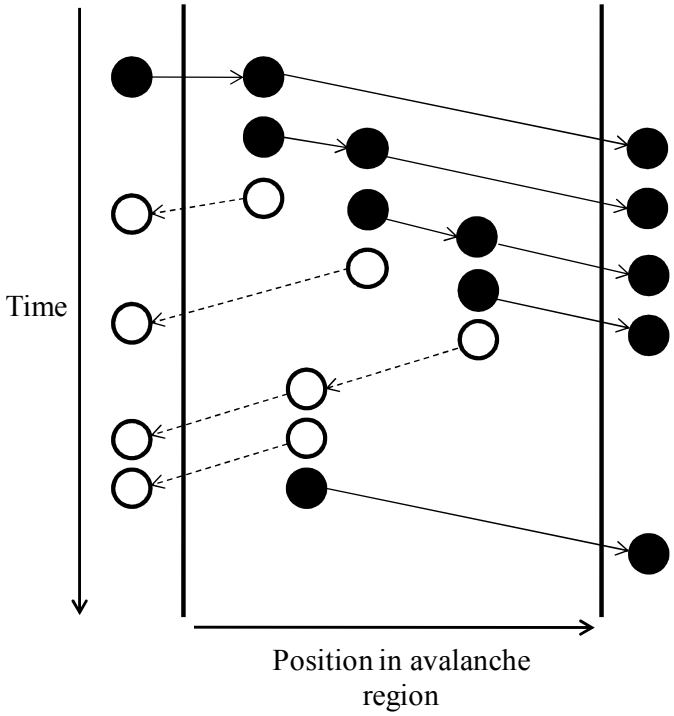

Figure 2.10 – Impact ionisation and avalanche multiplication

Excess noise within an APD can be minimised if the impact ionisation process is dominated by one type of carrier. This leads to significantly reduced fluctuations in the impact ionisation process, which occurs when both electrons and holes take part. The ionisation coefficients of electrons and holes, α and β, respectively, represent the average number of ionisation events that occur per unit distance the free carriers travel. If $\alpha = \beta$, the impact ionisation process is equal between electrons and holes, leading to high noise. However, in Si APDs $\alpha >> \beta$ indicating that impact ionisation is dominated by electrons. This makes Si APDs ideal for high gain and low noise applications. For radiation thermometry, this high gain of Si APDs should allow the measurement of lower temperatures.

2.3.2 MWIR InAs/GaSb T2SL

MWIR InAs/GaSb T2SL photodiodes are multi-quantum well detectors which contain barrier layers thin enough to allow tunnelling between the wells. The InAs

and GaSb materials have lattice constants that are slightly different. Bringing them together forms the strained layer superlattice (SLS) due to the lattice mismatch between InAs and GaSb. The spectral response for the T2SL is determined by the effective bandgap of the superlattice; the bandgaps of InAs and GaSb are 0.35 and 0.75 eV, respectively. Figure 2.11 shows that the valence band of the GaSb material is above the conduction band of the InAs by ΔE, which is the band overlap. However, this is not the effective bandgap of the superlattice, E_g. Wavefunction overlap leads to the formation of minibands, which are narrow subbands, being created out of the discrete energy states of the well. The value of E_g is the transition energy between the lowest subband in the conduction band of the InAs material and the highest subband in the valence band of the GaSb material, and it is temperature dependent. The band overlap increases as temperature increases, resulting in a reduction in the effective bandgap [23] and hence an increase in the cut-off wavelength [24]. The wavefunction overlap is also important in terms of optical absorption; a greater overlap leads to greater absorption due to an increased absorption coefficient.

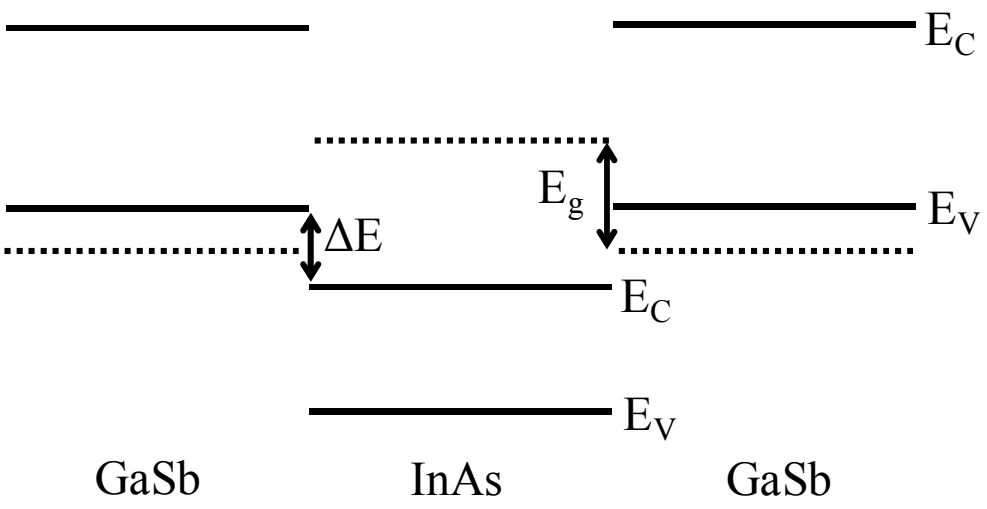

Figure 2.11 – InAs/GaSb T2SL band diagram

The bandgap and, ultimately, the spectral response, can be engineered by varying the ML period thickness of the InAs and GaSb material within the detector. Increase in the ML period results in a decrease in the effective bandgap, and thus an increase in

the cut-off wavelength. However, this leads to a decrease in the wavefunction overlap and therefore reduced optical absorption. In addition to the wavefunction overlap, a large depletion region and low doping concentration in the absorption region is important for T2SLs. Within the depletion region of the T2SL, as with all conventional photodiodes, the carrier collection is at its maximum. Therefore, it is desirable that this is maximised through a low background doping concentration in the absorption region. Low absorption region doping leads to increased depletion due to reduced carriers available for diffusion. Therefore, a larger depletion region is required to satisfy the charge neutrality principle [25].

A major attraction of T2SLs is their spectral response tunability. The effective bandgap ranges from 400 to 100 meV, with the spectral response ranging from 3 to 30 μm, depending on the InAs and GaSb composition [24]. This wavelength tunability is highly attractive to radiation thermometry as it allows the potential to tune the detector's peak response for specific measurement applications dictated by transmission properties. Also attractive is the ability of T2SLs to detect normal incidence light, leading to increased responsivity and increased D*. In addition, the potential low dark current of T2SLs arises due to the spatial separation of the electrons and holes. This leads to low Auger recombination; a recombination process which involves the recombination energy being transferred to a third carrier. Therefore, this results in reduced dark current.

In order to optimise T2SL for high photocurrent and high operating temperature, it is important to ensure that the carriers can be successfully extracted from the detector. Several key parameters need to be taken into account for this to take place. Firstly, the amount of light which is absorbed by the material needs to be maximised. This is governed by the absorption coefficient, α_A, of the T2SL material. This parameter has previously been investigated in terms of its wavelength dependence [24]. Assuming a mean α_A of 4000 cm^{-1}, the amount of absorption achieved as a function of absorption region thickness can be calculated using the Beer-Lambert law, equation (2.9).

$$A(x) = A(0)e^{-\alpha_A x} \quad (2.9)$$

x is the thickness of the absorption region in cm, *A(0)* is the absorption for a thickness of 0 cm, and *A(x)* is the absorption for a thickness of x cm. Figure 2.12 shows the absorption as a function of absorption region thickness. From this, it is clear that a thicker absorption region is required to maximise photon absorption.

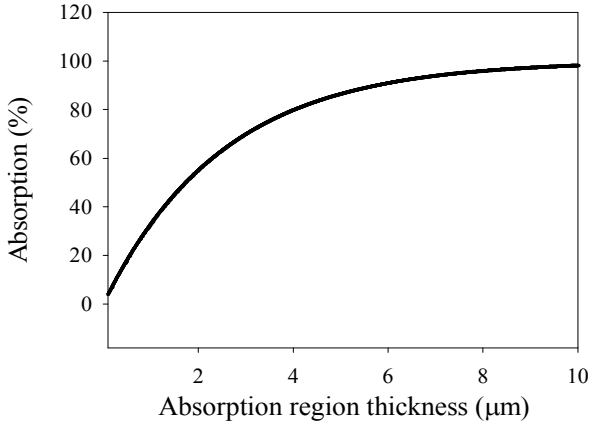

Figure 2.12 – Absorption as a function of absorption region thickness

Once absorbed, carrier recombination should be avoided to yield maximum photocurrent. Hence it is desirable to ensure the light is absorbed within the depletion region where carriers are immediately separated by the electric field and produce drift photocurrent [25]. Maximising the depletion region requires a low doping concentration in the absorption region. Under zero bias condition, part of the absorption region will remain undepleted. In this case, low absorption region doping is also required in order to maximise carrier extraction through maximised carrier lifetime and carrier diffusion length [26]. The carrier lifetime is the time it takes for the carrier to recombine after being created, with the diffusion length being the distance it travels before recombining. If the depletion region is small, carrier collection relies on carrier diffusion to reach the depletion region in order to get collected. In such a scenario, it is clear why this diffusion length needs to be maximised. Additionally, a nominally p-type background doping is preferable due to the minority electron diffusion length being significantly higher than that for holes in n-type material. This will lead to increased carrier collection and photocurrent than if

the background doping were nominal n-type [27]. If the material quality is poor, the carrier lifetime and diffusion lengths are reduced due to carriers recombining before reaching the depletion region. Therefore, optimised growth of the T2SL material is required in order to achieve a thick absorption region with low background doping to maximise carrier extraction.

2.3.3 QDIP

QDIPs are attractive due to their 3D carrier confinement, leading to the potential for low dark current and high temperature operation. This 3D confinement provides normal incidence operation and long excited state lifetimes. The basic QDIP structure, which incorporates a DWELL region, involves QDs, grown inside a QW by Stranski-Krastanow growth, with the QW surrounded by a material of higher bandgap. This DWELL region is repeated a specified number of times. Examples of materials used within the DWELL region are InAs, InGaAs and GaAs, for the QD, QW and higher bandgap materials, respectively. Each DWELL is separated by a potential barrier, such as AlGaAs. The electrons are trapped inside these QDs in a ground state, as shown in Figure 2.13. When photons are absorbed, the ground state electrons are excited into either (a) the continuum level directly or (b) the higher excited energy states, before tunnelling into the continuum level. Once the electrons reach the continuum level, they form a photocurrent under the influence of an applied electric field.

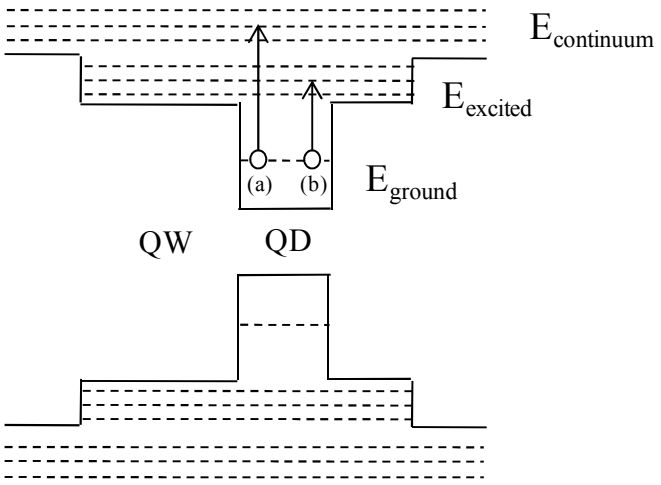

Figure 2.13 – QDIP band diagram showing (a) ground state to continuum and (b) ground state to higher excited energy state transitions

QDIPs have a bias tunable spectral response which leads to the capability of multi-spectral imaging. This therefore also makes them attractive for ratio radiation thermometry. For each polarity, there are two distinct peaks in the spectral response. These spectra are dependent on the transitions between the ground energy state to the continuum level and the higher excited energy states. The shorter wavelength peak is due to transitions between ground and continuum, with the longer wavelength peak (more than one peak is possible if the energy levels are sufficiently separated in the well) due to transitions between the ground and the higher excited energy states. Under applied bias, the energy bands tilt and the transition energies between the ground and the excited state or the continuum level alter. Therefore, different bias voltages lead to different spectra. Figure 2.14 shows the QDIP transitions under (a) forward bias and (b) reverse bias. If the QD inside the QW is off-centre, further transitions and more varied spectral responses exist. The end result is a multi-spectral detector, with different spectra for forward and reverse operating bias voltage.

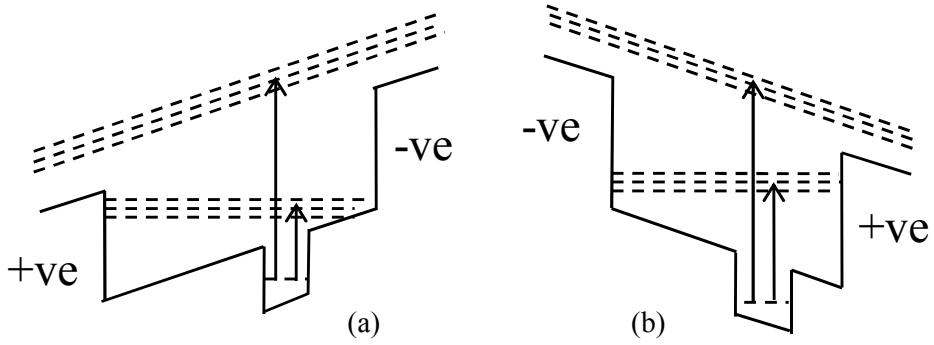

Figure 2.14 – QDIP band diagram under (a) forward and (b) reverse bias

In addition to the photocurrent, dark current processes within QDIPs are triggered by thermal energy. For instance, this thermal energy can elevate the electrons either directly into the continuum level, by thermionic emission, or into the higher excited states. The electrons in the higher excited states can then tunnel through the potential barrier and into the continuum level. Once in the continuum level, these electrons form the dark current.

2.4 Detector figures of merit

Various figures of merit are used when characterising photon detectors. Their theory is discussed in this section.

2.4.1 Dark current

Dark current is the current that flows through a photodetector in the absence of any optical signal. It is a key parameter which relates strongly to the detector's noise. It is composed of several mechanisms common to all photodetectors, whilst some are device specific. In practical radiation thermometers, the dark current creates an offset voltage that needs to be accounted for in calibration when using DD. Ideally, all the dark current should be due to the bu1k semiconductor material, as opposed to surface, or edge, leakage. The major bulk dark current mechanisms are diffusion, $I_{diffusion}$, generation-recombination (g-r), $I_{g\text{-}r}$, and tunnelling, $I_{tunnelling}$, as shown in equation (2.10), equation (2.11) and equation (2.12), respectively.

$$I_{diffusion} = I_o \left[\exp\left(\frac{qV}{k_B T}\right) - 1\right] \tag{2.10}$$

$$I_{g-r} = \frac{q n_i A W}{\tau_{eff}} \tag{2.11}$$

$$I_{tunnelling} = \frac{(2m^*)^{0.5} q^3 E V A}{4\pi^2 \hbar E_g^{0.5}} exp\left[-\frac{\alpha_T (m^*)^{0.5} E_g^{1.5}}{q\hbar E}\right] \tag{2.12}$$

I_o is the saturation current, n_i is the intrinsic carrier concentration, A is the detector active area, W is the depletion region width, τ_{eff} is the effective carrier lifetime, m^* is the electron effective mass, V is the voltage, $\hbar$ is the reduced Planck constant, E_g is the bandgap and α_T is a tunnelling parameter.

Diffusion current involves majority carriers diffusing across the potential barrier of the junction, whilst g-r current arises due to the generation and recombination of

carriers. Tunnelling currents are due to carriers being able to penetrate, or tunnel, through the potential barriers. Depending on the detector quality, the dark current can be highly dependent upon temperature. Therefore, cooling may be required in order to reduce the dark current. The bulk dark current in APDs is diffusion in the absorption layer and g-r and tunnelling in the avalanche region [28] and in T2SLs it is diffusion and g-r [18]. In QDIPs, the dark current is heavily dependent on thermal energy, thermionic emission and tunnelling [29], as discussed in section 2.3.3.

Surface leakage currents are caused by dangling bonds at the surface of the material. In detectors requiring bias voltage, it leads to current flowing along the surface of the material. Optimised bond terminations (a good example of good termination is the SiO_2-Si interface) are required to prevent such dangling bonds from being created and hence reduce the surface leakage current. Unfortunately, termination by a high quality native oxide is not available in most semiconductors. Therefore the bond termination is largely dependent on the use of suitable wet or dry chemical etching and passivation by dielectric materials. An assessment of this leakage current is done by comparing reverse bias dark current density for different sized detectors. Smaller detectors have a greater perimeter to area ratio, and if these detectors show higher dark current density than larger detectors, it is an indication of a surface leakage component. Various surface passivation techniques have been developed in order to reduce the surface leakage current whilst also providing long term protection to the detector's surface to ensure reliability over time [30].

2.4.2 Noise

The noise within a detector dictates the minimum measurable signal. It is composed of several components, but the major components are shot, thermal and 1/f noise, although other noise components exist which are specific to different detectors.

The shot noise, equation (2.13), arises from the current's random fluctuations and is independent of frequency. It is highly dependent upon the dark current, so an increase in this increases the shot noise.

$$i_{n\,shot}^2 = 2qI_d\Delta f \tag{2.13}$$

I_d is the dark current, q is the electron charge, and Δf is the bandwidth of the measurement system.

The thermal noise, equation (2.14), is dependent upon the random thermal motion of carriers in a semiconductor and is also independent of frequency. As temperature increases, so does the thermal noise. R_0 is the resistance of the photodiode, and can be approximated using equation (2.15).

$$i_{n\,thermal}^2 = \frac{4kT\Delta \mathrm{f}}{R_0} \tag{2.14}$$

$$R_0 = \frac{kT}{qI_d} \tag{2.15}$$

Unlike shot and thermal noise, 1/f noise is dependent on frequency, and is dominant at lower frequencies. At higher frequency, it reduces, resulting in the noise being dominated by other mechanisms, as shown in Figure 2.15. The origin of 1/f noise is not well understood, although it is believed to be related to material defects.

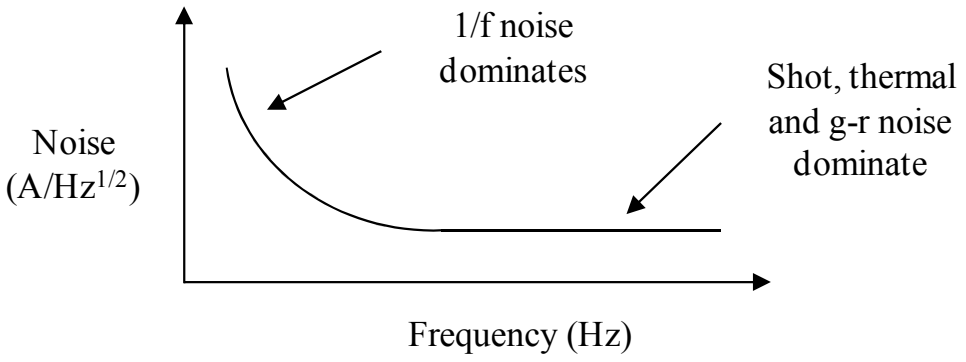

Figure 2.15 – Frequency dependence of noise

In APDs, an additional noise component is the excess avalanche noise due to statistical fluctuations in the gain [31]. This is caused by different lengths of multiplication chain which are initiated by different electron-hole pairs. This results in excess noise, or multiplication noise, that can be characterised by an excess noise factor, ENF. This is used to define the level of the excess noise for a specific APD.

In QDIPs, an additional noise component is g-r noise, equation (2.16). It arises from the random fluctuations associated with the generation and recombination of carriers.

$$i_{n\ g-r}^2 = 4qI_d \mathrm{g}\Delta f \tag{2.16}$$

g is the photoconductive gain, which is essentially the number of collected carriers exiting the detector for each carrier which has been excited. This gain mechanism leads to increased photocurrent in QDIPs.

2.4.3 Responsivity

The responsivity of a photodetector is a relationship between the measured photocurrent and the power incident on the detector's surface.

$$R(\lambda) = \frac{\eta q}{hc} \tag{2.17}$$

$$R_p = \frac{I_p}{\int_{\lambda_1}^{\lambda_2} R(\lambda)P(\lambda)} \tag{2.18}$$

$$P(\lambda) = \mathrm{W}(\lambda).\sin^2\left(\frac{\theta}{2}\right) A.M_F.T_F\,.\cos(\varphi)(1-r) \tag{2.19}$$

The responsivity can be expressed as a function of both wavelength, *R(λ)*, and bias voltage, equations (2.17) and (2.18), respectively. Equation (2.19) shows the power incident per unit wavelength upon the photodiode [5], *P(λ)*, where *r* is the reflectivity of the photodiode material surface. Due to its relation to the photocurrent,

responsivity is affected by the same mechanisms; as photocurrent goes up, so does responsivity. R_p is the peak responsivity of the photodiode and η is the photodiode's quantum efficiency. It can be referred to as either external or internal quantum efficiency. External quantum efficiency is the number of carriers which are created per photon incident on the surface of the detector. Internal quantum efficiency excludes photons reflected from the surface of the detector, and it is defined by the number of carriers created per photon which enter the detector's structure. The theoretical maximum responsivity of a photodetector, assuming no gain, can be calculated using equation (2.20).

$$R_p = \frac{\eta \lambda_{peak}}{1.24} \tag{2.20}$$

The maximum theoretical responsivity is determined by the peak wavelength, λ_{peak}, in μm, of the detector. Therefore, if the responsivity is larger than this, it would indicate the presence of a gain mechanism within the detector. For an APD, this is multiplication gain; for a QDIP, this is photoconductive gain.

The variation of the responsivity as a function of wavelength, *R(λ)*, is known as the spectral response of the photodetector. It is determined by the bandgap of the photodetector band structure.

2.4.4 D*

The D* of a photodetector is essentially a SNR indictor calculated from the responsivity and the noise, and is the most important figure of merit when comparing detectors; it takes into account different detector areas. Using this, a comparison between different detectors can be made based on how well they can distinguish the photocurrent from the noise level.

$$D^* = \frac{R_p \sqrt{A\Delta f}}{i_{n\,total}} \tag{2.21}$$

The peak value of D* is found using equation (2.21), where $i_{n\ total}$ is the total noise. The noise used in this calculation should be measured noise, when possible, or calculated noise based on shot and thermal noise when measurement is not possible, such as when the noise is out of the equipment measurement range. Different levels of D* are sufficient for different applications, but the higher the value of D*, the better the detector will be at distinguishing the signal from the noise. D* is generally larger for shorter wavelength photodetectors due to reduced dark current and therefore reduced noise.

2.4.5 Noise equivalent power

The noise equivalent power (NEP) of a photodetector is the radiant power which is incident upon the detector's surface which results in a signal equal to the root mean square of the detector noise. Therefore, it accounts for both the detector's signal and noise. It is a measure of the detector's sensitivity, and as low a value of NEP as possible is desired. It is an important parameter for radiation thermometry, as it gives an indication of the amount of averaging time required in order to measure the temperature. A longer averaging time leads to an improvement in the SNR of the measurement. However, the use of a more sensitive detector may allow for measurement of the temperature with the same SNR but over a shorter period of time. This will therefore lead to higher speed radiation thermometry measurements.

2.5 IRAS theory

The IRAS approach for ratio radiation thermometry, and how it can be related to physical measurements, is discussed in this section. As discussed in section 2.2.3, ratio radiation thermometers rely on the measurement of the ratio between photocurrents produced from detectors operating over two separate wavelength bands. As an example of the ratio principle, Figure 2.16 shows a bandpass filter placed between a blackbody source and a power meter.

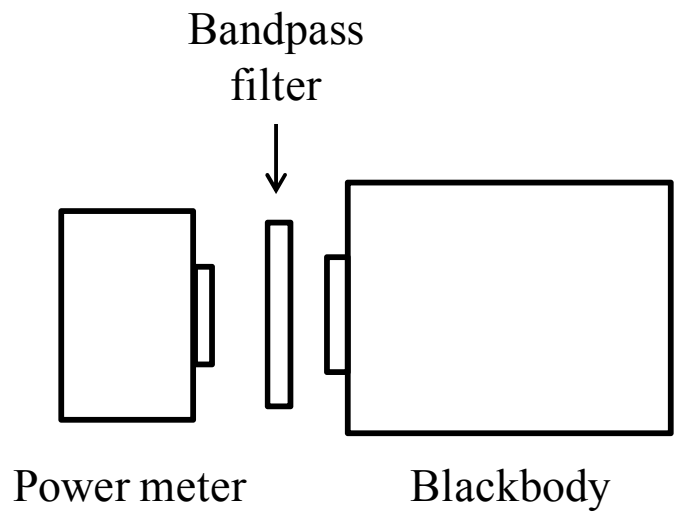

Figure 2.16 – Blackbody power transmitted through bandpass filter

The power meter measures the power emitted from the blackbody which is transmitted through the filter. This can be repeated with a second bandpass filter with a different transmission wavelength. This analysis uses filters with transmission wavelengths of 3.17–5.0 and 5.0–7.0 μm, which will be known as the shorter wavelength filter (SWF) and the longer wavelength filter (LWF), respectively. A ratio between the powers measured through each filter is calculated by dividing the power transmitted through the SWF by the power transmitted though the LWF. From this ratio, T_{BB} can be inferred. Figure 2.17(a) shows the transmission of the SWF and LWF, with Figure 2.17(b) showing the power measured by the power meter for the SWF and LWF. Figure 2.17(c) shows the SWF/LWF power ratio as a function of T_{BB}, for T_{BB} = 100-800 ^{o}C.

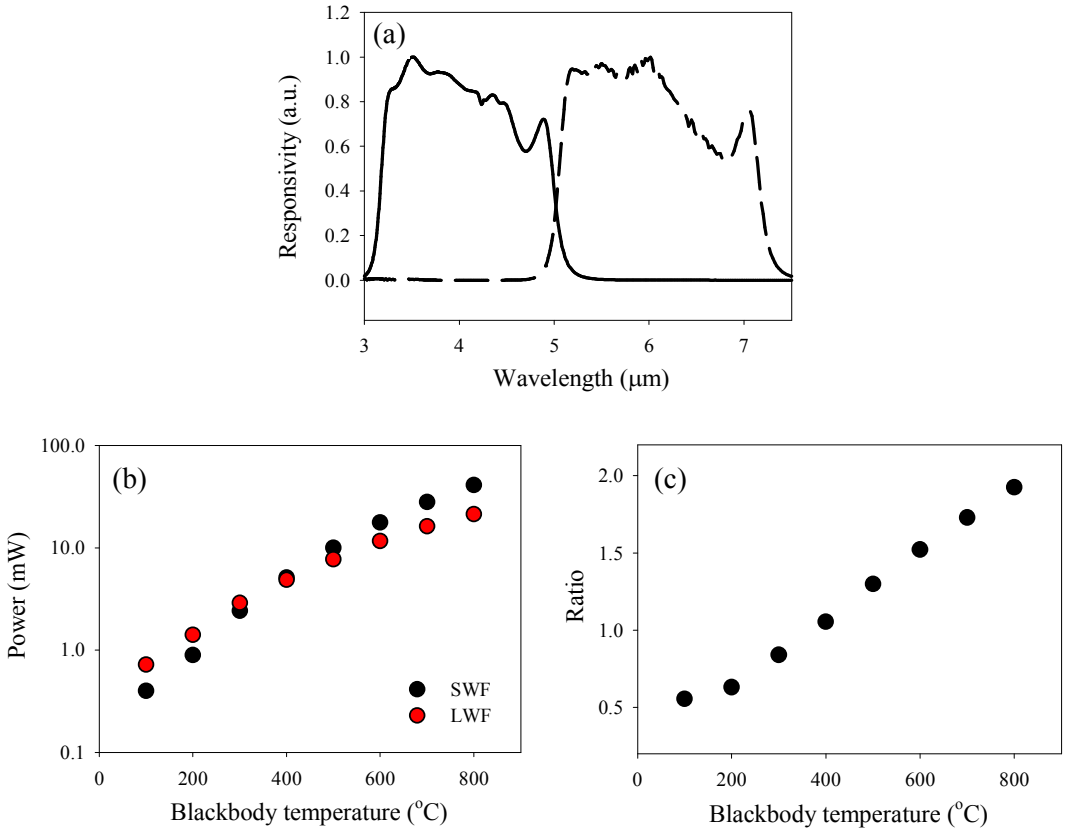

Figure 2.17 – (a) Filter transmission for SWF and LWF, (b) power measured by a power meter for SWF and LWF and (c) SWF/LWF power ratio as a function of T_{BB}

For T_{BB} = 800 °C, the ratio between the filters was calculated to be 1.89. As T_{BB} reduces, so does this ratio, due to the shift in the blackbody power to longer wavelengths. As T_{BB} drops below 200 °C, the ratio appears to deviate from its trend. This is believed to be due to the power meter's inability to measure this lower power with sufficient accuracy, resulting in this error. Once this point is reached, the measured power is below 2 mW for each filter. The IRAS can be demonstrated in a similar fashion to work as a ratio radiation thermometer. The filters, given by arbitrary spectral shapes, are defined within the IRAS rather than during the measurement.

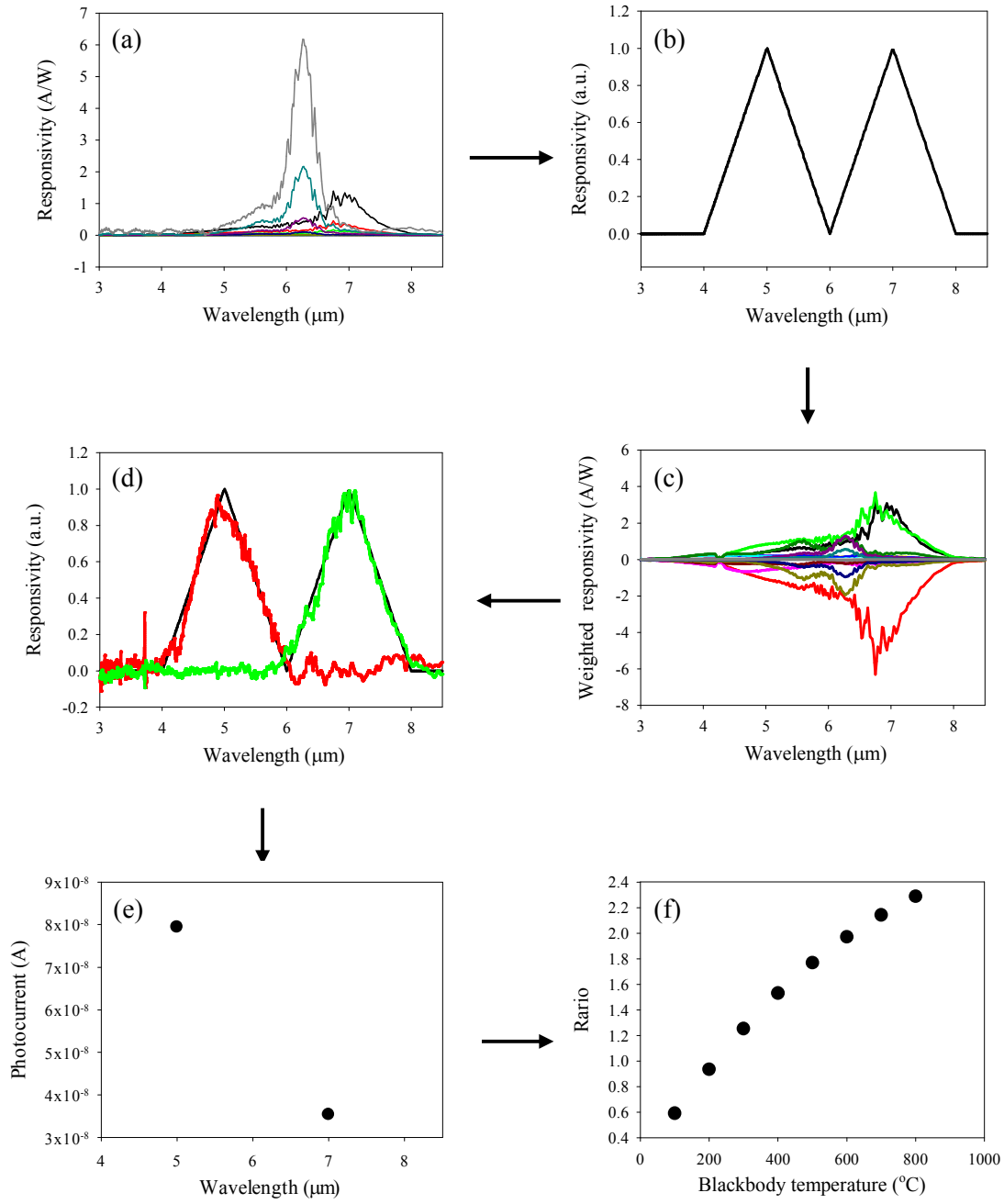

Figure 2.18 – IRAS process. (a) Bias dependent responsivities with wavelength are measured using photocurrent produced at each T_{BB}. (b) Arbitrary spectral shapes to be reproduced are defined. (c) Weighted responsivity from QDIP response calculated by the QDIP responses by weighting factors associated with each response. (d) Summation of weighted QDIP responses allows for spectral shapes to be reproduced. (e) Photocurrent calculated from filters and Planck's Law. (f) Ratios computed between calculated photocurrents at each T_{BB} using the IRAS.

The basic principle of the IRAS is a summation of weighted spectral responses at a given number of bias voltages for a QDIP in order to reproduce a spectral shape. This spectral shape could be that of real filter spectra, or of arbitrary filters such as rectangular or triangular shapes [29]. This essentially allows approximated narrowband responses to be formed from wideband responses from the QDIP. By combining these filters with Planck's Law, photocurrents corresponding to each filter can be calculated. By dividing one photocurrent by the other, a ratio relating to T_{BB} can be produced. Figure 2.18 outlines the process of the IRAS.

Weighting factors are calculated, with each corresponding to the spectral response at specific bias voltages. These weighting factors are used by the IRAS to reproduce the filters. Equations (2.22), (2.23) and (2.24) are used to calculate the weighting factors.

$$\boldsymbol{w} = (\boldsymbol{A}^T\boldsymbol{A} + \boldsymbol{\Phi})^{-1}\boldsymbol{A}^T\boldsymbol{R} \tag{2.22}$$

where

$$\boldsymbol{A} = \begin{bmatrix} R_{V1}(\lambda_1) & R_{V2}(\lambda_1) & \cdots & R_{VN}(\lambda_1) \\ R_{V1}(\lambda_2) & R_{V2}(\lambda_2) & \cdots & R_{VN}(\lambda_2) \\ \vdots & \vdots & \vdots & \vdots \\ R_1(\lambda_L) & R_2(\lambda_L) & \cdots & R_{VN}(\lambda_L) \end{bmatrix} \tag{2.23}$$

and

$$\boldsymbol{R} = \begin{bmatrix} R(\lambda_1) \\ R(\lambda_2) \\ \vdots \\ R(\lambda_L) \end{bmatrix} \tag{2.24}$$

$\boldsymbol{w}$ is the weighting factor vector which corresponds to the bias dependent weighting factors. For N bias voltages, there are weights of $w_1, w_2, \ldots, w_N$. $\boldsymbol{A}$ is a matrix formed of the QDIP responsivities as a function of wavelength and bias voltage, and $\boldsymbol{R}$ is the

arbitrary spectral shape as a function of wavelength. A SNR term, $\boldsymbol{\Phi}$, can be used in the IRAS, but for an ideal noiseless system, it is taken as a null matrix.

The calculated weights, *w*, at each bias voltage are multiplied by the measured responsivity, *R*, at the corresponding bias voltage to give the weighted responsivity as a function of wavelength at each bias voltage. These weighted responsivities are summed together to produce the calculated reproduction of the filters, $\boldsymbol{R_{rep}}$, as shown by equation (2.25).

$$\boldsymbol{R_{rep}} = \sum_{i=1}^{N} w_{V_i} R_{V_i,} \tag{2.25}$$

Photocurrents, $I_{ph,}$ corresponding to each filter can be calculated using equation (2.2). It is an integration of the product between the responsivity as a function of wavelength of the reproduced filter and the power calculated upon the QDIP surface as defined by Planck's Law.

Finally, a ratio between the photocurrents from each filter is calculated, as defined by equation (2.26).

$$Ratio = \frac{I_{ph}(SWF)}{I_{ph}(LWF)} \tag{2.26}$$

It should be noted that the IRAS does not account for the noise in the responsivity measurement, nor is the number of bias voltages used optimised. These aspects need to be developed further for future implementation of the IRAS for ratio radiation thermometry.

References

[1] T. J. Quinn, *Temperature*, 2nd ed. London, UK: Academic Press Limited, 1990.

[2] P. Saunders, *Radiation Thermometry: Fundamentals and Applications in the Petrochemical Industry* vol. 78: SPIE press, 2007.

[3] J. Nicholas, D. R. White, and J. Wiley, *Traceable temperatures: an introduction to temperature measurement and calibration*: Wiley New York, 2001.

[4] Hamamatsu Photonics, *Si Photodiodes - S2386 series*. Available: http://www.hamamatsu.com/resources/pdf/ssd/s2386_series_kspd1035e06.pdf, (2013).

[5] S. D. Gunapala and S. V. Bandara, "Quantum well infrared photodetector (QWIP) focal plane arrays," *Semiconductors and Semimetals,* vol. 62, pp. 197-282, 1999.

[6] J. Taylor. (2008). *Infrared Training Notes - Level 1*. Available: http://www.aumico.it/prodotti/files/117.pdf

[7] K. Boboridis, "Application of single-wavelength radiation thermometry and high-speed laser polarimetry to thermophysical property measurements on pulse-heated metals," *Graz University of Technology, Graz, Austria,* 2001.

[8] J. Bezemer, "Spectral sensitivity corrections for optical standard pyrometers," *Metrologia,* vol. 10, pp. 47-52, 1973.

[9] J. W. Hahn and C. Rhee, "Interpolation Equation for the Calibration of Infrared Pyrometers," *Metrologia,* vol. 31, pp. 27-32, 1994.

[10] P. Saunders, "Uncertainty Arising from the Use of the Mean Effective Wavelength in Realizing ITS-90," *AIP Conference Proceedings,* vol. 684, 2003, pp. 639-644.

[11] J. Dixon, "Radiation thermometry," *Journal of Physics E: Scientific Instruments,* vol. 21, pp. 425-436, 1988.

[12] C.-D. Wen and I. Mudawar, "Emissivity characteristics of polished aluminium alloy surfaces and assessment of multispectral radiation thermometry (MRT) emissivity models," *International journal of heat and mass transfer,* vol. 48, pp. 1316-1329, 2005.

[13] X. He, Y. Li, L. Wang, Y. Sun, and S. Zhang, "High emissivity coatings for high temperature application: progress and prospect," *Thin Solid Films,* vol. 517, pp. 5120-5129, 2009.

[14] J. Fischer, M. Battuello, M. Sadli, M. Ballico, S. N. Park, P. Saunders, *et al.*, "Uncertainty budgets for realization of ITS-90 by radiation thermometry," in *AIP Conference Proceedings*, Chicago, Illinois, USA, 2003, pp. 631-638.

[15] J. C. Campbell, S. Demiguel, F. Ma, A. Beck, X. Guo, S. Wang, *et al.*, "Recent advances in avalanche photodiodes," *IEEE Journal of Selected Topics in Quantum Electronics,* vol. 10, pp. 777-787, 2004.

[16] I. Wegrzecka, M. Wegrzecki, M. Grynglas, J. Bar, A. Uszynski, R. Grodecki, *et al.*, "Design and properties of silicon avalanche photodiodes," *Opto-Electronics Review,* vol. 12, pp. 95-104, 2004.

[17] R.J. McIntyre, "Recent developments in silicon avalanche photodiodes," *Measurement,* vol. 3, pp. 146-152, 1985.

[18] E. Plis, J. B. Rodriguez, and S. Krishna, "6.06 - InAs/(In)GaSb Type II Strained Layer Superlattice Detectors," in *Comprehensive Semiconductor Science and Technology*. vol. 6, P. Bhattacharya, R. Fornari, and H. Kamimura, Eds., ed Amsterdam: Elsevier, 2011, pp. 229-264

[19] A. Rogalski, "New material systems for third generation infrared photodetectors," *Opto-Electronics Review,* vol. 16, pp. 458-482, 2008.

[20] M. Razeghi, S. A. Pour, E. Huang, G. Chen, A. Haddadi, and B. Nguyen, "Type-II InAs/GaSb photodiodes and focal plane arrays aimed at high operating temperatures," *Opto-Electronics Review,* vol. 19, pp. 261-269, 2011.

[21] A. V. Barve, S. J. Lee, S. K. Noh, and S. Krishna, "Review of current progress in quantum dot infrared photodetectors," *Laser & Photonics Reviews,* vol. 4, pp. 738-750, 2010.

[22] G.-j. Zhang, Y.-c. Shu, J.-h. Yao, Q. Shu, H.-l. Deng, G.-z. Jia, *et al.*, "Characteristics and developments of quantum-dot infrared photodetectors," *Frontiers of Physics in China,* vol. 1, pp. 334-338, 2006.

[23] D. Symons, M. Lakrimi, M. Van der Burgt, T. Vaughan, R. Nicholas, N. Mason, *et al.*, "Temperature dependence of the band overlap in InAs/GaSb structures," *Physical Review B,* vol. 51, p. 1729, 1995.

[24] E. A. Plis, "Mid-IR type-II InAs/GaSb nanoscale superlattice sensors," Dissertation, The University of New Mexico, Albuquerque, New Mexico, USA, 2007.

[25] B. Streetman and S. Banerjee, *Solid State Electronic Devices*, 5 ed. vol. 1. Upper Saddle River, New Jersey: Prentice Hall, 2000.

[26] H. Haugan, S. Elhamri, F. Szmulowicz, B. Ullrich, G. Brown, and W. Mitchel, "Study of residual background carriers in midinfrared InAs⁄ GaSb superlattices for uncooled detector operation," *Applied Physics Letters,* vol. 92, p. 071102, 2008.

[27] H. Martijn, C. Asplund, R. M. von Würtemberg, and H. Malm, "High-performance MWIR type-II superlattice detectors," in *SPIE Defense, Security, and Sensing*, p. 87040Z, 2013.

[28] R. Fyath and J. J. O'Reilly, "Performance degradation of APD-optical receivers due to dark current generated within the multiplication region," *Journal of Lightwave Technology,* vol. 7, pp. 62-67, 1989.

[29] P. Vines, "Infrared Detection and Spectral Imaging Using Low Strain Quantum Dot Infrared Photodetectors," Dissertation, Department of Electronic and Electrical Engineering, University of Sheffield, Sheffield, 2010.

[30] P.-Y. Delaunay, A. Hood, B. M. Nguyen, D. Hoffman, Y. Wei, and M. Razeghi, "Passivation of type-II InAs⁄ GaSb double heterostructure," *Applied Physics Letters,* vol. 91, p. 091112, 2007.

[31] R. J. McIntyre, "Multiplication noise in uniform avalanche diodes," *IEEE Transactions on Electron Devices,* vol. 13, pp. 164-168, 1966.

Chapter 3 – Experimental details

3.1 Introduction

This chapter describes the experimental setups and procedures used to evaluate the performance of the detector technologies. Electrical and optical characterisation techniques were employed to determine various figures of merit for the detectors discussed in Chapter 2. In addition, the description of a transimpedance amplifier (TIA) circuit and phase sensitive detection (PSD) used during radiation thermometry measurements are presented and discussed.

3.2 Dark current and capacitance

Dark current measurements are indispensible for screening the quality of the detector, whilst capacitance measurements can be used to extract depletion width and doping profile with voltage.

3.2.1 Dark current measurements

Equation (3.1) shows the ideal diode equation, where I_F is the forward current, V_B is the built in voltage and n is an ideality factor which varies between 1 and 2.

$$I_F = I_o \left[\exp\left(\frac{qV_B}{nk_BT}\right) - 1\right] \tag{3.1}$$

Determination of n allows assessment of the type of current dominating in the detector. If n is closer to 1, this suggests that diffusion dominates; if n is closer to 2, it suggests that g-r dominates (for instance due to the presence of defects within the material and possible growth issues). A high quality diode exhibits n that is close to unity.

$$\ln(I_F) = \ln(I_0) + \left(\frac{q}{nk_BT}\right)V_B \tag{3.2}$$

n can be determined by measuring the forward dark current using a rearrangement of the diode equation, equation (3.2). This is then plotted, with *n* calculated from the gradient of the graph. Figure 3.1 shows how different gradients represent different values of n.

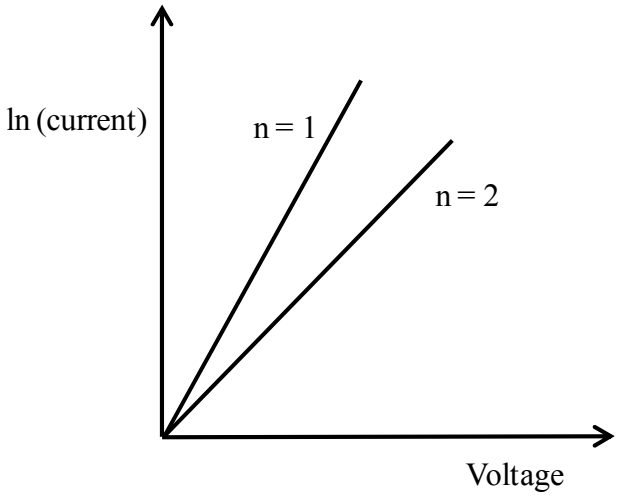

Figure 3.1 – n calculated from forward dark current measurements

To obtain an accurate estimation of the reverse saturation current, current-voltage (IV) measurements are normally performed in the dark to remove the influence of light. A low value of saturation current, I_o, is desirable in order to minimise the dark current which flows through the diode and therefore minimise the noise.

The bulk and surface leakage current components are assessed by evaluating the reverse bias current, I_d. Equations (3.3) and (3.4) show how current over area, or current density, *J*, and current over perimeter, *I / Perimeter*, can be calculated.

$$J = \frac{I_d}{A} \tag{3.3}$$

$$I/Perimeter = \frac{I_d}{Perimeter} \tag{3.4}$$

Measurements and calculations are performed on detectors of varying area and perimeter. If the current density plots overlap with each other, it is an indication that bulk current dominates. However, if I_d scales with perimeter, it indicates that surface leakage current dominates. For bulk dark current, temperature dependence data can be used to analyse the contribution of diffusion and g-r currents.

3.2.2 Capacitance-voltage measurements

CV measurements involve applying a reverse bias voltage to the photodiode, with a superimposed small sinusoidal voltage. In this work, a 50 mV alternating current (AC) signal at a frequency of 400 kHz was used. An inductance-capacitance-resistance (LCR) HP 4275A meter calculates the capacitance of the diode junction from the measured impedance with respect to bias voltage. Increased bias voltage decreases the capacitance due to increasing the depletion region. Equations (3.5) and (3.6) show how the depletion region width (for an abrupt p-n junction), and the effective carrier concentration, N_a, can be extracted.

$$W = \frac{\varepsilon_r \varepsilon_0 A}{C} \tag{3.5}$$

$$N_a = -\frac{2}{q\varepsilon_r \varepsilon_0} \cdot \frac{1}{d(1/C^2)/dV_R)} \tag{3.6}$$

C is the capacitance, ε_r is the relative permittivity of the dielectric, ε_0 is the permittivity of free space and V_R is the direct current (DC) reverse bias voltage.

3.2.3 Measurement setups for IV and CV measurements

A Keithley 236 source measurement unit (SMU) was used for IV measurements while a HP 4275A Multi frequency LCR meter was used for CV measurements. All measurements were controlled by a Labview program. For detectors on-wafer, room temperature measurements were carried out on a conventional probe station, while low temperature measurements were performed using a liquid nitrogen cooled Janis

wafer probe station, illustrated in Figure 3.2. The on-wafer detectors were placed on a metal chuck, which was enclosed by a cold shield. An optical window at the top of the chamber allowed viewing using a camera. The cryostat chamber was pumped down to low pressure before cooling, with the temperature of the metal chuck monitored by a manufacturer calibrated forward biased Si diode and a Scientific Instruments model 9700 temperature controller. The temperature controller also incorporated a heater to set the temperature for the measurement, with the temperature dependent voltage across the Si diode corresponding to the temperature of the setup. To ensure the setup's temperature was stable over different days, the dark current of known reference diode samples was also measured to confirm measurements were consistent. Also, dark currents of the on-wafer detectors were compared with packaged detectors using the setup described in section 3.2.5 for further confirmation of the temperature of both setups. Measurements on-wafer could be performed down to a temperature of 77 K.

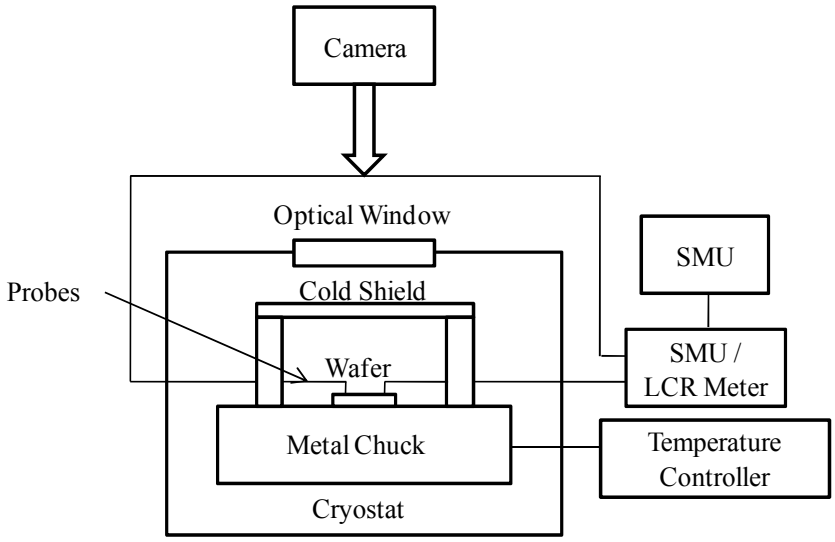

Figure 3.2 – Setup for on-wafer temperature dependent IV and CV measurements

3.2.4 PSD

PSD is used to measure photocurrent independent of the influence of dark current and system noise. PSD allows a signal to be recovered even when it is below the noise floor [1]. The signal is recovered with the use of a heterodyne technique which

shifts the signal away from the noise and subsequently recovers the signal with an appropriate bandwidth filter. This allows for the signal to be measured independently of the noise.

The basic principle of PSD is to use a fixed frequency and phase reference from an optical chopper. The measured and reference signals are given by equation (3.7) and equation (3.8), respectively.

$$V_M \sin(\omega_M t + \theta_M) \tag{3.7}$$

$$V_{REF} \sin(\omega_{REF} t + \theta_{REF}) \tag{3.8}$$

V_M and V_{REF} are the amplitudes, ω_M and ω_{REF} are the frequencies and θ_M and θ_{REF} are the phase, each for the measured and reference signals, respectively. Time is denoted by t. The product of equation (3.7) and equation (3.8), given by equation (3.9), gives the output of the PSD technique, V_{PSD} [2].

$$\begin{aligned} V_{PSD} &= V_M V_{REF} \sin(\omega_M t + \theta_M) \sin(\omega_{REF} t + \theta_{REF}) \\ &= \frac{1}{2} V_M V_{REF} [\cos(\omega_M t - \omega_{REF} t + \theta_M - \theta_{REF}) - \cos(\omega_M t \\ &\qquad + \omega_{REF} t + \theta_M + \theta_{REF})] \end{aligned} \tag{3.9}$$

The PSD output subsequently passes through a low pass filter, leading to the removal of the AC signals. If $\omega_M = \omega_{REF}$, the output simply becomes a DC term. This therefore provides a DC signal which can be related to the signal amplitude, as shown by equation (3.10).

$$V_{PSD} = \frac{1}{2} V_M V_{REF} \cos(\theta_M - \theta_{REF}) \tag{3.10}$$

3.2.5 Measurement setup for responsivity, noise and spectral response measurements

The optical window of the Janis probe station does not transmit wavelengths above 5 μm. In addition there are difficulties associated with focusing the blackbody radiation onto the device which is located at 60 cm from the optical window. Therefore a different setup is required for responsivity and spectral response measurements at IR wavelengths. Figure 3.3 shows this second cryostat setup, where the detectors were packaged onto transistor outline (TO) style TO-5 headers and placed in contact with a cold finger inside a helium cooled cryostat. This cryostat, with a KBr window that allows transmission wavelengths of 0.25 - 25 μm, was controlled by a CTI Cryogenics 8300 compressor and 8100 controller. This setup allowed the detectors to be cooled down to 30 K, with the temperature controlled by a Lakeshore 332 temperature controller. The temperature of the detector and the cold finger was monitored by manufacturer calibrated Lakeshore Si diodes, model number DT-471-CU, which function as the diode described in section 3.2.3. To confirm the setup temperature was consistent across different days, the measurements were performed on different samples. BNC connectors on the cryostat allowed for a connection between the detector and measurement equipment to take place.

A thermally conducting (but electrically insulating) printed circuit board, placed between the detector and the cold finger, is essential for noise measurements in order to ensure that the detector is electrically isolated from the cold finger. Noise measurements were performed by amplifying the signal using a Stanford Research Systems SR570 low noise pre-amplifier, and extracting the noise using a Stanford Research System SR760 spectrum analyser. The biasing of the detectors was achieved by use of the internal biasing of the pre-amplifier, with bias voltages greater than ±5 V achieved by placing 9 V batteries in series with the pre-amplifier.

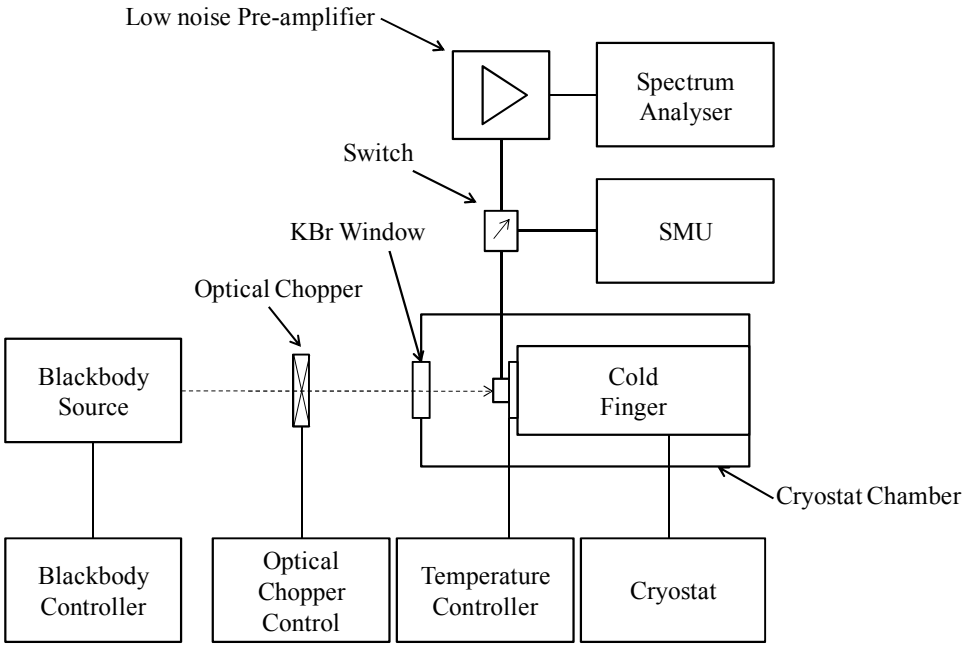

Figure 3.3 – Setup for noise and responsivity measurements

Responsivity and photocurrent measurements were carried out using an Infrared Systems model IR-563/301 blackbody (controlled by an Infrared Systems IR-301 blackbody controller) as the IR source. To isolate the influence of the dark current, PSD was performed using an optical chopper at a frequency of 810 Hz.

For spectral response measurements, a parabolic mirror was used to focus the output from a Varian 7000 Fourier Transform Infra-Red (FTIR) Spectrometer onto the detector as shown in Figure 3.4. The output from the pre-amplifier was connected to the FTIR.

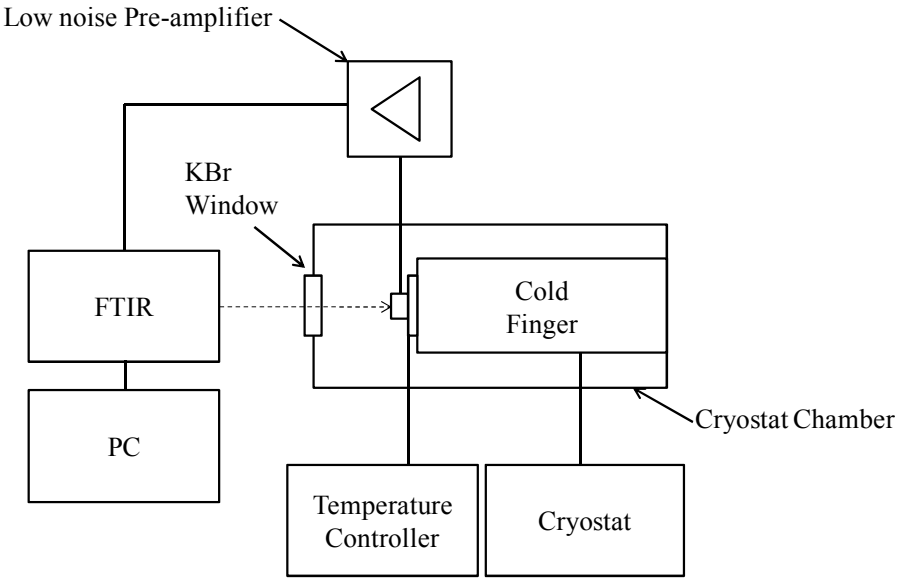

Figure 3.4 – Setup for spectral response measurements

In this work, the spectral response is represented in three ways. Firstly, the raw output from the pre-amplifier gives the spectral intensity, which can be used to assess how the photodiode's bias voltage and temperature photocurrent varies with wavelength. Secondly, by dividing the spectral intensity at each wavelength by its peak value, a normalised spectral response can be produced, therefore enabling a clear assessment detector's wavelength dependence. Finally, the normalised spectral response can be multiplied by the peak responsivity to give the responsivity as a function of wavelength.

Further details on how the cryostat used in these measurements is controlled, as well as how the photocurrent, noise and spectral response measurements are performed, can be found in Appendices C, D, E and F, respectively.

3.3 Radiation thermometry setup design and operation

3.3.1 TIA theory and operation

The basic principle of a TIA circuit is to convert current, in this case photocurrent, into a voltage. This voltage can then be measured at the thermometer output using a lock-in amplifier or an SMU, depending on whether PSD or DD was used. Further details regards TIA operation, derivation and theory can be found elsewhere [3][4], but a basic description of its operation will be described here. Figure 3.5 shows the basic circuit topology for a two-stage TIA, with Appendix G showing the full circuit with component values used.

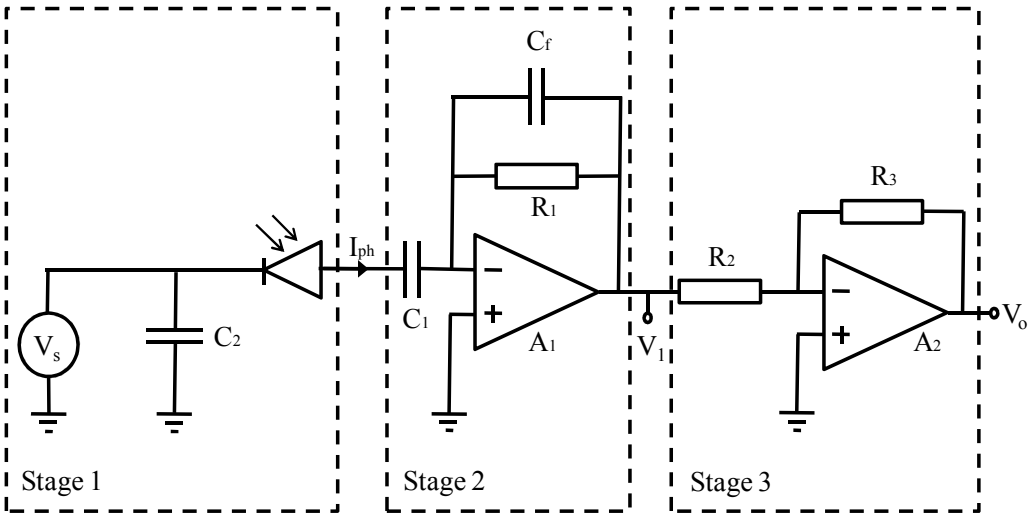

Figure 3.5 – TIA circuit topology

The circuit can be split into three stages. Stage 1 governs the biasing of the detector; stage 2 is the TIA which converts the photocurrent to a voltage; and stage 3 which provides further amplification of the voltage. Note only the Si APD is biased using stage 1; the Si photodiode operates at 0 V and is instead connected to ground. The operational amplifiers used in the circuit are Texas Instruments model OPA637.

In stage 1, the detector is biased by V_S, which represents an SMU. C_2 acts as a decoupling capacitor to the SMU, providing a route to ground for the high frequency

noise. The photocurrent, I_{ph}, produced by the photodiode, enters stage 2 and is amplified by the TIA to produce a voltage. R_1 defines the gain of the first amplifier stage, with C_f acting as a damping capacitor to reduce the frequency response gain peaking. C_1 acts as a DC blocking capacitor for PSD measurements, but is replaced by a short circuit for DD measurements. The transfer function, relating I_{ph} to the output voltage of the stage, V_1, is given by equation (3.11).

$$V_1 = -\frac{sR_1C_1}{1 + sR_1C_f}.I_{ph} \tag{3.11}$$

This can be rewritten as shown in equation (3.12), where ω is the frequency, and ω_1 and ω_f define the lower and upper -3 dB points, respectively. These points are given by $\omega_1 = (1/R_1C_1)$ and $\omega_f = (1/R_1C_f)$. The square root of -1 is denoted by j.

$$V_1 = -\frac{j\frac{\omega}{\omega_1}}{1 + j\frac{\omega}{\omega_f}}.I_{ph} \tag{3.12}$$

Figure 3.6 shows the bandwidth for stage 2 of the TIA circuit.

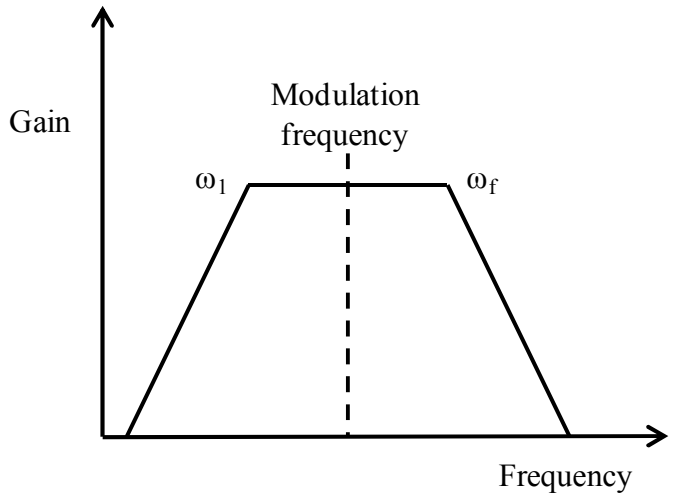

Figure 3.6 – Bandwidth for stage 2 of TIA circuit

When using PSD, and whilst designing the circuit, the modulation frequency of the photodiode needs to lie within the flat part of the frequency response to ensure

maximum gain. The high pass filter, defined by the lower frequency cut-off, is required to ensure that the DC dark current is blocked and does not propagate through the circuit. The higher cut-off frequency response is defined by the amplifier gain.

Stage 3 of the circuit is an additional voltage amplifier stage, and the relationship between the final output voltage of the circuit, V_o, and V_1, is given by equation (3.13).

$$V_o = -\frac{R_3}{R_2}.V_1 \tag{3.13}$$

Therefore, the final transfer function relating I_{ph} to V_o is given by equation (3.14).

$$V_o = \frac{sR_1C_2}{1 + sR_1C_f}.\frac{R_3}{R_2}.I_{ph} \tag{3.14}$$

The use of two gain stages is required to maintain a bandwidth >> modulation frequency of the measurements, whilst ensuring a sufficient level of gain. The total gain of 1×10^6 V/A is achieved with first and second stage gains of 1×10^4 and 1×10^2 V/A, respectively.

Basic characterisation was performed on the TIA circuit in terms of gain, bandwidth and noise. Figure 3.7 shows a bode plot[a] for the TIA circuit showing the first and second stage gains, as well as the total gain of the amplifier.

[a] A graph which shows the frequency response of the magnitude or phase of a transfer function

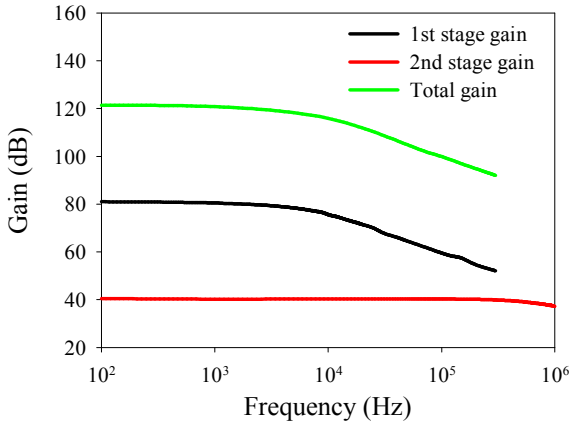

Figure 3.7 – Bode plot for TIA circuit

The total gain of the amplifier was found to be 120 dB, corresponding to the desired gain of 1×10^6 V/A. The -3 dB cut-off frequency of the amplifier was measured at 8 kHz. This indicates that the amplifier's bandwidth is suitable for use with the optical chopper as long as the modulation frequency is within this range.

Using a spectrum analyser, the noise at the amplifier output was found to be 125 $nV/Hz^{1/2}$, which is comparable with commercial amplifiers. The gain, bandwidth and noise of the TIA deem the amplifier to be suitable for performing radiation thermometry measurements.

3.3.2 Fixed gain room temperature radiation thermometry setup

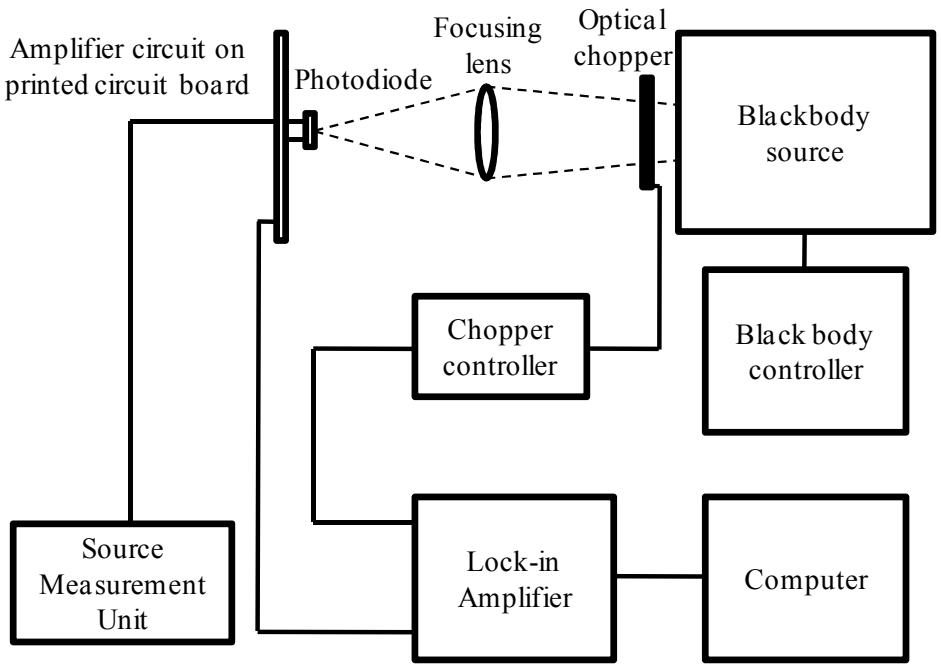

Figure 3.8 – Setup for fixed gain room temperature PSD radiation thermometry measurements

Figure 3.8 shows the setup used in Chapter 4 for room temperature PSD radiation thermometry measurements using a Si photodiode and a Si APD. The blackbody signal, chopped by an optical chopper at 410 Hz, is focused upon the detector with the use of a focusing lens. This lens was positioned 175 mm from the blackbody source, and 125 mm from the detector. The lens had a diameter of 32 mm, and was an achromatic doublet with a crown element of SK10 and a flint element of SF11. It was positioned at a height of 210 mm above the optical bench, level with the centre of the blackbody aperture. The photocurrent was amplified using a two-stage TIA, with a gain of 1×10^6 V/A. The output voltage was measured using a Stanford Research SR810 lock-in amplifier, monitored over time using a Labview program. The Infrared Systems model IR-563/301 blackbody source, which has a stability of ±0.1 ^{o}C, was used as the blackbody for these measurements. The temperature range used for this blackbody source was from 275 to 600 ^{o}C. The entire setup was enclosed within black optical curtains within a dark room to minimise the influence of background radiation.

For DD measurements, the chopper was removed and the output voltage was measured using a second SMU. The background signal was measured (by blocking the radiation from the blackbody source) and subtracted from the overall signal measured to provide the reading corresponding to the T_{BB}.

3.3.3 Radiation thermometry setup for cooled detector

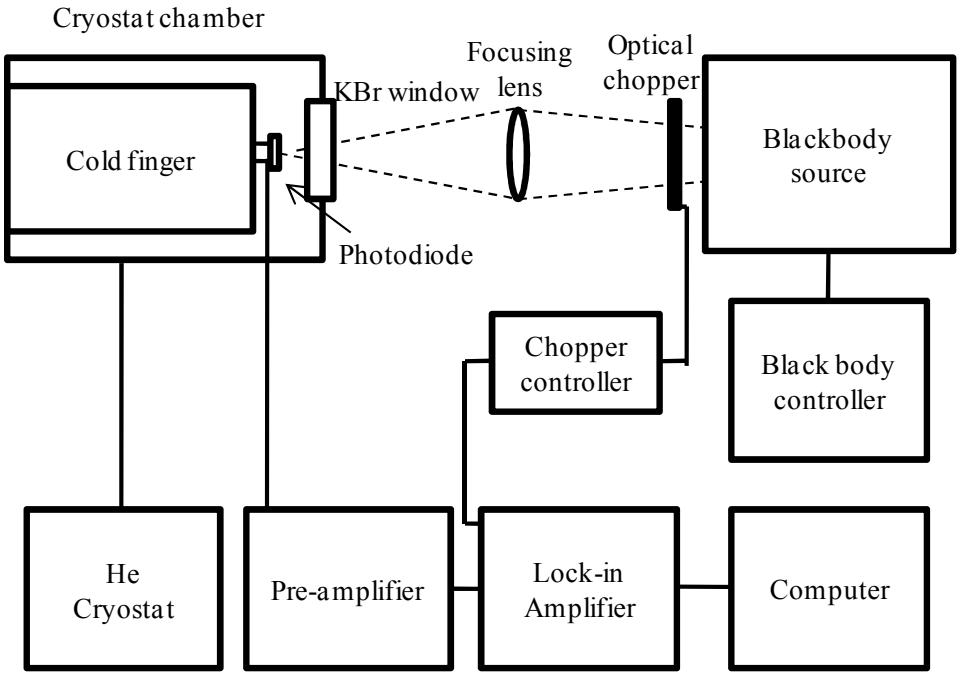

Figure 3.9 – Setup for radiation thermometry with cooled detector

Figure 3.9 shows the radiation thermometry setup used in Chapter 5 for cooled detector measurements using a T2SL. Again the blackbody signal, chopped at 810 Hz, was focused onto the detector using a focusing lens, but this time a CaF_2 lens of diameter 25 mm was used. This lens is used due to its longer wavelength transmission corresponding to the longer wavelength response of the T2SL. It was positioned 35 mm from the detector surface and 265 mm from the centre of the blackbody aperture. A Land Instruments Landcal P80P blackbody radiation source was used as the blackbody source for these measurements at temperatures from 25 to 100 ^{o}C. The stability of this blackbody source was ±0.1 ^{o}C.

Both this measurement setup, and the one described in section 3.3.2, required optimal lens focusing. To ensure this, several precautions were taken. Firstly, the detector was placed 300 mm away from the black body source in line with the centre of its aperture. The output voltage from the amplifier was measured on the lock-in amplifier with the blackbody source set to a reference temperature, for example T_{BB} = 600 ^{o}C for the Si photodiode. Secondly, the focusing lens was placed in a direct line between the detector and the blackbody on a linear optical rail. To ensure the detector, focusing lens and blackbody aperture were in line, the position of the detector and focusing lens were adjusted vertically and horizontally using linear translation stages until the output voltage on the lock-in amplifier was maximised. In additional, the position of the focusing lens between the blackbody aperture and detector was adjusted along the optical rail (the optimum positions found for each setup was as stated in the setup descriptions). Adjustments to the alignment were repeated until the output voltage could not be improved upon any more, with the output voltages for these optimised alignments recorded as reference points. Therefore, comparison of the setups could be made on separate days against these references to ensure the measurements were repeatable.

Further information on how these radiation thermometry measurements were performed can be found in Appendix H.

References

[1] D. P. Blair and P. H. Sydenham, "Phase sensitive detection as a means to recover signals buried in noise," *Journal of Physics E: Scientific Instruments,* vol. 8, pp. 621-627, 1975.

[2] Stanford Research Systems. (2005). *Model SR810 DSP Lock-in Amplifier*. Available: http://www.thinksrs.com/downloads/PDFs/Manuals/SR810m.pdf

[3] G. Rieke, *Detection of Light: From the Ultraviolet to the Submillimeter*, 2nd ed. Cambridge, UK: Cambridge University Press, 2003.

[4] J. Graeme, *Photodiode Amplifiers: Op Amp Solutions*, 1st ed. Boston, MA, USA: McGraw-Hill, 1996.

Chapter 4 – Si avalanche photodiode and phase sensitive detection for radiation thermometry

4.1 Introduction

This chapter evaluates the use of a Si avalanche photodiode (APD) for radiation thermometry in comparison with a Si photodiode. It starts by evaluating phase sensitive detection (PSD) and direct detection (DD) methods for a Si photodiode, including comparison with the modelled results. The more sensitive Si APD is then introduced as an alternative detector, with demonstration of both PSD and DD. The benefits of the Si APD's high internal gain are presented, with discussion on its impact for radiation thermometry. The benefits provided by using the Si APD-PSD combination are discussed [1], as well as the use of either approach individually.

4.2 PSD for radiation thermometry with Si photodiode

4.2.1 Mean output voltage for PSD and DD

The Si photodiode [2] evaluated in this analysis is the same as that used for theoretical modelling in section 2.2.1. Its active area is 17.9 mm^2, with its spectral response shown in Figure 4.1.

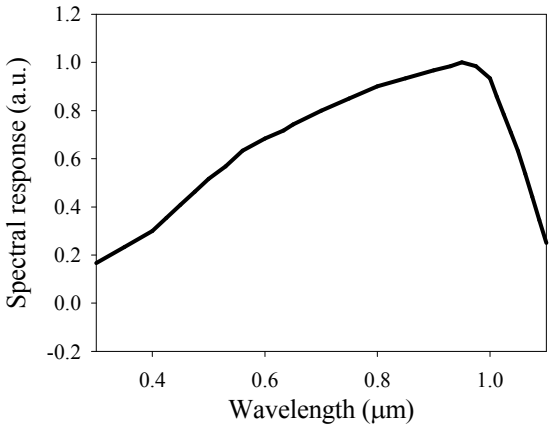

Figure 4.1 – Si photodiode spectral response [2]

The output voltage of the radiation thermometer system described in section 3.3.2 was measured as a function of T_{BB} using PSD and DD. Measurements were carried out over a period of 2 minutes for both PSD and DD at each T_{BB}, sampling at a rate of 0.05 s for PSD and 2 s for DD. These sampling rates were dictated by the measurement equipment used, resulting in sample sizes of 2400 and 60, respectively, for the two methods. It was found that the minimum sampling rate to achieve reliable measurement of the mean output voltage and SNR was 5 s for both PSD and DD, so these sampling rates were suitable. This was repeated six times at each T_{BB}, with the mean value of output voltage calculated. Figure 4.2(a) shows how these results compare with the theoretically calculated output voltage. Figure 4.2(b) shows how the natural logarithm of the output voltage compares with the inverse of the T_{BB}, along with the theoretical calculation.

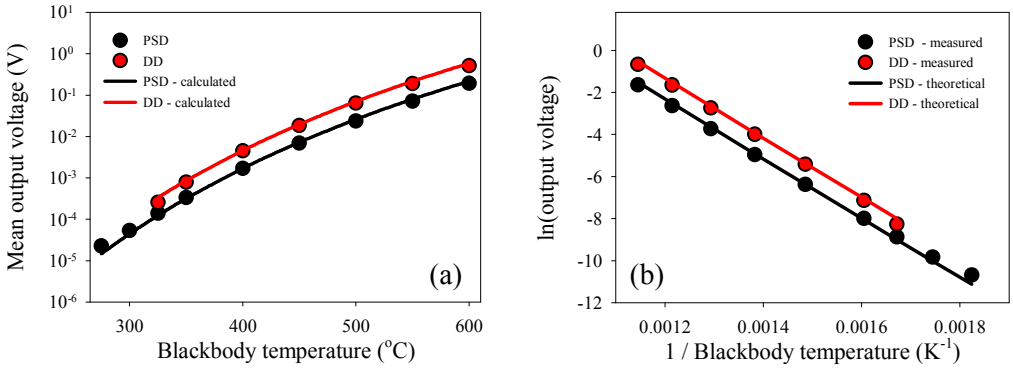

Figure 4.2 – (a) Measured and theoretical output voltage with T_{BB} using PSD and DD methods and (a) natural logarithm of output voltage against inverse of T_{BB} using PSD and DD methods at 0 V

PSD successfully measures lower T_{BB} than DD by ~50 °C in order to measure the lowest absolute T_{BB} possible by the thermometer, which is 275 °C for PSD. This minimum T_{BB} corresponds to the point where the signal can be distinguished from the noise floor of the thermometer setup. The lower T_{BB} measured by PSD was made possible by PSD's ability to retrieve the weaker signal from within the noise floor. The DD method is limited due to the output voltage being dominated by the amplified dark current. Therefore, in this instance, the smaller photocurrent cannot be distinguished from the noise floor.

The measured output voltage for both PSD and DD shows good comparison with theory, particularly at high T_{BB}. At low T_{BB}, the measured output voltage deviates from the theory slightly, resulting in the non-linearity to the graph shown in Figure 4.2(b). This is a result of the reduced photocurrent at low T_{BB} being comparable with the level of the dark current. Therefore, the effect of noise on the measured output voltage is greater, leading to inaccuracies in the measured output voltage using the lock-in amplifier. The use of this PSD technique with a lock-in amplifier has also been demonstrated by the National Institute of Standards and Technology [3] for measurement of low temperatures.

4.2.2 SNR and temperature error comparison for PSD and DD

Mean SNR as a function of T_{BB} was obtained from the output voltage measurements for both PSD and DD. This was obtained over the same 2 minute periods, repeated six times. Figure 4.3(a) shows the mean SNR, with Figure 4.3(b) showing a SNR improvement factor for the use of PSD over DD.

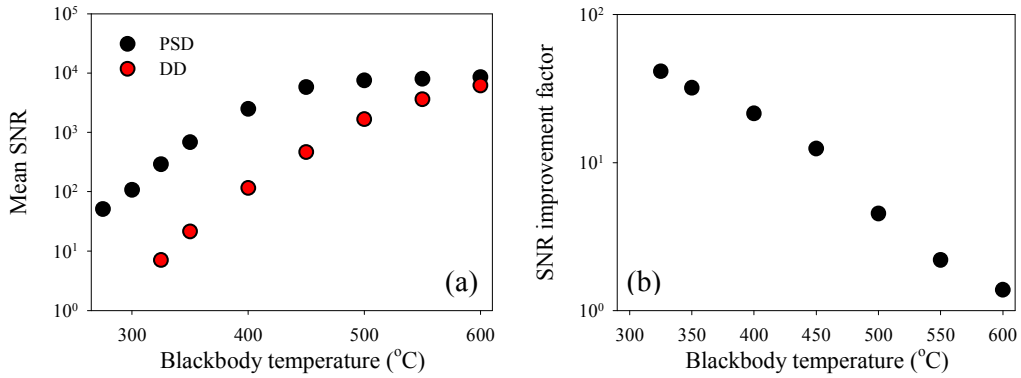

Figure 4.3 – (a) Mean SNR for Si photodiode using PSD and DD methods and (b) improvement factor for SNR by using PSD over DD at 0 V

Decreased T_{BB} results in decreased SNR for both PSD and DD. However, this decrease is more rapid for DD. For PSD, as T_{BB} reaches the higher temperature range, the SNR starts to saturate. At 600 °C, the SNR for both methods is similar, with an improvement factor of only ~1.4 times, whilst at 350 °C the improvement factor is ~32 times.

These results suggest PSD offers improvement in thermometer stability at low T_{BB}, but little improvement at high T_{BB}. The SNR is related to the ratio between the photocurrent and noise, contributed by the dark current and photocurrent induced shot noise as well as that from the amplifier. Therefore, as T_{BB} reduces, the photocurrent reduces. However, the dark current and amplifier noise stays constant, leading to a decrease in the SNR. With PSD able to successfully measure the photocurrent accurately, the effect of the dark current and amplifier noise is reduced. Therefore, the SNR for PSD will be higher than that of DD at low T_{BB}. At high T_{BB}, the photocurrent is significantly larger than the dark current. This leads to the noise being dominated by photocurrent induced shot noise; the benefit offered by PSD is negated. If the T_{BB} were to increase further, the improvement factor would tend towards unity. This implies that the benefit provided by PSD reduces as temperature increases.

In order to demonstrate the improvement offered by PSD, Figure 4.4 shows a typical example of how the output voltage varies with time over a 2 minute period at T_{BB} = 350 ^{o}C. Comparison is made between PSD and DD, with the output voltage fluctuation calculated as a percentage; 100 % is taken as the mean output. Both PSD and DD methods exhibit fluctuation over time. However, this fluctuation is greatly reduced for the PSD method. This demonstrates the benefit of PSD for measuring T_{BB} = 350 ^{o}C.

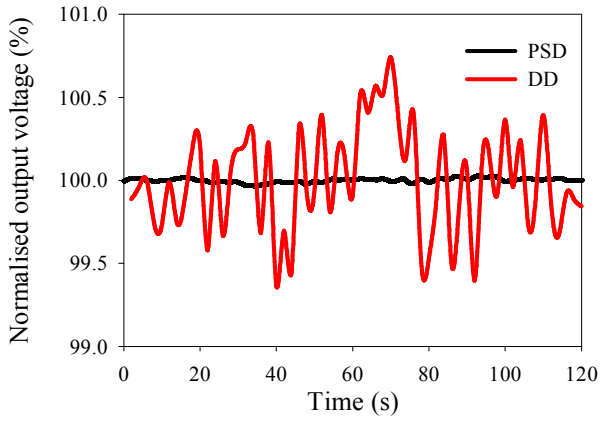

Figure 4.4 – Normalised output voltage fluctuation over time for PSD and DD methods for Si photodiode for detection of T_{BB} = 350 ^{o}C at 0 V

Using this fluctuation, and the *%/°C* calculated as a function of T_{BB}, the temperature error across the T_{BB} range can be calculated for both PSD and DD. This is shown in Figure 4.5.

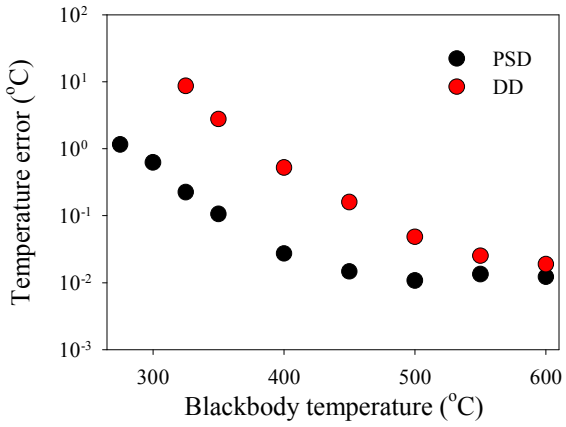

Figure 4.5 – Temperature error for unbiased Si photodiode with T_{BB} using PSD and DD methods at 0 V

At equivalent T_{BB}, the temperature error is lower for PSD than for DD, hence following the trend of the SNR. Again, the benefit of PSD is greater at lower T_{BB} than at higher T_{BB}, where the benefit is not so significant. For the measurement of T_{BB} = 350 °C the temperature error for PSD is ±0.11 °C, whilst for DD it is ±2.75 °C. Alternatively, if the temperature that needs to be measured is allowed a maximum level of temperature error of ±0.5 °C, PSD and DD can measure T_{BB} = ~305 and ~400 °C, respectively. This highlights the benefits PSD offers for the measurement of such temperatures.

The use of PSD obviously requires the use of an optical chopper system. Although this added mechanical component may be undesirable, its benefits are clear. It enables measurement of a lower temperature with reduced temperature error. However, it also allows a shorter wavelength detector to be used to measure a temperature which would normally require a longer wavelength detector with DD. Since the error in the measured temperature is proportional to wavelength for a given change in emissivity, shorter wavelength operation means that a given change in emissivity will result in reduced error in the measured temperature.

4.3 Si APD for radiation thermometry

With PSD shown to offer benefit to radiation thermometry, the advantages of a Si APD are demonstrated in this section. For this analysis, a Hamamatsu Si APD model S2384 [4] is used, with an active area of 7 mm^2, along with the same Si photodiode analysed in section 4.2. A comparison between PSD and DD is also made for the Si APD.

4.3.1 Mean output voltage for Si APD

The Si APD was evaluated using variable temperature blackbody measurements at the same temperatures as the Si photodiode, using both PSD and DD. Figure 4.6 shows how the output voltage (measured using PSD) varies as a function of reverse bias voltage, corresponding to varied APD gain.

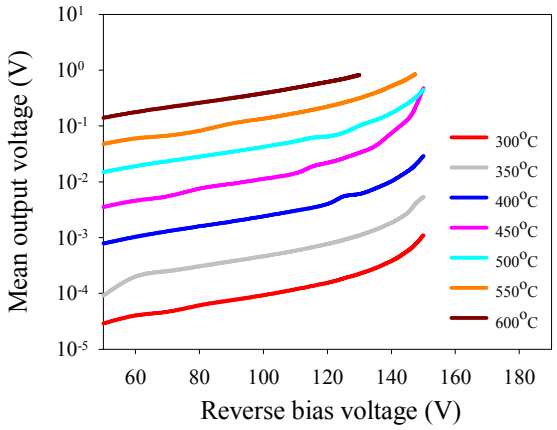

Figure 4.6 – Output voltage for Si APD with reverse bias voltage and T_{BB} using the PSD method

The output voltage increases with APD bias voltage and T_{BB}. As the reverse bias voltage increases, the internal avalanche gain of the APD increases, resulting in an increase in output voltage. However, the signal amplification by the avalanche gain does not improve the lowest absolute T_{BB} limit of 275 ^oC using PSD achieved by the Si photodiode. This is believed to be due to a background induced noise floor. By repeating the measurement with the blackbody source switched off, the noise floor remained at the same values for the corresponding gains when measured below 275

^{o}C. This suggests that the noise floor is dominated by the background signals and the amplifier. The lower T_{BB} limit of 275 ^{o}C is due to unoptimised shielding from background sources. Measurement of lower T_{BB} may be possible by using an improved photodiode shield with a well defined aperture and an optimised APD-TIA combination. For example, a measurement setup which completely shields the APD from background radiation is likely to result in the measurement of lower T_{BB} due to the measurement noise floor being lower. However, as it stands, these results suggest that the increased sensitivity of the Si APD does not offer reduction in the absolute minimum temperature which can be measured.

4.3.2 APD gain with blackbody emission wavelength and power

By normalising the measured output voltage to the value at 40 V, approximate gain values for the Si APD can be calculated, as shown in Figure 4.7 for T_{BB} = 300 and 500 ^{o}C.

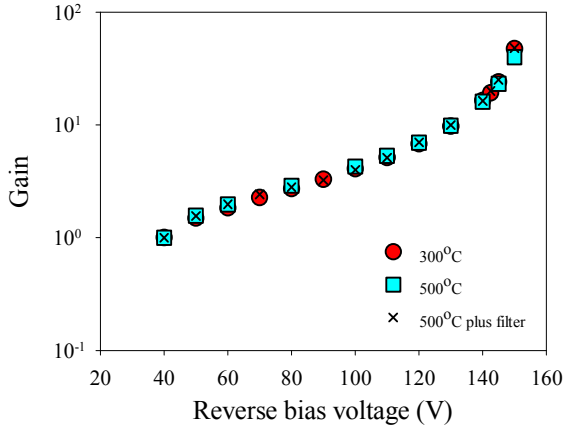

Figure 4.7 – APD gain at T_{BB} = 300 and 500^{o}C with bias voltage. Also plotted is APD gain with bias voltage at T_{BB} = 500 ^{o}C using a filter wheel to reduce the photocurrent to the equivalent of T_{BB} = 300 ^{o}C

APD gain shows very close if not identical performance of its characteristics up until an applied bias voltage of 150 V across the T_{BB} range. In order to confirm that the avalanche gain is not affected by changes in the blackbody power or spectra, a series of measurements were performed. This involved using a fixed T_{BB} and a variable neutral density optical filter wheel to measure the gain at different levels of

photocurrent, with the reduction in the incident radiation equal across the wavelength range. For example, with T_{BB} = 500 ^{o}C, Figure 4.7 shows how the filter wheel modelled T_{BB} = 300 ^{o}C. The gain measurement under these conditions again showed similar characteristics to the measurement performed at T_{BB} = 300 ^{o}C. Therefore, these results confirm the APD's gain is independent of radiation power and emission spectra in the tested range of T_{BB} up to 150 V. The exact value of avalanche gain is difficult to quantify due to uncertainties in establishing the unity gain reference and the exact carrier generation profile within the depletion region. This requires knowledge of the field profile of the APD.

4.3.3 Threshold voltage improvement over Si photodiode

Although no improvement in the lower detection temperature is achieved with the use of the Si APD, the output voltage of the circuit clearly increases with the internal gain of the APD, as shown in Figure 4.6. The APD produces higher photocurrent and, with the fixed gain of the amplifier, it makes it easier for the following electronics. With the SNR being increased by the APD, it is straight forward to add further amplification. This increased output voltage is therefore possible due to the increased sensitivity of the APD.

In practical radiation thermometers, the ADC in the thermometer, used for signal conditioning, requires a pre-defined input voltage value. For a fixed TIA gain, the larger output voltage which the APD provides allows the APD-TIA module to supply a given level of threshold voltage at a lower T_{BB} than the Si photodiode, as shown in Figure 4.8, using the PSD method.

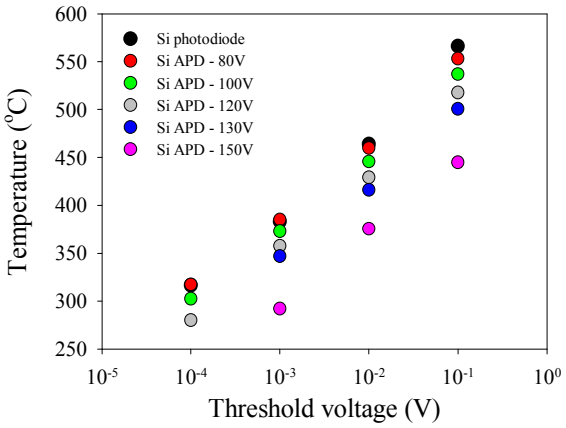

Figure 4.8 – Minimum T_{BB} achievable to satisfy a defined threshold voltage for the unbiased Si photodiode-TIA at 0 V, and Si APD-TIA at different APD bias voltages, using PSD

As APD bias voltage increases, the minimum T_{BB} achievable to satisfy specific bias voltages decreases. For instance, for a threshold voltage of 1 mV, the APD biased at 150 V measures minimum T_{BB} of 292 °C, whilst the Si photodiode measures minimum T_{BB} of 383 °C. Therefore, this yields an improvement of 91 °C. An improvement as large as 121 °C is obtained for a threshold voltage of 100 mV. These results confirm the benefit of using an APD with PSD to provide additional amplification to that provided by the TIA.

Therefore, the increased sensitivity of the Si APD does indeed offer measurement of lower T_{BB} compared to the Si photodiode. This suggests it could be used as an alternative to longer wavelength photodiodes, such as InGaAs or Ge, to measure lower temperatures whilst still operating at a shorter wavelength.

4.3.4 SNR and temperature error comparison for Si APD and Si photodiode

The avalanche mechanism contributes additional excess avalanche noise, adding to the total noise of the detector. Therefore, if the increased sensitivity of the Si APD is to be fully utilised, it is important to establish whether the use of APDs introduces an unacceptable level of excess noise which negates the benefit of measuring lower temperatures. In the same way as with the Si photodiode, the output voltage was recorded over a duration of 2 minutes for the Si APD at a sampling rate of 0.05 s

using PSD. Six sets of measurements were carried out at each T_{BB} and bias voltage combination to produce a mean SNR. Figure 4.9 shows an example of the typical fluctuation in the output voltage for the Si APD biased from 80 to 150 V at a T_{BB} of 300 ^{o}C. Also shown is the output voltage of the Si photodiode, at 0 V. The output voltages have been normalised to their mean values for each photodiode and bias combination with 100 % representing the mean.

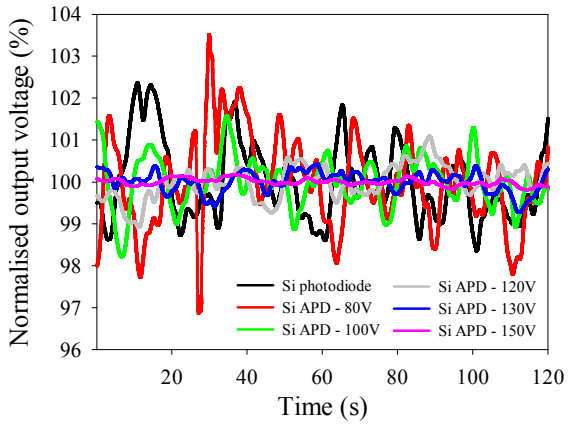

Figure 4.9 – Normalised output voltage for Si photodiode at 0 V and Si APD with bias voltage at T_{BB} = 300 ^{o}C, with 100 % corresponding to the mean value, using PSD

As the APD gain increases, the level of fluctuation decreases; a small percentage error of ±0.19 % is seen for a reverse bias of 150 V. This is significantly smaller than an error of ±2.54 % for the Si photodiode. This indicates that the SNR has been improved by the APD by amplifying the signal to a level such that the fluctuation of the output voltage from the electronics has become negligible. This shows that not only does the Si APD offer the measurement of lower T_{BB}, but sufficient gain will produce less variation in the output voltage that the Si photodiode. Therefore, the use of a Si APD as a detector in radiation thermometry is indeed viable with its increased sensitivity able to be fully utilised.

It was not possible to measure data at high T_{BB} and high bias voltage due to the input voltage limit of the lock-in amplifier. At low T_{BB}, the SNR increases when APD gain increases with reverse bias voltage. As T_{BB} increases, the rate at which the SNR

increases becomes progressively smaller with T_{BB}; no significant increase in SNR is observed above 450 °C. At low T_{BB}, the APD gain increases the signal such that the SNR increases; the noise is dominated by the amplifier. As T_{BB} increases, the shot noise from the APD, which originates from the multiplied photocurrent, starts to dominate the system noise. Hence, this prevents the SNR from increasing with bias. In addition, the excess noise factor increases as the APD gain increases. This leads to the degradation seen in the SNR, particularly at high APD gain and high T_{BB}. This implies that there is an upper temperature limit to the benefit provided by high APD gain. However, this gain is beneficial for the measurement of lower temperatures. The SNR of the APD-TIA at different T_{BB} is shown in Figure 4.10.

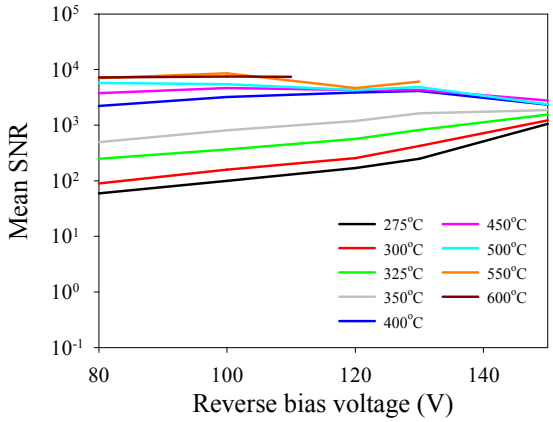

Figure 4.10 – Mean SNR of the APD-TIA at different T_{BB} using PSD

These measurements were repeated for the Si APD using the DD method. Figure 4.11 shows how the mean SNR varies with use of PSD and DD for the Si photodiode at 0 V and the Si APD with bias, with T_{BB} = 350 °C. This temperature was chosen as it could be measured using both the PSD and DD methods, whilst also representing a temperature lower than the current ~400 °C limit of DD Si photodiode radiation thermometers.

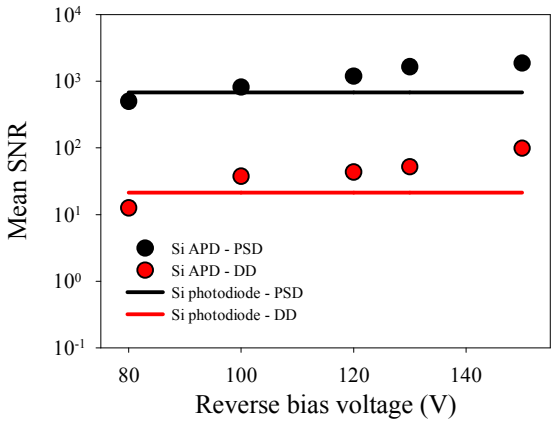

Figure 4.11 – Mean SNR for the unbiased photodiode and Si APD with bias voltage using PSD and DD at T_{BB} = 350 ^{o}C

For the Si photodiode, PSD resulted in an enhancement in the SNR of ~32 times compared with using DD. For the Si APD at 150 V, the improvement in SNR was ~19 times with the use of PSD over DD. Therefore, an overall enhancement in SNR provided by using the PSD Si APD over the DD Si photodiode was ~88 times, whilst ~2.7 times improvement was seen when both photodiodes used PSD. This shows the benefits of the combined PSD-APD system. It should be noted that the Si photodiode is ~2.6 times larger than the Si APD. Whereas this results in a larger shot noise component from the detector, the overall noise of the measurement is dominated by the amplifier. Therefore this small difference in the detector area has little effect on the results.

These results can be converted to temperature error with use of the fluctuation over time and the *%/°C* of the Si APD. The temperature error at T_{BB} = 350 ^{o}C, using both PSD and DD, is shown for the Si photodiode and Si APD in Figure 4.12.

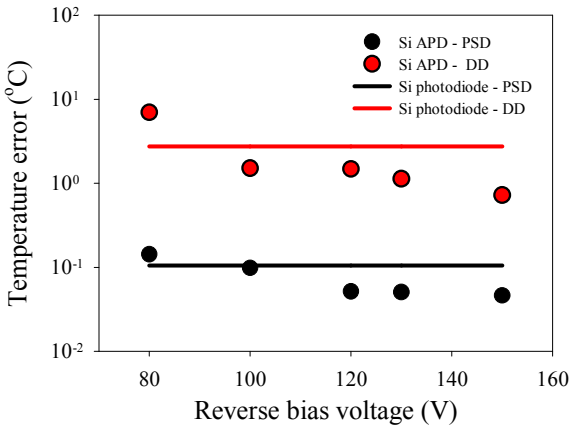

Figure 4.12 – Temperature error for unbiased photodiode and Si APD with bias voltage using PSD and DD at T_{BB} = 350 °C

Once again, it is clear that the use of PSD over DD offers improvement to the thermometer performance. For the Si photodiode, PSD improves the temperature error from ±2.75 to ±0.11 °C. The use of the Si APD with PSD at 150 V improves this again to ±0.05 °C. A similar improvement in the temperature error was found with the use of the Si APD at lower T_{BB}.

Although it is clear that the PSD-APD system offers improvement over the DD-photodiode system, it is important to emphasise the benefit of a DD-APD system over a DD-photodiode system. Figure 4.11 shows increased SNR for the Si APD at all bias voltages above 100 V in comparison with the Si photodiode, whilst Figure 4.12 shows reduced temperature error. This highlights the benefit of the more sensitive APD even without the use of PSD. The DD-APD would be expected to demonstrate similar improvement in ability to measure lower T_{BB} in order to achieve specific threshold voltages compared to the DD-photodiode. The more sensitive Si APD therefore offers great potential to radiation thermometry whatever measurement technique is used.

4.4 Conclusion

A Si APD was demonstrated as a more sensitive detector technology for radiation thermometry in comparison with a Si photodiode. Its high internal gain was shown to

offer benefit by the successful measurement of lower minimum T_{BB} in order to satisfy specific threshold voltages. This therefore allows the thermometer to operate at a shorter wavelength in order to measure temperatures which would previously only be possible by using a longer wavelength detector. In addition, the use of the Si APD was shown to not add additional excess noise to the thermometer system. In fact, with the correct amount of gain used, the Si APD achieved a higher SNR and a lower temperature error than the Si photodiode. The use of PSD was also shown to offer measurement of lower T_{BB} with higher SNR and lower temperature error compared with DD, for both the Si photodiode and Si APD. This also allows lower temperatures to be measured without using a longer wavelength detector. The combined use of the Si APD with PSD offered the best performance and significant advantages over the Si photodiode using DD in terms of SNR and temperature error. However, even if DD were to be used, the Si APD still demonstrated improvement in both SNR and temperature error over a Si photodiode using DD. Therefore, the Si APD is a viable technology for radiation thermometry, with benefits provided by its increased sensitivity.

References

[1] M. J. Hobbs, C. H. Tan, and J. R. Willmott, "Evaluation of phase sensitive detection method and Si avalanche photodiode for radiation thermometry," *Journal of Instrumentation,* vol. 8, p. P03016, 2013.

[2] Hamamatsu Photonics, *Si Photodiodes - S2386 series*. Available: http://www.hamamatsu.com/resources/pdf/ssd/s2386_series_kspd1035e06.pdf, (2013).

[3] G. Eppeldauer and H. Yoon, "AC-Mode Short-Wavelength IR Radiation Thermometers for Measurement of Ambient Temperatures," *International Journal of Thermophysics,* vol. 29, pp. 1041-1051, 2008.

[4] Hamamatsu Photonics, *Si APD - S2381 to S2385, S5139, S8611, S3884, S4315 series*. Available: http://sales.hamamatsu.com/assets/pdf/parts_S/s2381_etc_kapd1007e09.pdf, (2010).

Chapter 5 – Mid-wave infrared InAs/GaSb type-II superlattice for radiation thermometry

5.1 Introduction

The next motivations behind developing the next generation of infrared detectors for radiation thermometry include minimally cooled longer wavelength detection, versatile longer wavelength single- and multi-colour detection and the potential for array implementation. The current generation of mid-wave infrared (MWIR) detectors have limitations such as slow operation, drift over time or the need for intensive cooling. Longer wavelength ratio radiation thermometry currently makes use of broadband detectors with filters, with any flexibility in the detection wavelengths determined by these filters. However this is undesirable and expensive, as is the alternative of using cooled two-colour MCT. Additionally, the implementation of longer wavelength photon detectors as arrays for radiation thermometry has great potential. This capability would be attractive for monitoring the temperature of low temperature objects over a larger area of their surface. The MWIR InAs/GaSb type-II superlattice (T2SL) is a viable candidate for meeting all these desirable qualities. It has the potential for uncooled operation, is wavelength tunable and can be grown as an array. This wavelength tunability allows the T2SL to be tuned to application specific peak wavelengths, whilst also allowing versatile longer wavelength two-colour detectors to be grown for ratio radiation thermometry. Its potential for growth as an array, whilst incorporating its other qualities, makes it hugely attractive for radiation thermometry.

This chapter evaluates the T2SL for use in radiation thermometry. Three structures with different absorption region doping concentrations were investigated in terms of room temperature dark current. The structure with the lowest dark current was then fully characterised as a function of temperature, both electrically and optically. It was demonstrated for use in radiation thermometry at low and room temperature [1], with evaluation of its SNR and temperature error.

5.2 MWIR InAs/GaSb T2SL characterisation

5.2.1 Device structure and fabrication

Figure 5.1 shows the schematic of three T2SL detectors, with the detectors grown on 2 inch GaSb substrates. An n-type cladding layer was grown directly onto the substrate, followed by an absorption layer and then a p-type cladding layer. The highly doped cladding layers are designed to confine the electric field to the absorption layer where the photons are absorbed. Each detector is identical except for the level of doping within the 2 μm thick absorption region. Different p-type dopant (using Be) concentrations were incorporated in the absorption regions. These detectors will be referred to as T2SL1, T2SL2 and T2SL3, corresponding to doping concentrations of undoped, 1×10^{16} and 1×10^{17} cm^{-3}, respectively. The SLS period of these detectors is 10ML/10ML, with the detectors grown at the University of New Mexico.

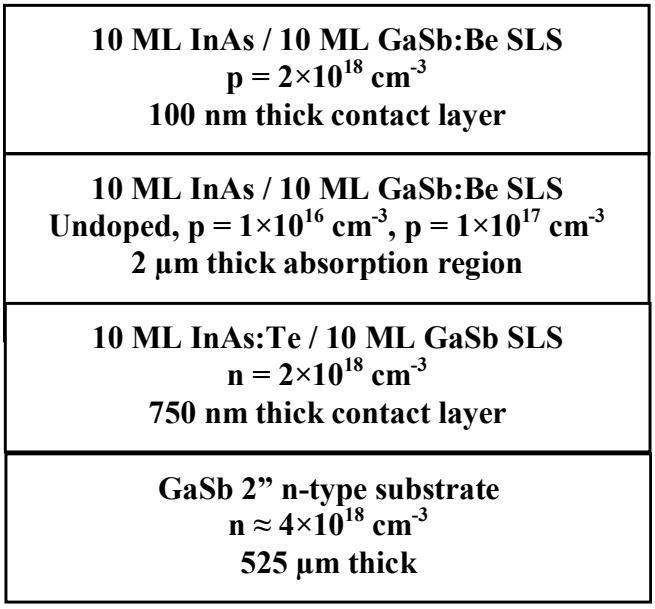

Figure 5.1 – Schematic of T2SL1, T2SL2 and T2SL3

For characterisation, the three detectors were fabricated into mesa diodes[a] with areas of 1 × 1, 1 × 0.5 and 0.21 × 0.235 mm^2 using wet chemical etching at the UK EPSRC National Centre for III-V Technologies at the University of Sheffield. These

[a] Diodes formed by growing the structure epitaxially across the whole wafer and then isolating individual diodes by etching away the material

will be referred to as 'large', 'medium' and 'small' for the purposes of this analysis. The chemical etchant used was a solution of H_3PO_4:$C_6H_8O_7$:H_2O_2:de-ionised water (mixed in the ratio of 1:1:1:1), with etching of the mesa diodes to the GaSb substrate to ensure isolation of all diodes. On-wafer measurements were used for electrical characterisation. The diodes were packaged onto TO-5 headers for optical characterisation.

5.2.2 Electrical characterisation

On-wafer dark current density measurements were carried out on the three detectors for large, medium and small diodes at room temperature. Figure 5.2 shows these measurements for large and medium diodes.

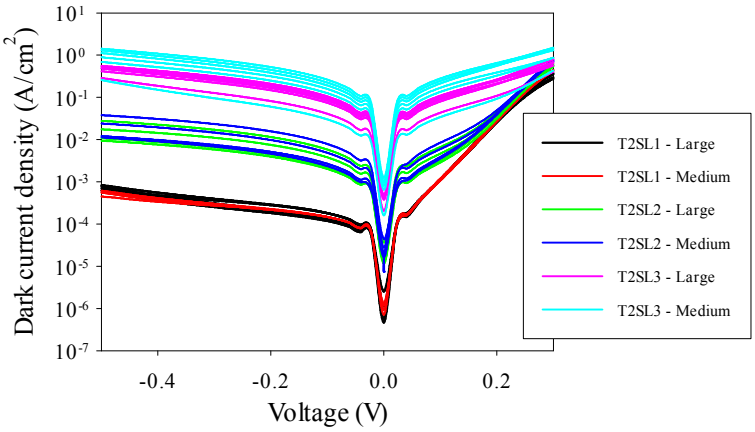

Figure 5.2 – Dark current density for T2SL1, T2SL2 and T2SL3 for large and medium diodes at room temperature

A 0 V dark current density of below 1×10^{-6} A/cm^2 was measured for T2SL1. This is amongst the lowest in the known literature for such a detector, suggesting that the non-intentional background doping within this detector is acceptably low. The dark current density for T2SL1 appears to scale well with area suggesting a dominant bulk current, although there appears to still be an element of surface leakage. This becomes more noticeable for the small area diodes. As the absorption region doping increases for T2SL2, so does the dark current density, with this trend continuing for T2SL3. Additionally, the dark current density begins to scale less well with area for T2SL2, getting worse again for T2SL3.

These results show that additional doping within the absorption region leads to increased dark current. Therefore, for noise to be minimised and D* maximised, absorption region doping concentration should be as low as possible. Work needs to be focused on minimising the background doping of the absorption region for further reduction in dark current and increased depletion. In addition to this, further investigation into the causes and treatment of the surface leakage current should be performed.

Due to its low dark current, T2SL1 was chosen for full characterisation prior to demonstration within a radiation thermometer system. Temperature dependent on-wafer dark current density measurements were performed on T2SL1, with Figure 5.3 showing the results for a large diode.

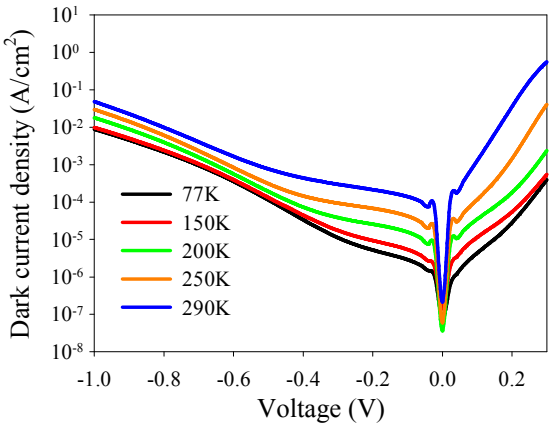

Figure 5.3 – Dark current density of T2SL1 for large diode with temperature

Cooling T2SL1 down to 77 K yielded an improvement in the dark current by ~2 orders of magnitude at low reverse bias, with reduced reduction at higher reverse bias. The surface component is highlighted by the reduction of dark current with temperature; a purely bulk current would be expected to decrease more greatly with temperature. Also, the dark current density scales less well with area at lower temperatures; the bulk current reduces whilst the surface leakage current does not. At reverse bias voltages greater than -0.5 V, the dark current reduction with temperature is less, indicating a tunnelling component.

Temperature dependent CV measurements were carried out upon T2SL1 in order to investigate the depletion width. This is shown for a large diode in Figure 5.4. The T2SL material consists of alternating MLs of InAs and GaSb, which have dielectric constants of 15.15 and 15.7, respectively. Therefore, a dielectric constant of 15.4 was assumed for the T2SL [2]. Due to the phase angle of the CV measurement being > 70°, these results can be taken as a reliable measurement of the capacitance and estimation of the depletion width.

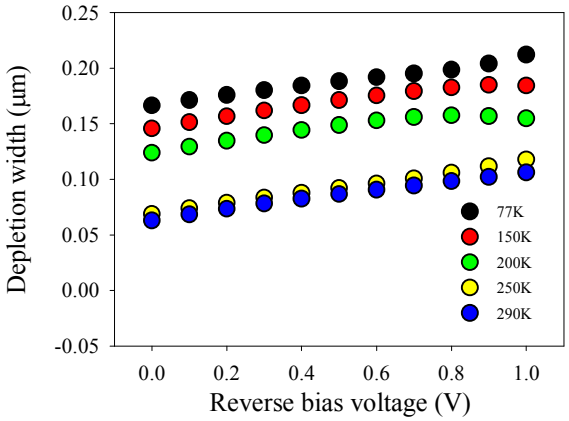

Figure 5.4 – Depletion width with temperature for T2SL1

Cooling of the detector resulted in an increase in the depletion width, as did increased reverse bias. However, these increases are relatively small. The small depletion is an issue as it reduces the quantum efficiency of the diodes as discussed in section 2.3.2.

5.2.3 Optical characterisation

The spectral response was successfully measured from 77 K up to room temperature. Figure 5.5 shows how the spectral shape varies with temperature between 77 and 290 K, with (a) showing the spectral intensity and (b) showing the normalised response. These measurements were performed at 0 V to maintain the low dark current.

As temperature reduces, there is an increase in the spectral intensity as well as a reduction in the cut-off wavelength, although this is not so clear due to the longer wavelength's response becoming relatively weak at higher temperature. These

spectra suggest that there are different peaks dominating at different temperatures. For example, at higher temperature, a peak starts to be observed below 1.7 µm. Additionally, the spectral shape becomes increasingly noisy at higher detector temperatures.

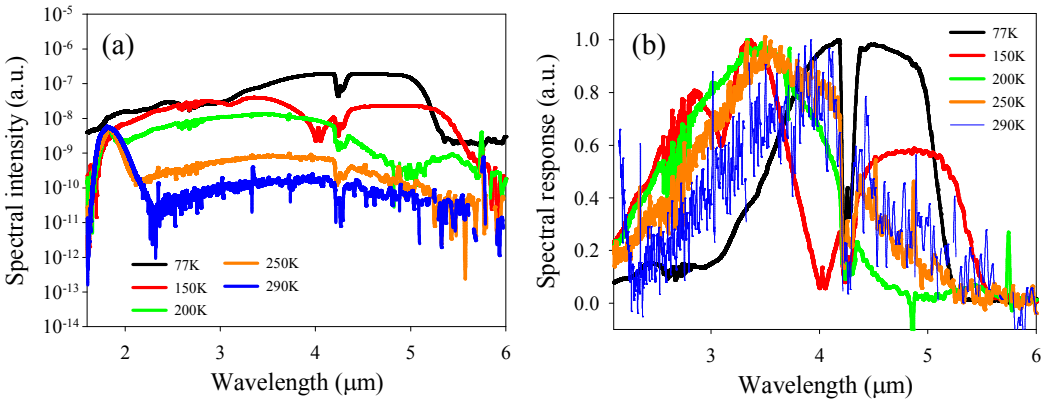

Figure 5.5 – (a) Spectral intensity and (b) normalised spectral response with temperature for T2SL1 at 0 V

The temperature dependence of the cut-off wavelength is due to a change in the band overlap. As temperature increases, the band overlap increases [3] leading to a decrease in the effective bandgap of the superlattice. Hence, a shift to longer wavelengths occurs at higher temperature. The spectral peak variation indicates different transitions dominating at different temperatures. For instance, the transition below 1.7 µm is believed to be due to the GaSb, with the remaining peaks believed to be due to transitions from the effective T2SL bandgap. As temperature is reduced, the peak below 1.7 µm reduces. The exact reason for these peak variations is not fully known and requires further investigation. The dip in the spectral response at 4.2 µm is an atmospheric absorption feature to CO_2, as is the feature at 2.7 µm. Although not clear in the figures, there is also an absorption feature at 3.2 µm which corresponds to H_2O.

Temperature dependent peak responsivity and D* were calculated for T2SL1 by performing fixed point blackbody measurements. T_{BB} = 1000 ^{o}C was used with a 3.17–5 µm MWIR filter placed between T2SL1 and the blackbody source. The use

of this filter was necessary due the strong room temperature response below 1.7 μm originating from the GaSb. The photocurrent from the sample was amplified using the pre-amplifier, with the blackbody signal chopped at ~810 Hz. Temperature dependent peak responsivity and thermal noise limited D* are shown in Figure 5.6 for 0 V operation.

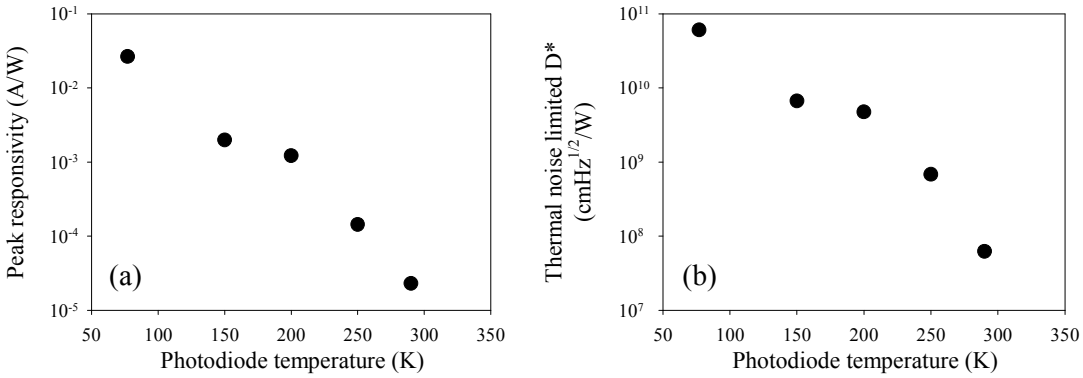

Figure 5.6 – (a) Peak responsivity and (b) thermal noise limited D* with T2SL1 temperature at 0 V

A MWIR photocurrent was successfully measured at room temperature using the blackbody and filter combination. Cooling of the detector to 77 K resulted in a large improvement in the responsivity and D* by ~4 and ~3 orders of magnitude, respectively, with a calculated D* of 6.2×10^{7} cmHz$^{1/2}$/W at room temperature increasing to 6.1×10^{10} cmHz$^{1/2}$/W at 77 K. Application of a bias voltage resulted in no significant improvement in the peak responsivity, but resulted in reduced D*, as shown in Figure 5.7. For example, a -0.1 V bias at room temperature produced a D* of 2.6×10^{6} cmHz$^{1/2}$/W. With weak bias dependence in the peak responsivity, and significant increase in the dark current with bias voltage, this result is expected.

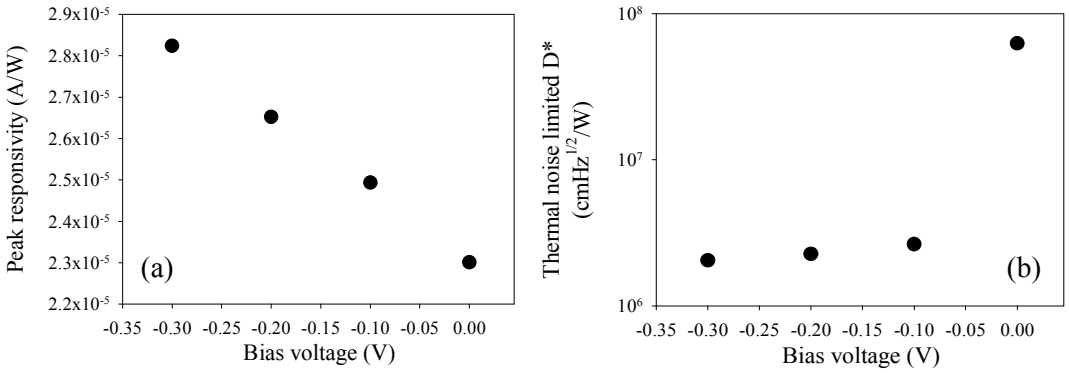

Figure 5.7 – (a) Peak responsivity and (b) thermal noise limited D* for T2SL1 with bias voltage at room temperature

This measured responsivity of less than 0.1 A/W at 77 K is relatively low, but due to low dark current the D* values of 6.1×10^{10} and 4.7×10^{9}cmHz$^{1/2}$/W at 77 and 200 K, respectively, are comparable with other authors. At room temperature, the low D* of 6.2×10^{7} cmHz$^{1/2}$/W explains why the room temperature spectral response is so noisy.

Several theories have been discussed as to why this increase in photocurrent with cooling exists. Neither cooling of T2SL1 nor increase in bias voltage had significant effect on the depletion width, suggesting that the main cause of increased photocurrent at low temperature is not increased absorption in the depletion region. This also explains the weak bias dependence in the peak responsivity, and therefore reduced D* with bias voltage. It has been reported that T2SLs consist of a large g-r component in the bulk current [4], indicating the presence of defects such as traps within the detector. Due to the challenges presented by growth of T2SLs, such defects are developed during the growth of the detectors [5]. Figure 5.8 demonstrates how such trap centres, or Shockley-Read-Hall (SRH) centres, are located within the bandgap. Trap related recombination can be explained by illustration of the energy transitions within the bandgap. If the energy required for an electron (or hole) to move from the conduction (or valence) band is less than it is for it to move to the trap state than to the valence (or conduction) band, it will lead to trap related recombination. This results in carriers recombining and reduces the carrier lifetime. Other authors have shown that reduced carrier lifetime in T2SLs is a result of

recombination at such centres [6]. This reduced carrier lifetime has been proposed as the reason for decreased responsivity at high temperature.

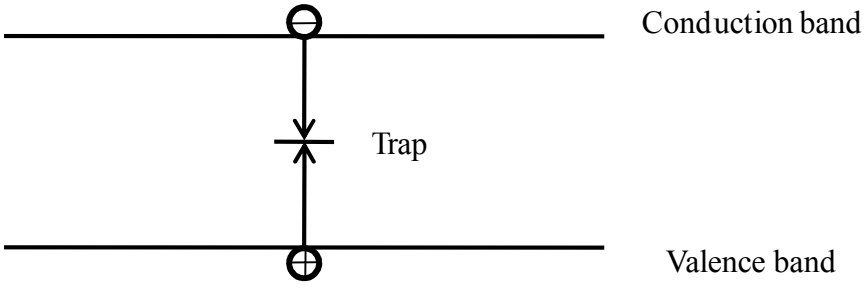

Figure 5.8 – Trap related recombination

At high temperature, the carriers generated by photon absorption have sufficient thermal energy, which leads to the traps frequently emptying and filling again. Therefore, only a very small amount of carriers contribute to the photocurrent. As the temperature is reduced, the thermal energy reduces, leading to carriers remaining in the traps for longer. This in effect reduces the number of trap centres. From the point of view of the other carriers, they can now diffuse over a longer distance without recombining. This leads to increased photocurrent at the contacts, with the end result being improved responsivity and D* with cooling.

5.3 MWIR InAs/GaSb T2SL for radiation thermometry

Variable temperature blackbody radiation thermometry measurements were carried out on T2SL1 using PSD and the setup outlined in section 3.3.3. The mean photocurrent of T2SL1 as a function of T_{BB} is shown in Figure 5.9(a) with T2SL1 cooled to different temperatures. This mean photocurrent was measured over a 2 minute duration, sampling every 0.05 s to yield a 2400 sample data set for each blackbody and T2SL temperature combination. All measurements were performed at 0 V. Comparison of the mean photocurrent at T_{BB} = 50 ^{o}C was chosen as the main reference temperature for this analysis due to its relevance to the motivation of developing MWIR detectors for low temperature radiation thermometry measurement applications.

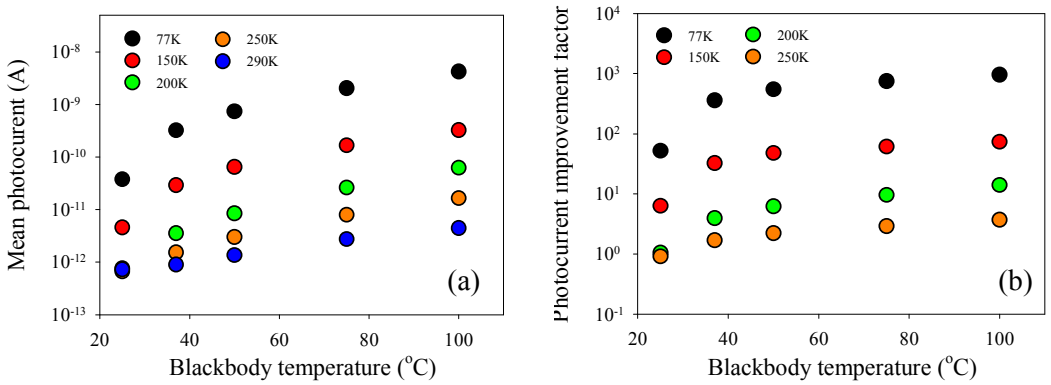

Figure 5.9 – (a) Mean photocurrent and (b) photocurrent improvement factor with T_{BB} and T2SL1 temperature at 0 V

A weak but repeatable photocurrent could be measured at T_{BB} = 25 °C with an uncooled T2SL1. This therefore indicates the potential of using uncooled T2SL for radiation thermometry. Significant improvement in the photocurrent with cooling was observed, as shown in Figure 5.9(b), where the photocurrent is normalised to its measured value at 290 K. This normalisation was carried out taking the photocurrent measured for each diode temperature and T_{BB} combination, and dividing them by the correlating T_{BB} photocurrent for a diode temperature of 290 K. For instance at T_{BB} = 50 °C, improvement factors of 2.2, 6.2, 48 and 547 when the diode was cooled to 250, 200, 150 and 77 K, respectively, were obtained. This improvement in photocurrent with cooling is consistent with the increase in responsivity with cooling. It is noted that this improvement is greater at higher T_{BB} due to an increased spectral overlap between blackbody emission and T2SL1's spectral response.

As T_{BB} approaches 20 °C, the measurement was limited by the unoptimised shielding of T2SL1 from the ambient background. The T_{BB} has become less than the surrounding environment's temperature. This surrounding environment presents a challenge in radiation thermometry [7]. Lower T_{BB} could be successfully measured if the setup were fully shielded from the surrounding environment, with the optical chopper cooled to a lower temperature than the T_{BB}. Alternatively, a technique could be implemented which measures and deducts the chopper temperature from the total measured temperature.

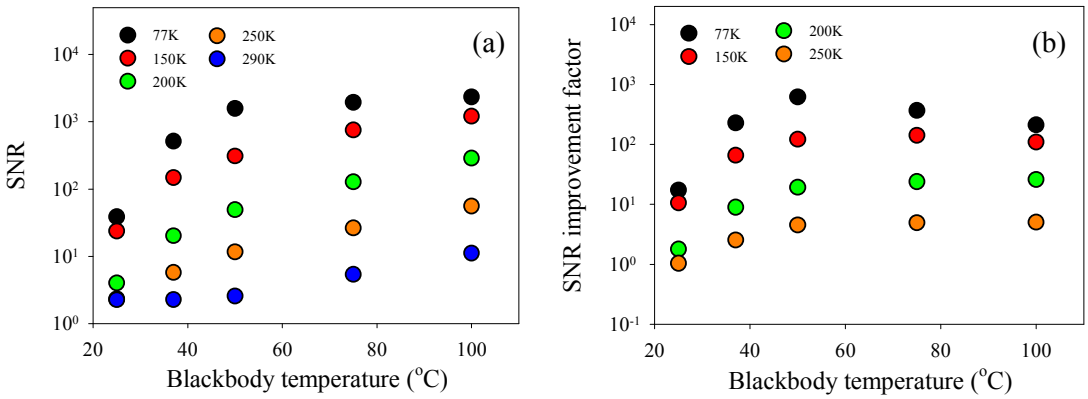

Figure 5.10 – (a) Mean SNR and (b) SNR improvement factor with T_{BB} and T2SL1 temperature at 0 V

An assessment of T2SL1's temperature dependence of SNR, along with its corresponding improvement factor with cooling, is shown in Figure 5.10. At room temperature, SNR > 1 was measured even at T_{BB} = 25 °C. An increased photocurrent from either cooling T2SL1 or increased T_{BB} resulted in improvement in SNR. However, it was observed that at a diode temperature of 77 K, the SNR increase seems to be saturating with increasing T_{BB}. This is due to the slowing increase of signal with temperature, as described by the Planck function, whilst the noise remains constant with temperature.

The SNR can be related to the level of fluctuation in the measured photocurrent, with a typical example of the fluctuation in photocurrent over a 2 minute period shown in Figure 5.11 for T_{BB} = 50 °C with diode temperatures of 77 to 290 K. The photocurrent is normalised to its mean values for each T2SL temperature and presented as a percentage; 100 % represents the mean photocurrent for each temperature.

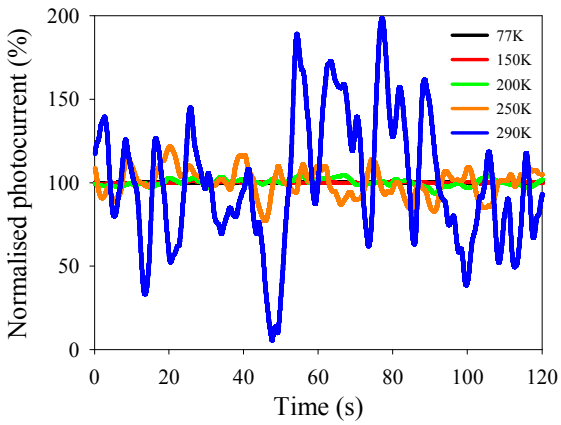

Figure 5.11 – Normalised output current over a 2 minute period at different temperatures of T2SL1 to detect T_{BB} = 50 ^{o}C, with 100 % representing the mean photocurrent

Significant reduction in the measured photocurrent fluctuation was observed with cooling; the percentage error reduces from ±97 % at room temperature for an uncooled diode to ±5.6 and ±0.1 % at 200 and 77 K, respectively.

These percentage errors can be related to a practical radiation thermometer by calculating the temperature error as a function of T_{BB}, as shown in Figure 5.12. A reduction in the temperature error as a function of T_{BB} was found with decreased diode temperature, following the trend in SNR. For example, for detection of T_{BB} = 50 ^{o}C, the error of ±34 ^{o}C for an uncooled diode is reduced to ±1 and ±0.03 ^{o}C for diode temperatures of 200 and 77 K, respectively.

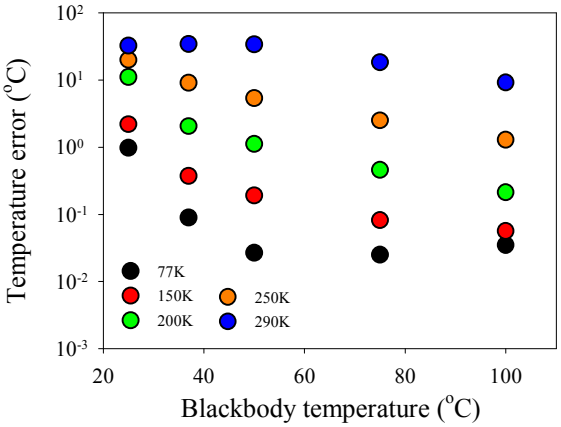

Figure 5.12 – Temperature error in target temperature with T_{BB} and TS2L temperature

This high temperature error obtained using uncooled T2SL suggests that, in its current form, it is not yet fully optimised for room temperature operation. However, these results demonstrate the potential of using moderately cooled T2SL. If a maximum temperature error of, say, ±0.5 °C is defined, T_{BB} of ~37, 50, 75 and 100 °C could be accurately measured by cooling the T2SL to 160, 175, 200 and 225 K, respectively. The latter two temperatures can therefore be achieved using thermo-electric cooling. However, measurement of T_{BB} = 50 °C could be achieved at 200 K with thermo-electric cooling if a temperature error of ±1 °C were to be deemed satisfactory.

These results indicate that improved performance of uncooled MWIR T2SL for radiation thermometry requires increased photocurrent at high temperature. For example, the quantum efficiency could be increased by increasing the carrier diffusion length and carrier lifetime. However, this requires improved growth of the superlattice material quality, with the depletion width maximised via minimising the unintentional background doping.

5.4 Conclusion

A MWIR InAs/GaSb T2SL detector was evaluated as a viable detector technology for radiation thermometry. The T2SL detector with the lowest absorber doping was able to detect T_{BB} = 25 °C with SNR > 1 whilst in uncooled operation. The

measurement of T_{BB} = 50 ^{o}C with a temperature error of ±0.5 ^{o}C could be achieved by cooling the detector to 175 K. However, measurement of T_{BB} = 50 ^{o}C could be achieved at the thermo-electric cooler compatible temperature of 200 K if a temperature error of ±1 ^{o}C were to be deemed satisfactory. This therefore demonstrated the potential for the minimally cooled T2SL to be used for temperature measurement applications requiring MWIR detection. Cooling of the T2SL increased the photocurrent and reduced the dark current, leading to improvement in the SNR and temperature error. Further investigation and development is required in order to optimise T2SL for use in radiation thermometry, but its potential has been demonstrated and discussed.

References

[1] M. J. Hobbs, C. H. Tan, X. Zhou, J. P. David, J. R. Willmott, E. Plis and S. Krishna, "InAs/GaSb type-II superlattice for radiation thermometry," *Accepted for publication in IEEE Transactions on Instrumentation and Measurement on* 19th June 2014.

[2] A. Hood, D. Hoffman, Y. Wei, F. Fuchs, and M. Razeghi, "Capacitance-voltage investigation of high-purity InAs⁄ GaSb superlattice photodiodes," *Applied physics letters,* vol. 88, p. 052112, 2006.

[3] D. Symons, M. Lakrimi, M. Van der Burgt, T. Vaughan, R. Nicholas, N. Mason*, et al.*, "Temperature dependence of the band overlap in InAs/GaSb structures," *Physical Review B,* vol. 51, pp. 1729-1734, 1995.

[4] E. Plis, J. B. Rodriguez, and S. Krishna, "6.06 - InAs/(In)GaSb Type II Strained Layer Superlattice Detectors," in *Comprehensive Semiconductor Science and Technology*. vol. 6, P. Bhattacharya, R. Fornari, and H. Kamimura, Eds., ed Amsterdam: Elsevier, 2011, pp. 229-264

[5] J. Shen, S. Y. Ren, and J. D. Dow, "Deep levels in type-II InAs/GaSb superlattices," *Physical Review B,* vol. 46, pp. 6938-6946, 1992.

[6] B. M. Nguyen, D. Hoffman, E. K. Huang, S. Bogdanov, P. Y. Delaunay, M. Razeghi*, et al.*, "Demonstration of midinfrared type-II InAs/GaSb superlattice photodiodes grown on GaAs substrate," *Applied Physics Letters,* vol. 94, p. 223506, 2009.

[7] P. Saunders, *Radiation Thermometry: Fundamentals and Applications in the Petrochemical Industry* vol. 78: SPIE press, 2007.

Chapter 6 – Mid-wave infrared InAs/GaSb type-II superlattice on GaAs substrate

6.1 Introduction

The uncooled (or minimally cooled) mid-wave infrared (MWIR) InAs/GaSb type-II superlattice (T2SL) has been evaluated in Chapter 5. However, to encourage mass exploitation of this technology it needs to be more affordable. This is particularly the case if the development of large area arrays is the end goal. T2SLs are traditionally grown on lattice matched GaSb substrates, which are comparatively expensive and are limited in their size. However, growth of T2SL on larger and cheaper GaAs substrates offers the potential for more affordable detectors, therefore making them more suitable for radiation thermometers.

This chapter evaluates a MWIR InAs/GaSb T2SL grown upon a GaAs substrate [1]. It was characterised both electrically and optically, before being evaluated for radiation thermometry. Comparison is made between the detector and the detectors grown on GaSb, with the challenges of realising improved T2SL performance discussed.

6.2 MWIR InAs/GaSb T2SL on GaAs substrate

6.2.1 Device structure and fabrication

Figure 6.1(a) shows the schematic of the T2SL grown on a 3 inch semi-insulating GaAs substrate, with Figure 6.1(b) showing an x-ray diffraction (XRD) curve for the T2SL. For the purposes of this thesis, this detector will be known as T2SL4. The XRD curve is shown here to demonstrate the growth quality for the T2SL on GaAs.

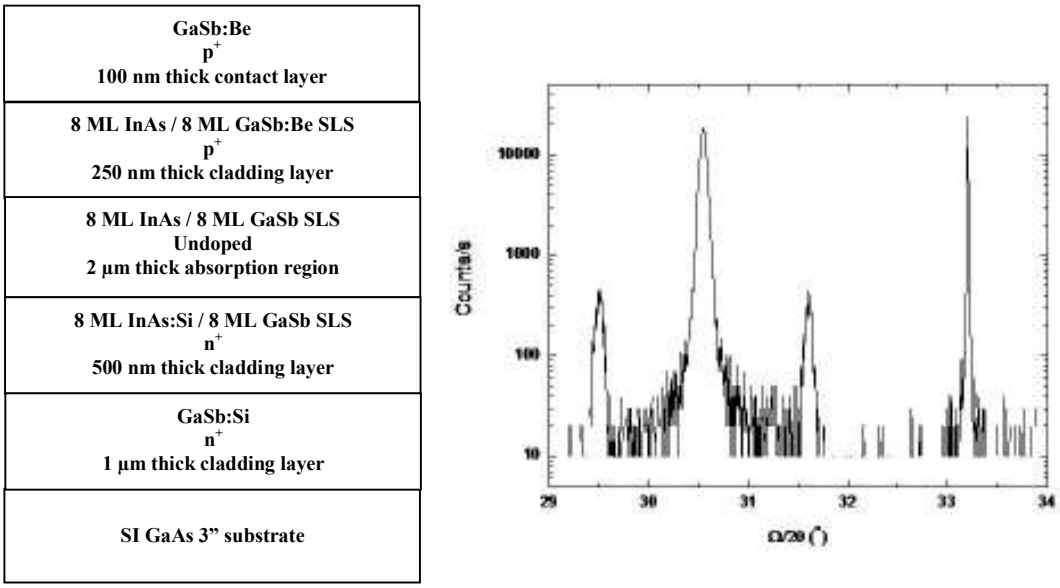

(a) (b)

Figure 6.1 – (a) Schematic and (b) XRD for T2SL4

Like T2SL1, the absorption region of T2SL4 is undoped, and is 2 μm in thickness. Unlike T2SL1, the structure had SL period of 8ML/8ML, with the detector also grown at the University of New Mexico. The XRD curve, which was also performed at the University of New Mexico, shows broader satellite peaks than similar detectors grown upon GaSb substrates. This indicates the presence of some non-uniformity, suggesting that there is still progress to be made with the growth of GaSb on GaAs. There is a peak at around 33.2°, which corresponds to the GaAs substrate. The peak at approximately 30.4° indicates successful growth of the SL with a period of 8ML/8ML. Therefore, this confirms that the detector could be successfully grown upon a GaAs substrate, despite the slight non-uniformity. This slight non-uniformity relates to the SLS period, resulting in variations in the thickness of each layer.

T2SL4 was fabricated into mesa diodes with radii ranging between 25 to 200 μm, using a combination of dry reactive ion etching and wet etching. The dry etching used Cl_2 and Ar plasma at a low pressure, with this immediately followed by a few seconds dip in diluted H_2O_2 and H_3PO_4, which was aimed at removing surface damage caused by the ion etching. The sample was mounted on a TO-5 header for characterisation to take place. Fabrication took place at the UK EPSRC National Centre for III-V Technologies.

6.2.2 Electrical characterisation

Dark current density measurements were carried out on T2SL4 for diodes of radii of 200 and 100 µm. As the temperature is reduced from room temperature to 40 K, a dark current reduction of ~2 orders of magnitude can be observed, as shown in Figure 6.2(a). Poor agreement is found when the current is divided by area (shown in Figure 6.2(b)) and by perimeter (shown in Figure 6.2(c)). This suggests the presence of high surface leakage and bulk currents. This high surface leakage prevents the true dark current of T2SL4 from being realised.

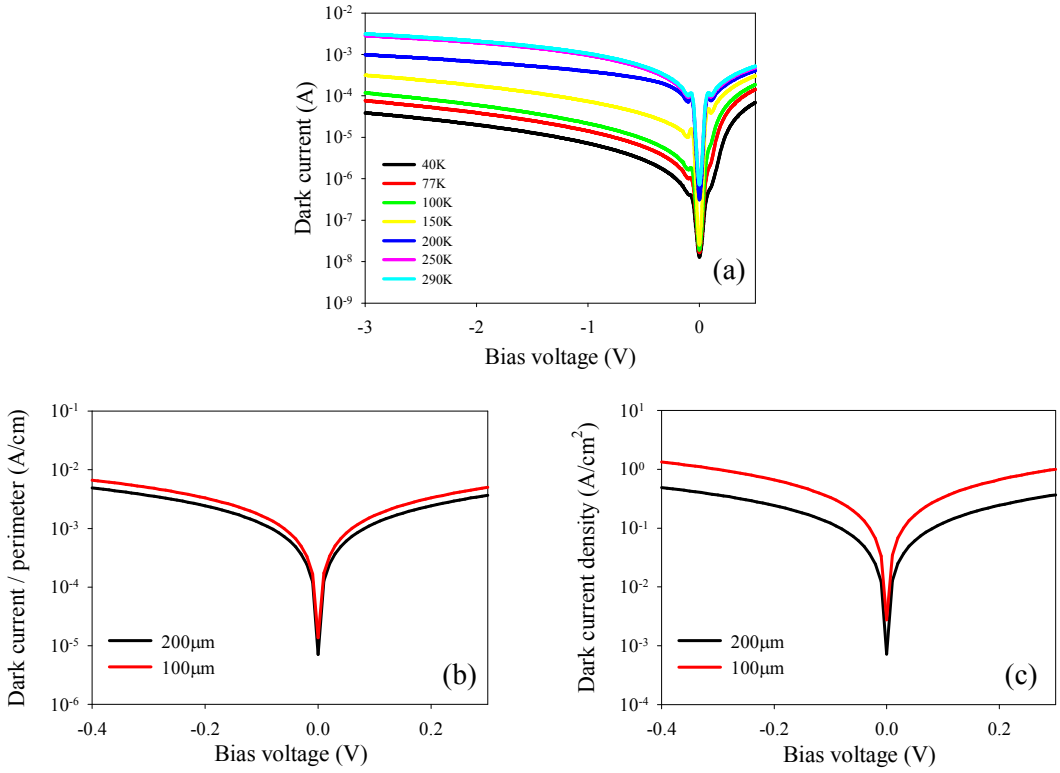

Figure 6.2 – (a) Dark current for 200 µm diode with temperature, (b) dark current density and (c) perimeter normalised dark current of T2SL4 with area at room temperature

6.2.3 Optical characterisation

Temperature dependent spectral response measurements were performed on T2SL4. Figure 6.3 shows normalised spectral response for 0 V operation.

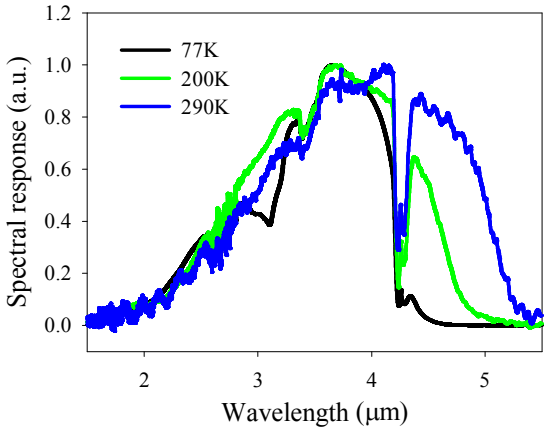

Figure 6.3 – Normalised spectral response with temperature for T2SL4 at 0 V

The peak detection wavelength of T2SL4 is ~3.7 μm at 77 K, with its cut-off wavelength, defined to be 50 % of the peak wavelength, at ~4.2 μm. This cut-off increases to ~ 4.5 and 5 μm at 200 K and room temperature, respectively. Similar to the cut-off wavelength with temperature for T2SL1, a change in band overlap is responsible for the increase in cut-off wavelength with increased temperature. Also observed in the spectra are the absorption features corresponding to CO_2 and H_2O, as were seen with the T2SL1 spectral response in Figure 5.5.

Photocurrent measurements were performed on T2SL4 using T_{BB} = 1000 ^{o}C, with the signal chopped at a frequency of ~810 Hz. Figure 6.4 shows the bias and wavelength dependence of the responsivity calculated from the photocurrent and spectral response.

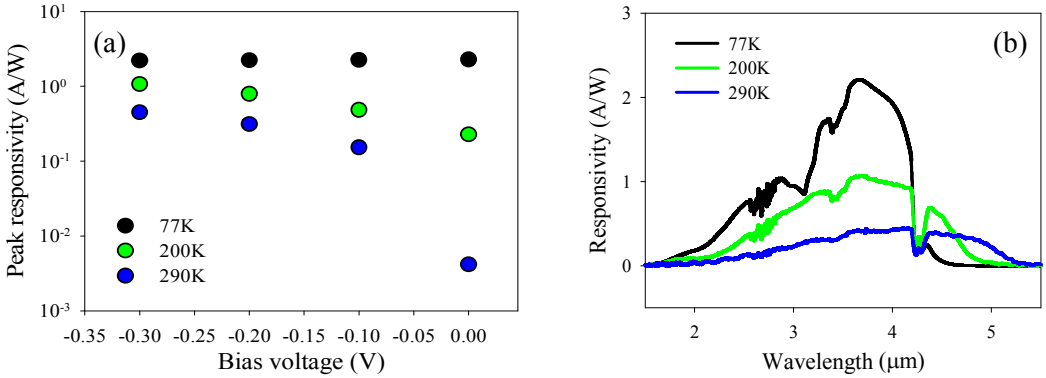

Figure 6.4 – (a) Peak responsivity with bias voltage and temperature and (b) responsivity with wavelength and temperature for T2SL4

At room temperature, a rapid increase in the peak responsivity is found with bias voltage increase from 0 to -0.3 V, although further bias voltage increase to beyond -0.3 V did not yield significant further increase in responsivity. This lower bias voltage increase in peak responsivity is less pronounced at 200 K and becomes virtually bias independent at 77 K. At -0.3 V, peak responsivities of 0.45, 1.07 and 2.21 A/W were measured at 290, 200 and 77 K, respectively. A plausible reason for the observed trend in the bias dependence of the responsivity with temperature is explored further in section 6.2.4.

Thermal noise was calculated for T2SL4 from the dark current and was used to calculate thermal noise limited D* as shown in Figure 6.5. At 77 K, an average D* of 1.6×10^{11} cmHz$^{1/2}$/W is observed at 0 V, the D* then decreases with bias voltage due to increased dark current. D* reduces as the temperature increases, by as much as an order of magnitude between 77 and 200 K. A smaller reduction is seen between 200 and 290 K. At room temperature, D* starts off low at a bias voltage of 0 V before rising to a maximum value of 8.0×10^{8} cmHz$^{1/2}$/W at -0.3 V. This increase in D* at higher temperature indicates that the dark current is increasing at a greater rate than the photocurrent with bias voltage increase, whilst at lower temperature the opposite is true.

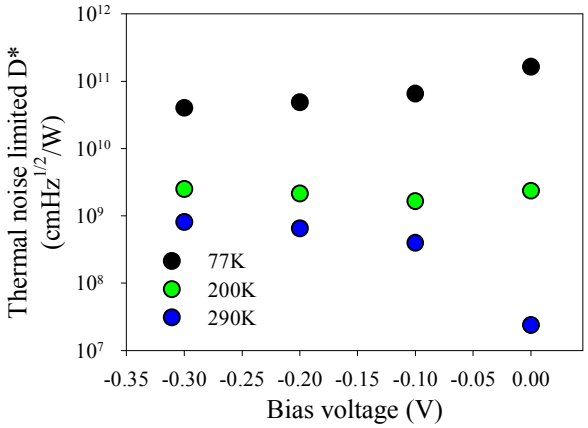

Figure 6.5 – Thermal noise limited D* with bias voltage and temperature for T2SL4

6.2.4 Analysis and comparison with T2SLs on GaSb substrate

T2SL1 and T2SL4 are similar in structure, with the only differences being their slightly different SL period and substrate material. Critically, both structures were grown with undoped absorption regions in order to maximise the depletion within their structures. In section 5.2, T2SL1 was shown to have a small depletion region which was only weakly dependent on temperature and bias voltage. Unfortunately, due to the high dark current of T2SL4, it is not possible to perform a CV measurement to analyse its depletion width. Therefore, other approaches will be used in this analysis to compare it with T2SL1.

As well as maximising the depletion region width, low absorption region doping is required in order to minimise the dark current. Figure 6.6 shows a comparison between the room temperature dark current density of T2SL1 and T2SL4. Although both detectors were grown with undoped absorption regions, they produced vastly different dark currents in terms of magnitude, as well as in the symmetry displayed about 0 V. This cannot be explained by the small differences in the superlattice period. A possible reason for this discrepancy could be differences in the unintentional background doping. To test this hypothesis, the dark current density of T2SL2 and T2SL3 are also compared in Figure 6.6 at room temperature. In section 5.2.2, along with T2SL1, it was found that increased absorption region doping lead

to increased dark current density. For this analysis, medium area diodes were used for T2SL1, T2SL2 and T2SL3, and a 200 µm radius diode was used for T2SL4.

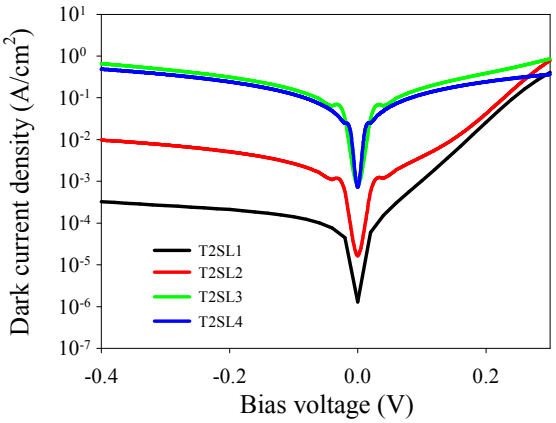

Figure 6.6 – Dark current density for T2SL1, T2SL2, T2SL3 and T2SL4 at room temperature

Similar dark current characteristics are observed in T2SL3 and T2SL4, supporting the hypothesis that T2SL4 has higher unintentional background doping. Unfortunately there is no reliable characterisation method to verify this accurately.

A further comparison of T2SL1 and T2SL4 was performed by analysing their responsivity and D*. Figure 6.7 shows a comparison of the 0 V peak responsivity and thermal noise limited D* between T2SL1 and T2SL4 as a function of temperature.

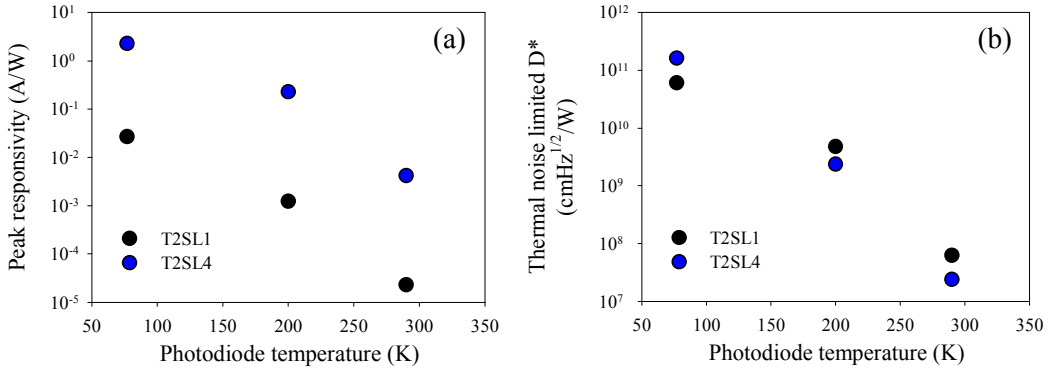

Figure 6.7 – (a) Peak responsivity and (b) thermal noise limited D* for T2SL1 and T2SL4 with temperature at 0 V

The peak responsivity of T2SL4 is larger than that of T2SL1 across the temperature range at 0 V. However, the D* is very similar at the equivalent temperatures. The trend of increased responsivity and D* with cooling is also common to both detectors, with ~3-4 orders of magnitude improvement in 0 V D* with cooling from room temperature down to 77 K.

When the bias dependence of responsivity is compared, T2SL4 shows ~107 times increase in responsivity as the bias increases from 0 to -0.3 V, in contrast to the negligible change observed in T2SL1. Their bias dependent peak responsivity and thermal noise D* at room temperature are compared in Figure 6.8. Clearly T2SL4 has a strong bias dependence. The reason for this strong bias dependence is not known at present. A plausible explanation may be the presence of photoconductive gain. The large increase in responsivity may be due to a combination of increase in carrier lifetime (possibly due to saturation of the traps at higher current levels) and reduced carrier transit time (due to increased carrier velocity at higher bias).

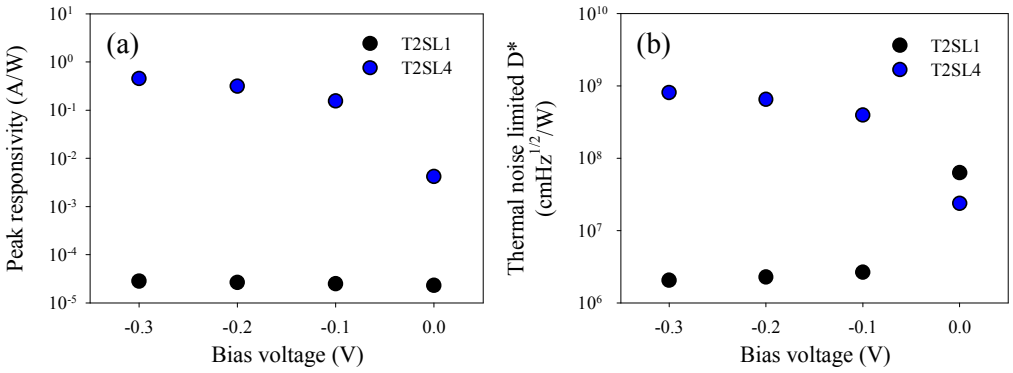

Figure 6.8 – (a) Peak responsivity and (b) thermal noise D* for T2SL1 and T2SL4 with bias voltage at room temperature

Figure 6.9(a) shows the peak responsivty for T2SL4 at room temperature for reverse and forward bias. Photocurrent, and therefore peak responsivity, for T2SL4 is fairly symmetrical about 0 V for reverse and forward bias. The large increase in responsivity in both reverse and forward bias is consistent with photoconductive gain. In contrast, the responsivity of T2SL1 drops rapidly in the forward bias as the depletion region reduces.

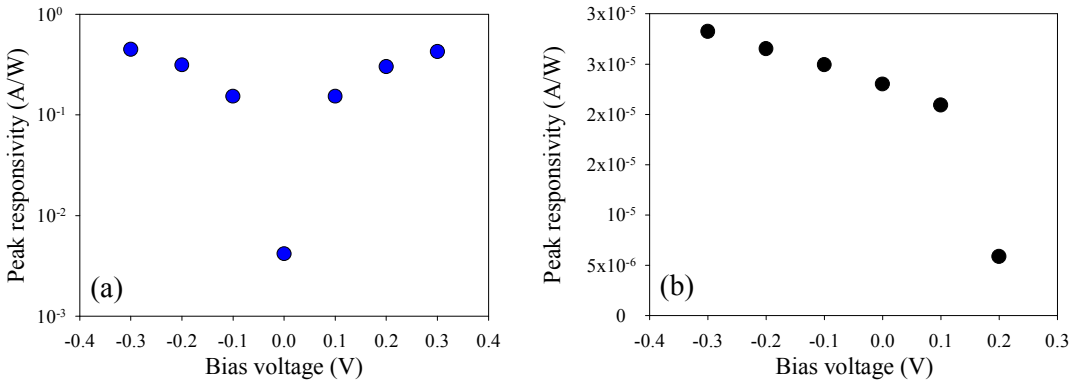

Figure 6.9 – Peak responsivity with reverse and forward bias voltage at room temperature for (a) T2SL4 and (b) T2SL1

At low temperature, some of the dopants are not activated. It is proposed that as the temperature decreases, the doping in T2SL4 will also decrease making the photoconductive behaviour less prominent. To support this argument, the temperature dependence of responsivity for T2SL4 in forward and reverse bias is compared in Figure 6.10. The results broadly support that the photoconductive gain reduces at low temperature, leading to the reduced responsivity in the forward bias. It should also be noted that the responsivity also becomes less bias dependent with decreasing temperature, again suggesting reduced photoconductive gain at low temperature.

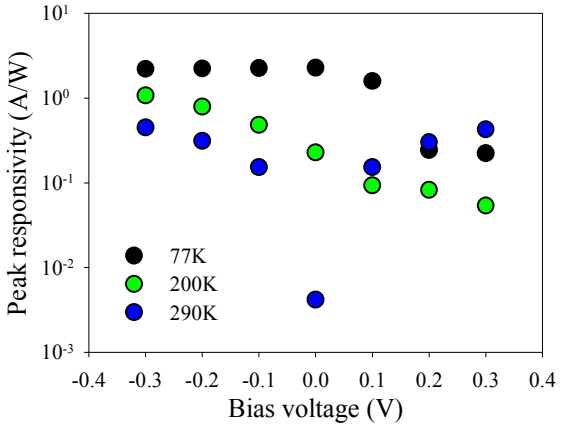

Figure 6.10 – Peak responsivity with reverse and forward bias voltage with temperature for T2SL4

These results suggest that T2SL4 has a higher level of absorption region doping than originally intended, which leads to suspected photoconductive gain and increased responsivity. This implies that there is still work to be done to control the absorption region doping of T2SLs. However, this photoconductive nature of T2SL4 is interesting and should be investigated further in other T2SL structures.

6.2.5 Radiation thermometry measurements

Variable temperature blackbody radiation thermometry measurements were carried out on T2SL4 at room temperature with a bias voltage of 0 V. Mean photocurrent and SNR with T_{BB} are shown in Figure 6.11 for a 200 µm radius diode in comparison with T2SL1.

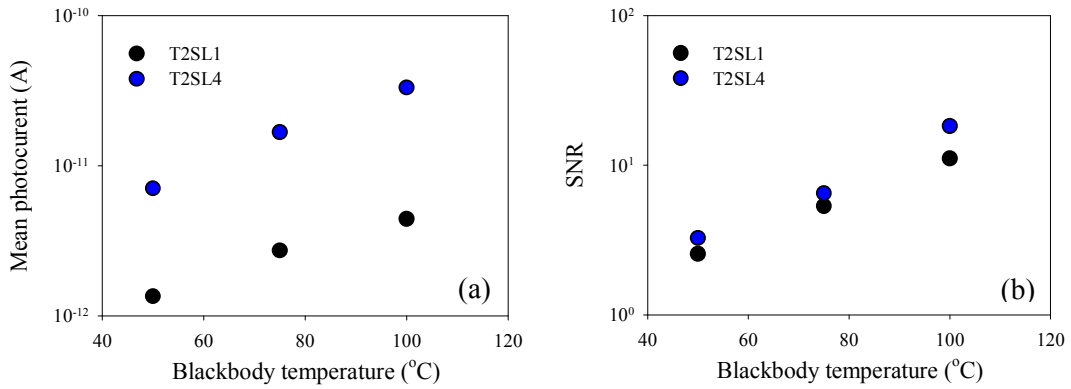

Figure 6.11 – (a) Mean photocurrent and (b) SNR with T_{BB} for T2SL1 and T2SL4 at room temperature and 0 V

Taking the same T_{BB} = 50 °C reference point analysed in Chapter 5, T2SL4 achieved a SNR of ~3.3. This is higher than for T2SL1, ~2.6, and it was accompanied by a higher mean photocurrent since its responsivity is higher. In fact, both the mean photocurrent and SNR are higher for T2SL4 across the whole T_{BB} range. However, this photocurrent difference is not as great as the difference in the peak responsivity at 0 V suggests it should be. For instance, the peak responsivity of T2SL4 is ~183 times larger than for T2SL1. By taking into account that the area of T2SL4 is ~8 times smaller than T2SL1, the photocurrent for T2SL4 would be expected to be ~23 times larger than for T2SL1. However, these results show that this difference is only

~5 times, indicating that there is something else occurring that is not accounted for. For T_{BB} = 50 ^{o}C, the blackbody emission corresponds to the longer wavelengths, which are away from the peak responsivity. As T2SL1's spectral response extends to longer wavelengths than T2SL4, due to its increased SLS period, these wavelengths will also contribute to the photocurrent. This is believed to be the reason, along with the reduced detector area, why the photocurrents are more similar than expected.

These results suggest that T2SL4 offers slightly better performance than T2SL1. However, the area of the T2SL4 detector is ~8 times smaller than that of the T2SL1 detector. The spot size of the focused blackbody signal in this unoptimised lens system was estimated to be ~2.5 mm in diameter, which is larger than the area of both T2SL1 and T2SL4, by ~5 and ~39 times respectively. A comparison between diodes of equal area would provide a more accurate comparison, with T2SL4's performance expected to improve. Also, for optimum performance of either T2SL in a practical radiation thermometer, the lens system needs to be optimised. For the current measurement setup, T2SL4's improved performance is believed to be due to its higher responsivity. However, this may ultimately only be beneficial if the noise from the dark current of the detector is much less than the amplifier noise.

To relate this to practical radiation thermometry measurements, the temperature error was calculated for T2SL4 with T_{BB}, and compared with that of T2SL1, as shown in Figure 6.12.

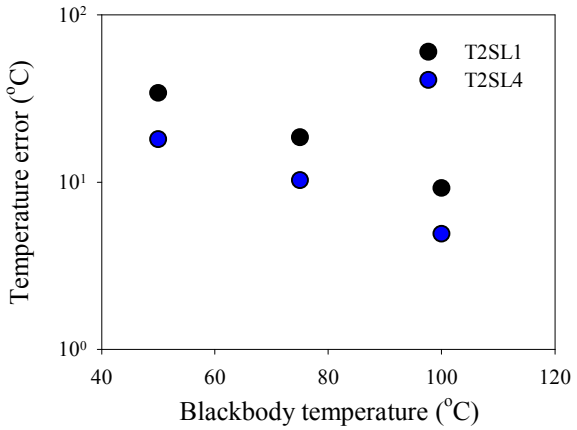

Figure 6.12 – Temperature error with T_{BB} for T2SL1 and T2SL4 at room temperature and 0 V

The temperature error of T2SL4 is below that of T2SL1 across the T_{BB} range, and is consistent with the SNR results. At T_{BB} = 50 °C, the temperature error for T2SL4 was found to be ±18 °C, compared to that of ±34 °C for T2SL1. This is indeed an improvement, but is still a fairly large temperature error. However, the strong temperature dependence of T2SL4 would be expected to lead to a reduced temperature error if it were to be cooled, as was the case for T2SL1. Additionally, the increased responsivity of T2SL4 would be expected to lead to better performance than T2SL1, again provided that the noise from the detector's dark current is less than the amplifier noise. Good performance would be expected for T2SL4 at thermo-electric cooler compatible temperatures.

With T2SL4 believed to be exhibiting photoconductive behaviour, radiation thermometry measurements were carried out with bias voltage up to -0.3 V to analyse its performance in photoconductive mode. Figure 6.13 shows the (a) mean photocurrent and (b) SNR with bias voltage and T_{BB} at room temperature.

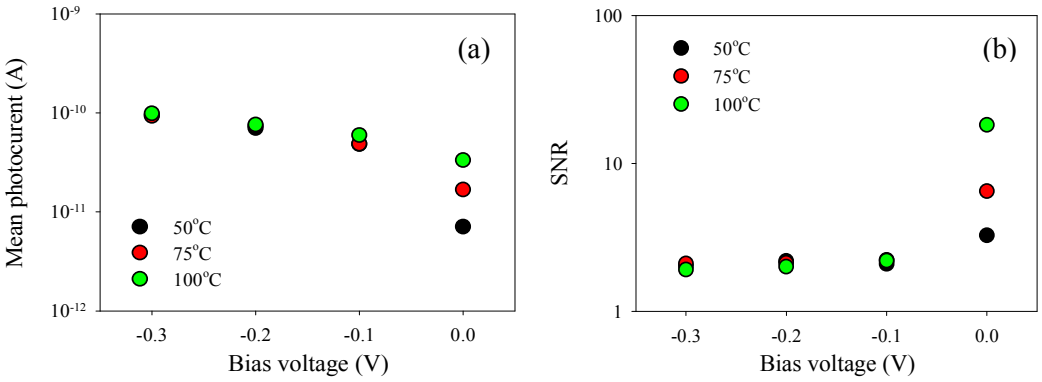

Figure 6.13 – (a) Mean photocurrent and (b) SNR with bias voltage and T_{BB} for T2SL4 at room temperature

Figure 6.13(a) shows that as the bias voltage increases, the photocurrent also increases. However, this increase in photocurrent with bias voltage is not as great as the responsivity trend measured at the higher T_{BB} of 1000 °C shown in Figure 6.8. The results suggest that the photoconductive gain is also dependent on photocurrent level. This may be related to the amount of traps that are filled at different levels of photocurrent. Figure 6.13(b) confirms that dark current increases at a faster rate than the responsivity as the bias increases, leading to reduced SNR at higher bias. This is also confirmed by the larger temperature error at high bias shown in Figure 6.14. Therefore the presence of photoconductive gain does not provide advantages in measurement of these low temperatures.

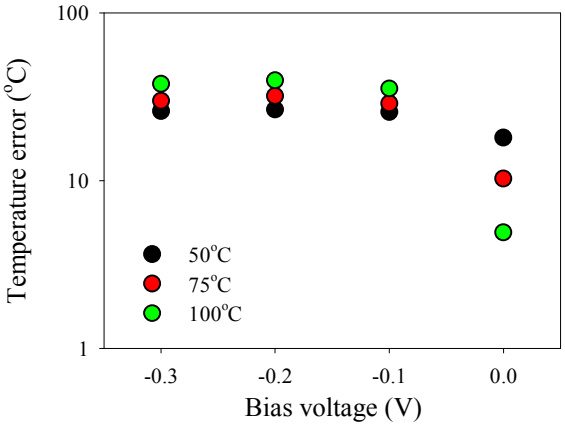

Figure 6.14 – Temperature error with bias voltage and T_{BB} for T2SL4 at room temperature

These results serve as a demonstration of an uncooled T2SL grown on a GaAs substrate for radiation thermometry. These results again highlight the challenges with T2SL growth in order to optimise the detectors for use in radiation thermometry, with the aim of maximising their responsivity and D* at room temperature. Once improved and optimised growth of T2SL material, on either GaSb or GaAs substrates, is fully realised, it would be possible to optimise their performance for specific radiation thermometry applications by demonstrating controlled tunability in their spectral response.

6.3 Conclusion

An uncooled MWIR InAs/GaAs T2SL, grown upon a GaAs substrate, was characterised and demonstrated for radiation thermometry, with a high uncooled D* of 8.0×10^{8} cmHz$^{1/2}$/W found at a bias voltage of -0.3 V. Cooling of T2SL4 resulted in improvement in the responsivity and D*. Although the responsivity and dark current were both higher than for T2SL1, the D* was similar at equivalent temperatures. The photocurrent of both detectors demonstrated strong temperature dependence, indicating potential issues with the T2SL material quality common to both detectors. By comparing the two detectors further, results suggested that T2SL4 contained a higher level of absorption region doping than T2SL1. This higher absorption region doping is believed to lead to T2SL4 demonstrating photoconductive gain, resulting in its increased responsivity compared to T2SL1. Further analysis of bias polarity dependence of the responsivity of the two detectors supported the photoconductor theory, as did cooling to reduce the absorption region doping of T2SL4. Further work needs to be done to fully understand the effect of doping on T2SL performance, including identifying the cause of the strong temperature dependent photocurrent mechanisms and achieving repeatable T2SL material growth. T2SL4 was demonstrated for use in radiation thermometry, demonstrating improved photocurrent, SNR and temperature error performance over T2SL1 at T_{BB} = 50 ^{o}C due to its increased responsivity. However, operation of T2SL4 in photoconductive mode did not result in any improvement in performance. This successful demonstration of a T2SL upon GaAs suggests the potential for more affordable T2SLs for radiation thermometry, particularly for the aim of developing

arrays. However, there is still work to be done to improve the T2SL growth repeatability and optimisation.

References

[1] M. J. Hobbs, F. Bastiman, C. H. Tan, J. P. R. David, S. Krishna, and E. Plis, "Uncooled MWIR InAs/GaSb type-II superlattice grown on a GaAs substrate," *Proc. SPIE 8899, Emerging Technologies in Security and Defence; and Quantum Security II; and Unmanned Sensor Systems X,* p. 889906, 2013.

Chapter 7 – Quantum dot infrared photodetector and infrared algorithmic spectrometer as versatile ratio radiation thermometer

7.1 Introduction

Chapter 5 and Chapter 6 introduced the mid-wave infrared (MWIR) InAs/GaSb T2SL as a viable technology for longer wavelength radiation thermometry measurements. The potential growth of two T2SL structures on top of each other, each with different detection wavelengths, leads to the potential to develop multi-colour detectors for ratio radiation thermometry. Their wavelength tunability offers versatility, an aspect which allows them to be tuned for specific measurement applications. However, these detection wavelengths need to be defined during the growth of the detectors, and cannot be adjusted when the thermometer is in use. In contrast, quantum dot infrared photodetectors (QDIPs) offer bias tunability which is highly attractive for ratio radiation thermometers. By using a QDIP in combination with an infrared algorithmic spectrometer (IRAS), there is the potential to develop a versatile ratio radiation thermometer with a tunable wavelength response.

This chapter presents a QDIP-IRAS combination for use as a ratio radiation thermometer. A QDIP is electrically and optically characterised, with evaluation of the QDIP's temperature dependence. The QDIP-IRAS is demonstrated as a ratio radiation thermometer by reproducing two arbitrary filter shapes from measured photocurrent at different T_{BB}. These reproductions were used to calculate photocurrents corresponding to each filter, with ratios computed from these photocurrents used to determine T_{BB}. Further analysis involving altering the filter properties was carried out. Finally, the QDIP-IRAS with a gauze blocking part of the FOV was used to further demonstrate this combination as a ratio radiation thermometer.

7.2 Characterisation of QDIP with temperature

7.2.1 QDIP structure

A QDIP was grown on a semi-insulating GaAs substrate. Its structure consists of 30 stacks of dot-in-a-well (DWELL) grown between two 0.5 μm Si doped n^+ GaAs regions. The DWELL consists of an undoped QD layer grown using 2.4 ML of InAs. The QDs were grown inside an $In_{0.15}Ga_{0.85}As$ well, which consists of 10 Å below and above the dots. This well was grown inside a GaAs well; 40 Å below, 68.5 Å above, with the DWELL regions separated by 500 Å $Al_{0.1}Ga_{0.9}As$ barriers. The QDIPs were fabricated using a chemical etchant solution of $HBr:CH_3COOH:K_2Cr_2O_7$ (in an equal ratio of 1:1:1) into 100 and 200 μm radius circular mesas and packaged onto TO-5 headers for characterisation. The samples were grown and fabricated at the EPSRC National Centre for III-V Technology at the University of Sheffield. This is the same QDIP as was demonstrated in [1], with Figure 7.1 showing the structure.

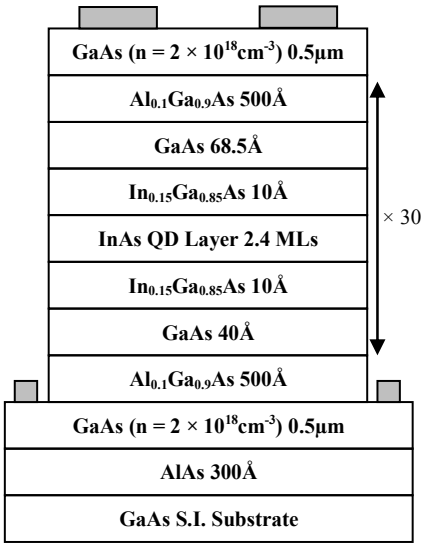

Figure 7.1 – QDIP structure

The QDIP was characterised both electrically and optically as a function of QDIP temperature to assess the ability of QDIPs to operate at high temperature.

7.2.2 Dark current

Dark current measurements were performed at 20 to 290 K. Figure 7.2 shows the dark current across the temperature range, with respect to bias voltage, for a 200 µm radius QDIP. Note, all the characterisation measurements for the QDIP were performed on 200 µm radius detectors.

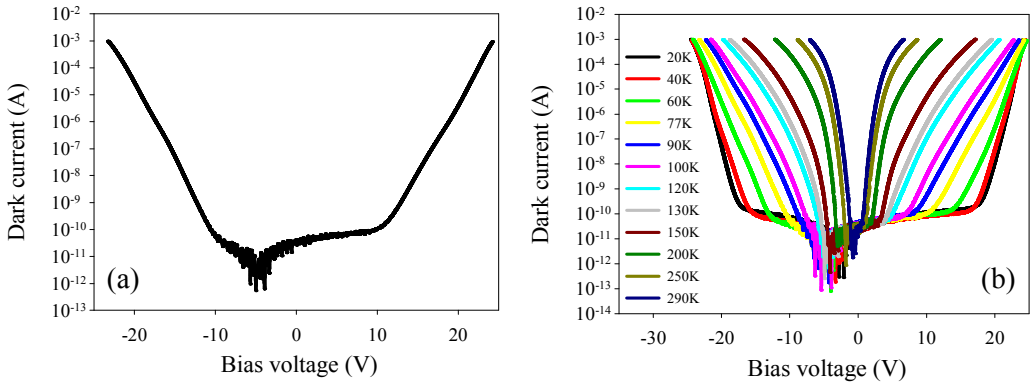

Figure 7.2 – QDIP dark current (a) at 77 K and (b) with temperature

Increased bias voltage results in increased dark current. At 77 K, there is a small increase in dark current with bias voltage as the voltage increased from 0 V. However, a rapid increase in dark current with further bias voltage increase occurs above ±10 V. As the bias voltage increases, the electric field increases. This causes the bands to tilt, reducing the thickness of the barrier. Once the barrier becomes thin enough, electrons can tunnel through and form part of the dark current [2].

Cooling of the QDIP results in decreased dark current. However, at the lowest temperatures of 20 and 40 K, the dark current's temperature dependence reduces. It is assumed that the dark current is dominated by dot-to-dot or dot-to-well tunnelling rather than thermionic emission at these temperatures. In contrast, at higher temperatures, the greater temperature dependence of the dark current indicates that the dark current is dominated by thermionic emission.

7.2.3 Spectral response

Spectral response measurements were performed on the QDIP at 77 K, with bias dependence of the spectra shown in Figure 7.3.

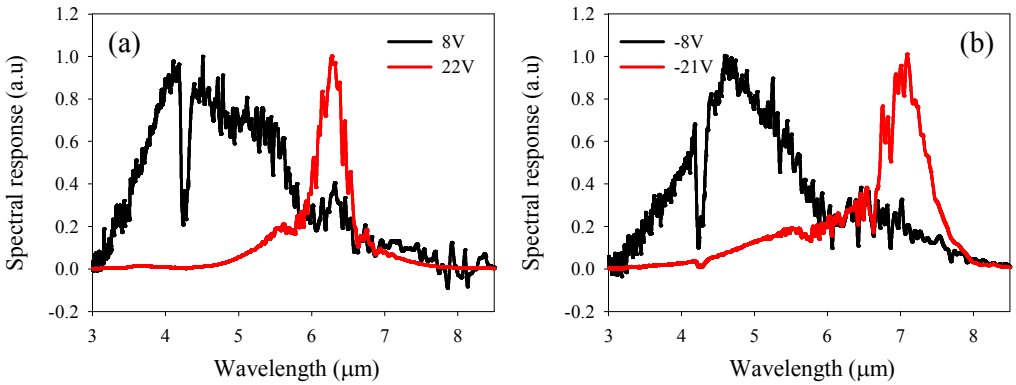

Figure 7.3 – Spectral response for QDIP at 77 K for (a) positive bias and (b) negative bias

Distinct spectral peaks could be measured at four different peak wavelengths corresponding to different bias voltages, as shown in Figure 7.3. This highlights the QDIP's highly tunable bias dependent spectral response. The peaks in Figure 7.3(a) correspond to positive bias, whilst the peaks in Figure 7.3(b) correspond to negative bias. The longer wavelength peaks correspond to the greatest applied bias for either polarity. These longer wavelength peaks correspond to the transition between the ground state and the higher excited states, whereas the shorter wavelength peaks correspond to the direct transition from the ground state to the continuum level.

The longer wavelength peaks have greater variation than the shorter wavelength peaks. For example, this varies between 6 and 7 μm, depending on the QDIP's bias polarity. The wavelength shift is dependent on the position of the QDs within the GaAs wells. For the QDIP, the QDs are off centre within the structure; band tilting under different bias polarity therefore leads to different transitions that produce different spectral responses. The shorter wavelength peaks are less dependent upon the bias polarity, due to less variation in the transitions under band tilting. This highly tunable spectral response makes the QDIP ideally suited for use with the IRAS for development of a versatile ratio radiation thermometer.

The spectral response demonstrated little temperature dependence, indicating no major change in the energy transitions. Although the bandgap of the constitute

materials will increase as temperature reduces, these results suggest that the QDIP intersubband transitions are unaffected; these are dependent upon the size and positions of the QD and the QW within the structure. However, no spectral response could be measured above 100 K, although, as will be shown in section 7.2.4, a photocurrent could be successfully measured. This suggests that the increased dark current is preventing the FTIR from measuring the spectra; the photocurrent cannot be distinguished above the noise floor.

7.2.4 Photocurrent and responsivity

Photocurrent measurements were performed on the QDIP using T_{BB} = 800 ^{o}C, with the signal chopped at 810 Hz. Figure 7.4(a) shows QDIP photocurrent from 40 to 290 K, with Figure 7.4(b) showing the peak responsivity.

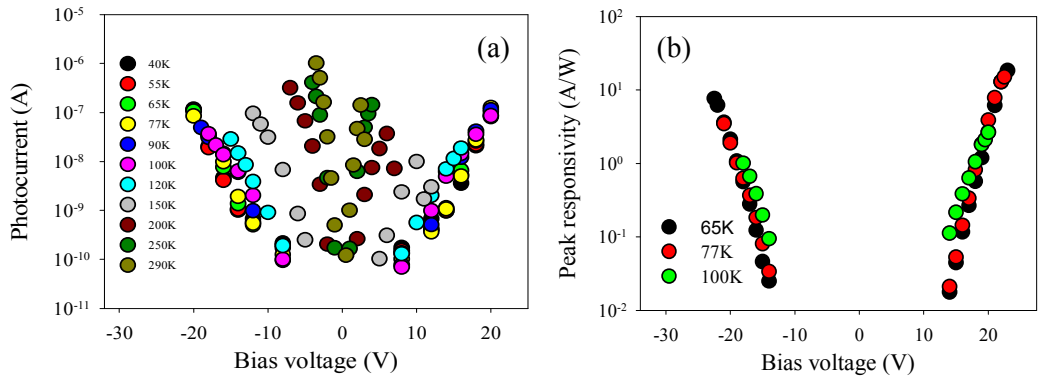

Figure 7.4 – (a) Photocurrent and (b) peak responsivity with bias voltage for QDIP

The QDIP's photocurrent demonstrates a strong temperature dependence as it was cooled from room temperature down to 100 K. However, further cooling shows reduced temperature dependence. Below 100 K, the peak responsivity demonstrates a similar lack of temperature dependence. At fixed bias voltages, the peak responsivity increases with temperature increase. However, lower temperature operation allows higher bias voltages to be used, due to the reduced dark current. At these higher bias voltages, higher peak responsivities were measured at lower temperatures. Peak responsivities of 18.31, 14.97 and 2.64 A/W were measured at temperatures of 65, 77 and 100 K, respectively. Such high responsivity is indicative of photoconductive gain within the QDIP.

This reduction in photocurrent as temperature decreases is believed to be due to a reduction in the photoconductive gain caused by reduced carrier mobility. However, reduced temperature dependence of the photocurrent at the lowest temperatures suggests that the carrier mobility is no longer decreasing. The responsivity follows this trend at lower temperature, but the lack of spectral response prevented the measurement of responsivity at higher temperature.

The responsivity as a function of wavelength is shown in Figure 7.5 for the QDIP at 77 K. This highlights that the responsivity is at its greatest at higher bias voltages, corresponding to the longer wavelength peaks at ~6 and 7 μm, Figure 7.5(a). This is due to the increased photocurrent provided by both the QDIP's photoconductive gain and increased tunnelling at the high bias voltage.

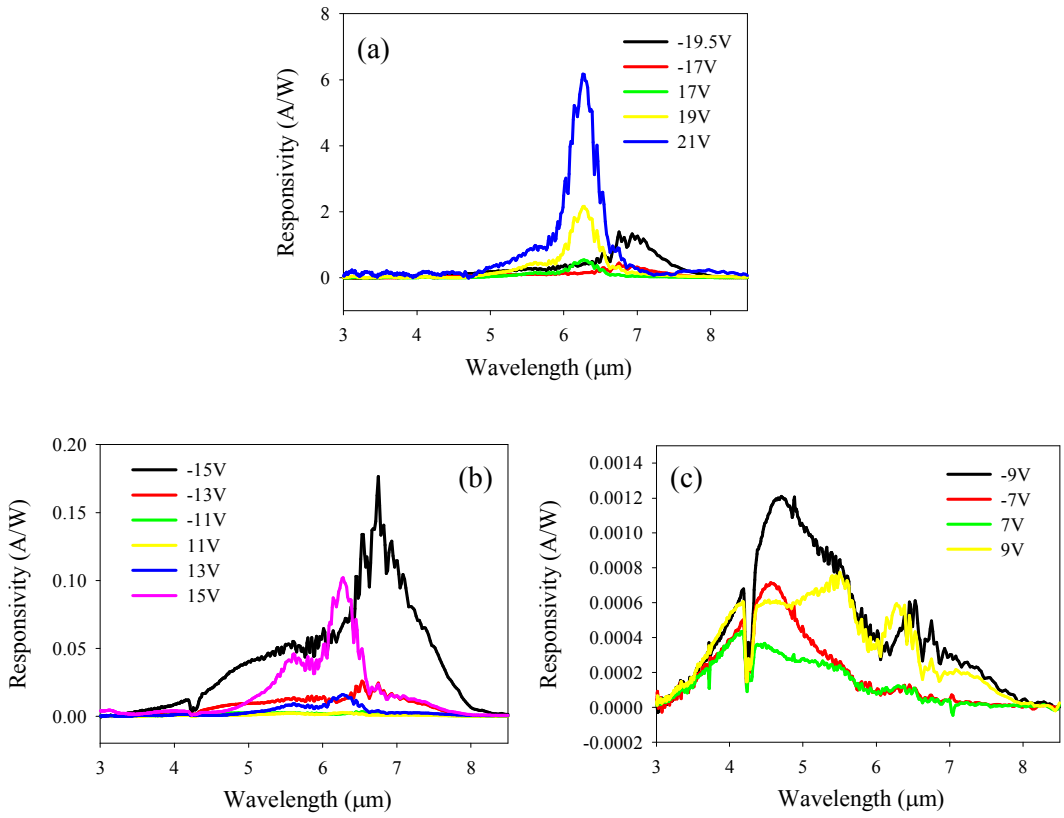

Figure 7.5 – Responsivity with wavelength for QDIP at 77 K

7.2.5 Noise

Noise measurements for the QDIP are shown in Figure 7.6 at 65, 77 and 100 K. The noise increases with bias voltage and temperature, but a noise floor of ~5×10^{-13} A/Hz$^{1/2}$ prevents further measurement at low bias voltages. This increase in noise with bias voltage and temperature follows that of the dark current; there is an increase in both the thermal noise and the g-r noise. This noise floor is due to the measurement setup, with the main contribution coming from the pre-amplifier. With the input of the pre-amplifier grounded, this noise floor of ~5×10^{-13} A/Hz$^{1/2}$ was measured, confirming the limit presented by the measurement system.

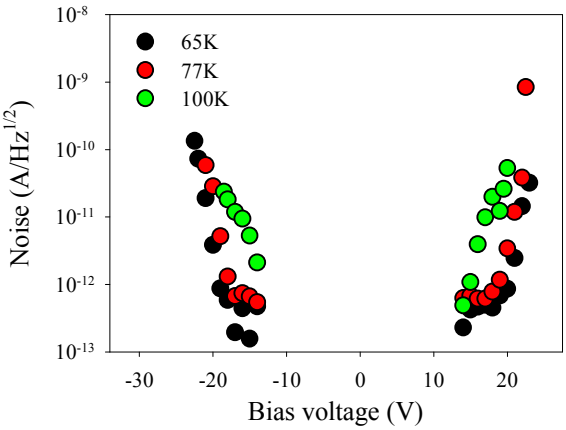

Figure 7.6 – Noise for QDIP

7.2.6 D*

The measured peak responsivity and noise were combined to calculate D* for the QDIP. The temperature and bias voltage dependence of this D* is shown in Figure 7.7.

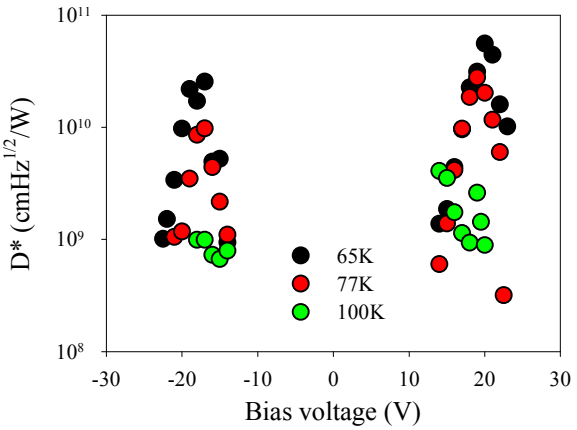

Figure 7.7 – D* for QDIP with temperature and bias voltage

The D* has a strong temperature dependence between 65 to 100 K. Peak values of D* of 5.6×10^{10}, 2.8×10^{10} and 4.1×10^{9} cmHz$^{1/2}$/W were measured at 65, 77 and 100 K, respectively. These correspond to bias voltages of 20, 19 and 14 V, respectively. As the responsivity and noise decrease with cooling, there is a corresponding increase in D*. With D* proportional to the ratio between the responsivity and noise, the increase in D* with cooling suggests that the noise is decreasing at a greater rate than the responsivity.

It should be noted that the peak D* was measured in the middle of the measured bias range for each polarity and temperature. As bias voltage increases, both the responsivity and noise increase, until a point where the D* is at its maximum. This indicates that the responsivity increases at a greater rate than the noise. However, after the point at which the peak D* reaches its maximum value, the D* starts to drop again. Both the responsivity and noise continue to increase, but this drop in D* suggests that the increase in noise is now increasing at a greater rate than the responsivity. For the bias voltages immediately below the peak D* bias voltage, the measurement of the D* is limited by the noise floor of the measurement setup. If the noise floor of the setup could be reduced, it could be possible to measure a lower noise, and therefore a more accurate D* value at these bias voltages.

The temperature dependence of the peak D* of the QDIP is shown in Figure 7.8.

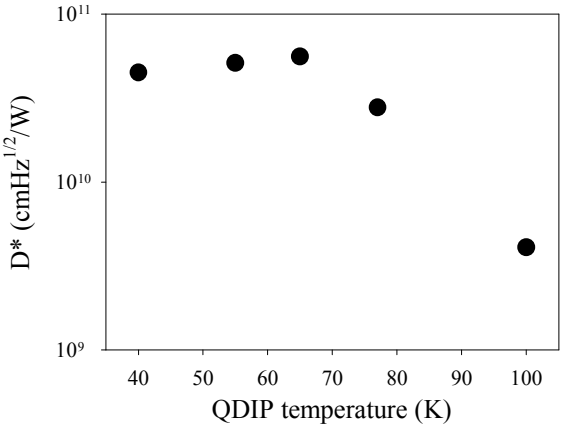

Figure 7.8 – Peak D* for QDIP with QDIP temperature

As temperature reduces from 100 to 65 K, the peak D* increases. However, below 65 K, the peak D* starts to level off. As the temperature drops below 65 K, the peak responsivity demonstrates weak temperature dependence due to reduced photoconductive gain. This therefore results in the levelling off in the peak D* observed in Figure 7.8. This suggests that cooling the QDIP below 65 K offers no benefit to its performance. This trend has been observed by other authors [3][4]. Additionally, if the temperature were to be increased beyond 100 K, and if a spectral response could be measured, the rapid decrease in peak D* with temperature suggests that the D* would be poor at these temperatures. Although good performance is observed at these cryogenic temperatures, further investigation is required to improve QDIP performance with the aim of higher temperature operation. One potential area of investigation to increase the QDIP operating temperature is the growth of smaller QDs. This will lead to both reduced dark current and increased carrier lifetime, resulting in higher temperature operation.

7.3 QDIP-IRAS as ratio radiation thermometer

A demonstration of the QDIP-IRAS combination for ratio radiation thermometry follows in this section.

7.3.1 Evaluation of QDIP-IRAS using real filter shapes

Photocurrent measurements were performed on a 200 µm radius QDIP at 77 K for T_{BB} = 100-800 ºC at 100 ºC intervals, as shown in Figure 7.9. 15 bias voltages were used for this initial analysis, taken across the QDIP's spectral range. These bias voltages were: -19.5, -17, -15, -13, -11, -9, -7, 7, 9, 11, 13, 15, 17, 19 and 21 V. Below 7 V, it was not possible to measure the spectral response of the QDIP. The photocurrent reduces with reduction in T_{BB}, however a noise floor prevents measurement of photocurrent below ~20 pA. It is believed that this noise floor is limited by the measurement setup used including the pre-amplifier and spectrum analyser.

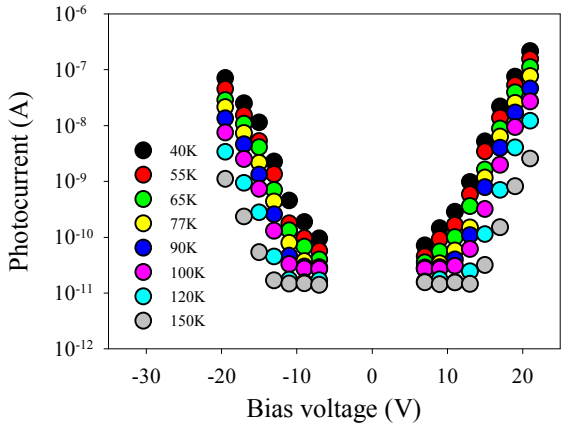

Figure 7.9 – Measured photocurrent for QDIP at 77 K with T_{BB} = 100-800 ^{o}C

Section 2.5 outlined the full procedure for implementing the IRAS, but the key equations will be reproduced here. Matrix $\boldsymbol{A}$, equation (7.1), can be formed for each T_{BB} using responsivities calculated from these photocurrents.

$$\boldsymbol{A} = \begin{bmatrix} R_{V1}(\lambda_1) & R_{V2}(\lambda_1) & \cdots & R_{VN}(\lambda_1) \\ R_{V1}(\lambda_2) & R_{V2}(\lambda_2) & \cdots & R_{VN}(\lambda_2) \\ \vdots & \vdots & \vdots & \vdots \\ R_1(\lambda_L) & R_2(\lambda_L) & \cdots & R_{VN}(\lambda_L) \end{bmatrix} \tag{7.1}$$

Reproductions of the SWF and LWF filters, corresponding to transmission wavelengths of 3.17–5.0 and 5.0–7.0 µm, can be calculated using the IRAS. The

arbitrary filters are represented by $\boldsymbol{R}$, equation (7.2), with the reproduced filters represented by $\boldsymbol{R_{rep}}$, equation (7.3). The weights, $\boldsymbol{w}$, calculated using $\boldsymbol{A}$ and $\boldsymbol{R}$, are calculated using equation (7.4).

$$\boldsymbol{R} = \begin{bmatrix} R(\lambda_1) \\ R(\lambda_2) \\ \vdots \\ R(\lambda_L) \end{bmatrix} \tag{7.2}$$

$$\boldsymbol{R_{rep}} = \sum_{i=1}^{N} w_{V_i} R_{V_i}, \tag{7.3}$$

$$\boldsymbol{w} = (\boldsymbol{A}^T\boldsymbol{A} + \boldsymbol{\Phi})^{-1}\boldsymbol{A}^T\boldsymbol{R} \tag{7.4}$$

Figure 7.10 shows these reproductions at (a) T_{BB} = 800 and (b) T_{BB} = 100 °C.

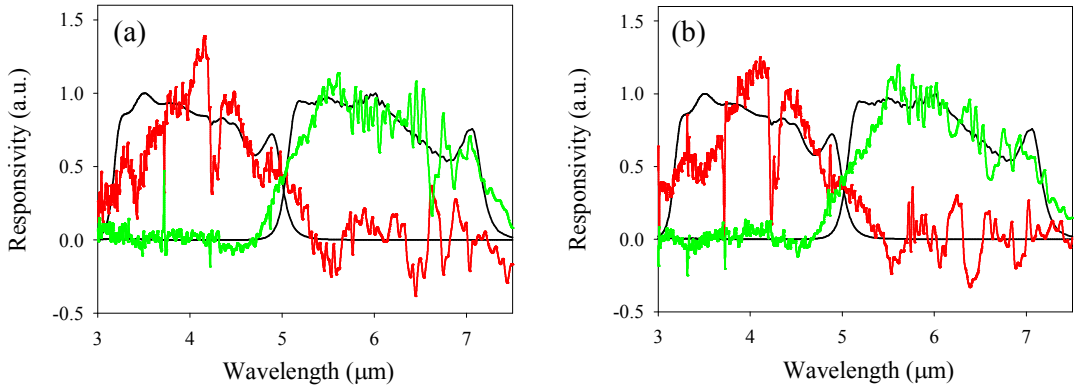

Figure 7.10 – Reproduced filters at (a) T_{BB} = 800 °C and (b) T_{BB} = 100 °C

Acceptable reproduction of the filters is demonstrated. The quality of the reproduction is due to the acceptably high responsivity of the QDIP. The weak temperature dependence of the filter reproduction is not surprising; it relies mostly upon the spectral response shape of the QDIP. However, the source of error in the reproduction is believed to be insufficient variation of the spectral shapes of the QDIP and unoptimised weighting factors and combination of selected spectral shapes in the IRAS. These filters are very different in shape compared with the

QDIP spectral response. *Vines* [5] discussed that the use of triangular filters leads to improved filter reproduction, due to the shape of triangular filters being similar to the QDIP spectral response.

To assess the quality of the filters reproduced using the IRAS, the total signal within each filter was computed for T_{BB} = 100-800 ^{o}C. From this, the ratio of optical power between the two filters was obtained. The procedures were repeated to give computed ratios using the target filter, i.e. the arbitrarily defined filter. Figure 7.11 shows these ratios, along with the measured ratio using an optical power meter described in section 2.5.

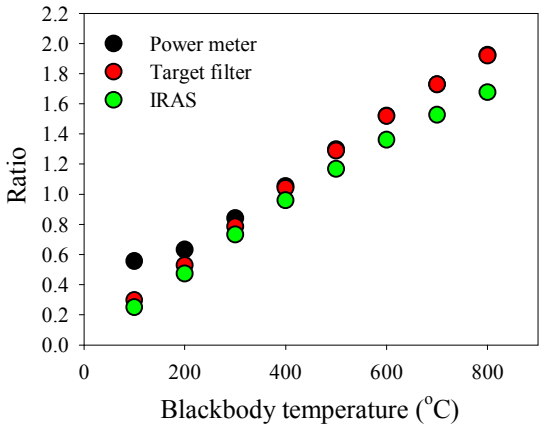

Figure 7.11 – Ratios of optical power between the filters from measured power, computed ratio using target filters and computed ratio using IRAS

Reasonable agreement between ratios using the target filter and IRAS is observed, although there is room for improvement at high T_{BB}. The non-perfect reproduction of the filters using the IRAS has lead to discrepancy between the computed ratios using the IRAS and the target filter. There is also some discrepancy between the computed ratio using the target filter and the measured ratio. This is believed to be due to atmospheric absorption during the measurement. However, a much larger deviation is seen at lower T_{BB}. As was explained in section 2.5, this is due to the power meter's inability to measure the lower blackbody emitted power with sufficient accuracy.

In order to improve the performance of the IRAS, there are aspects which can be investigated and analysed. Optimisation of the target filter shape to best match the QDIP response in order to improve the quality of the filter reproduction. Reduction of the filter width to make it easier for the QDIP-IRAS to target grey areas in the emitted spectrum of surfaces. Reduction in the number of bias voltages used in the IRAS with optimised choice of bias voltage for each filter, with the aim of improved filter reproduction. These aspects will be investigated in the next three sections.

7.3.2 Evaluation of QDIP-IRAS using triangular filter shapes

As was shown and discussed by *Vines* [5], triangular filters offer improved filter reproduction with the IRAS. This is due to the QDIP's intrinsic spectral response being more triangular in shape rather than the shape of rectangular or Gaussian filters. Therefore, triangular filters also offer improved shape comparison when compared with the filters used in the above analysis. Additionally, the position of the centre wavelength of the filters helps with filter reproduction. Filters centred at the QDIP's peak response make use of the spectral range of greatest responsivity.

Further analysis of the QDIP-IRAS was carried out using triangular filters with widths of 2 μm. The filters had centre frequencies of 5 and 7 μm representing the SWF and LSF, respectively. These filters are shown in Figure 7.12.

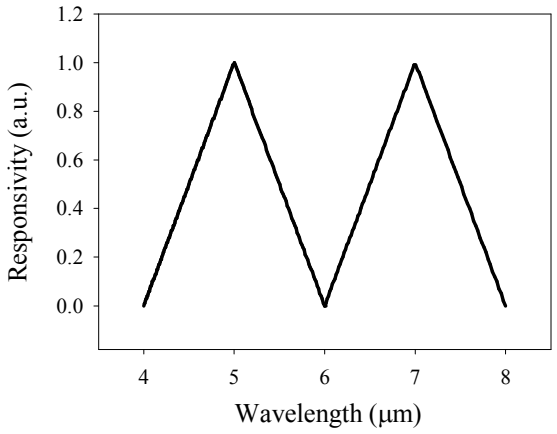

Figure 7.12 – Triangular filters used for QDIP-IRAS

The IRAS was used with these filters to produce reproductions of the triangular filters at T_{BB} = 100-800 ^{o}C. Figure 7.13 shows these reproductions at (a) T_{BB} = 800 and (b) T_{BB} = 100 ^{o}C.

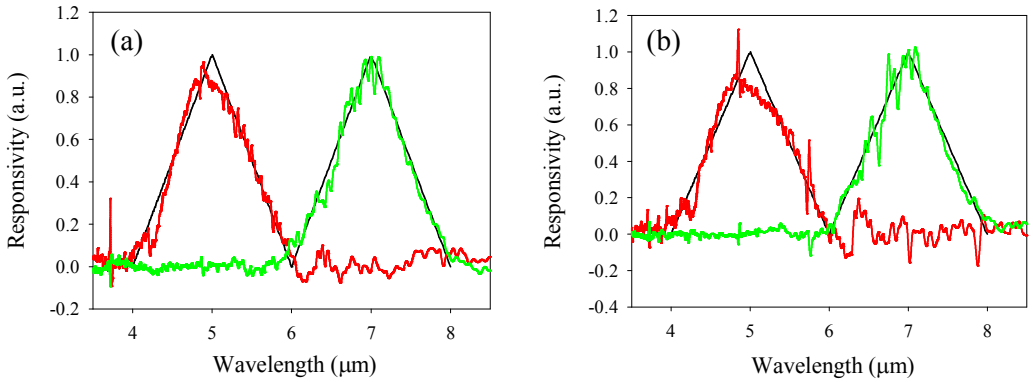

Figure 7.13 – Reproduced triangular filters at (a) T_{BB} = 800 ^{o}C and (b) T_{BB} = 100 ^{o}C

The reproduction of these triangular filters is significantly better than that of the real filters, with reproduction again down to T_{BB} = 100 ^{o}C. The shape and wavelength of the QDIP spectra are therefore better suited to these triangular filters. Photocurrents and ratios computed using the target triangular filter and IRAS were calculated, with Figure 7.14 showing a comparison between the ratios computed using the target triangular filters and the IRAS.

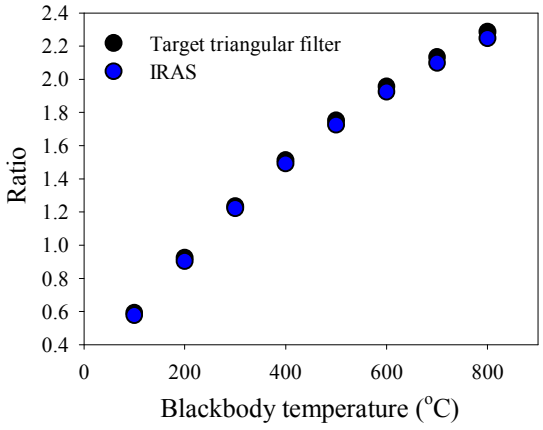

Figure 7.14 – Ratios computed using target triangular filters and IRAS

The ratios computed using the target triangular filters and the IRAS show better comparison with each other than those computed using the target real filters demonstrated in section 7.3.1. This indicates that the triangular filters are more suitable for the QDIP-IRAS for a ratio radiation thermometer. This also demonstrates the flexibility of the IRAS such that it is not bound by the properties of physical filters. By defining arbitrary filters within the IRAS this way, it allows greater control over the filter wavelengths for the ratio radiation thermometry measurement.

7.3.3 Evaluation of QDIP-IRAS using narrower filter shapes

In practical ratio radiation thermometers, narrow band responses are preferred which limit the wavelength range of detection. This is required in order to make it easier to target the grey areas in the radiated emission of the target object. The filters demonstrated so far in this analysis are relatively large and therefore undesirable for such systems. Use of narrower triangular filters are therefore demonstrated and analysed in this section.

Reproduction of narrower triangular filters can be investigated by scaling the triangular filters by factors of 0.5, 0.25, 0.125 and 0.05. These correspond to filter widths of 1, 0.5, 0.25 and 0.1 μm, respectively. Figure 7.15 shows reproduction of these filters for T_{BB} = 800 ^{o}C.

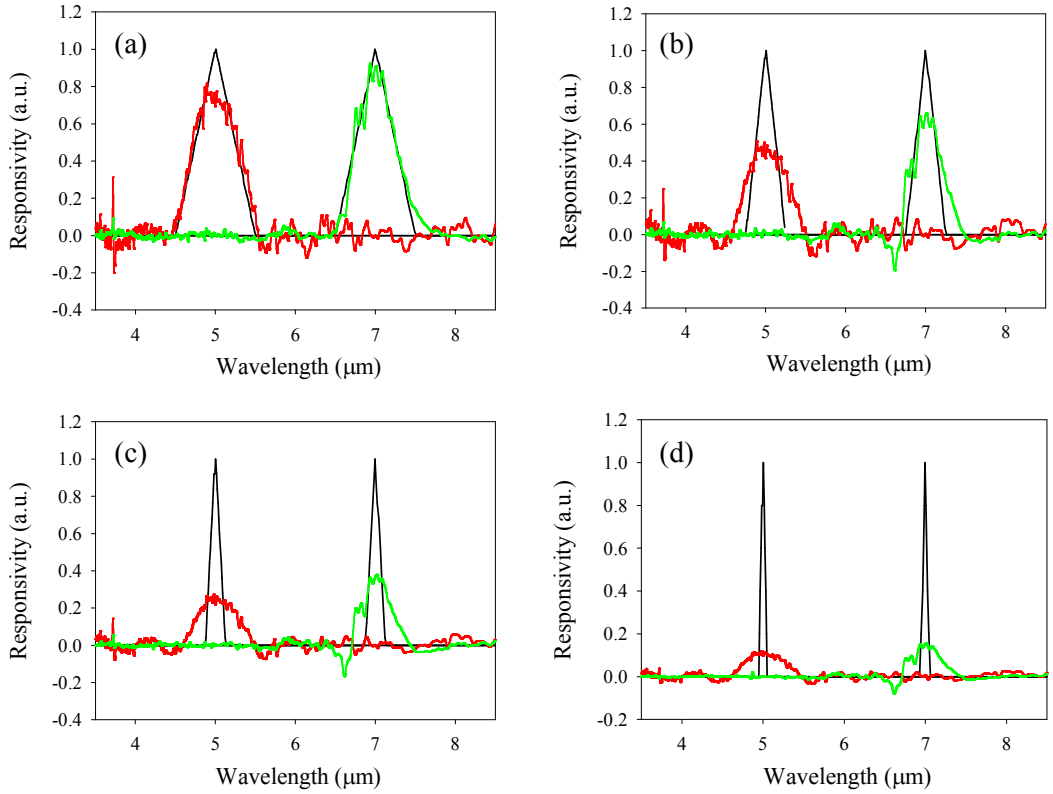

Figure 7.15 – Reproduction of triangular filters at T_{BB} = 800 ^{o}C with filter widths of (a) 1, (b) 0.5, (c) 0.25 and (d) 0.1 μm

The quality of the filter reproduction deteriorates as the filter width reduces, with filter widths down to ~1 μm achieving the best filter reproduction. This is understandable, due to the width of the QDIP spectra being similar to 1 μm. In order for narrower filters to be reproduced, a QDIP with a narrower spectral response is required. Ratios computed from the target triangular filters and the IRAS for T_{BB} = 800 ^{o}C are shown in Figure 7.16(a) as a function of filter width. Figure 7.16(b) shows the absolute error between the ratios. This absolute error is defined by equation (7.5).

$$Absolute\ error = \left|\frac{Ratio_{Target} - Ratio_{IRAS}}{Ratio_{Target}}\right| \qquad (7.5)$$

$Ratio_{Target}$ is the ratio computed from the target triangular filters, with $Ratio_{IRAS}$ the ratio computed from the IRAS.

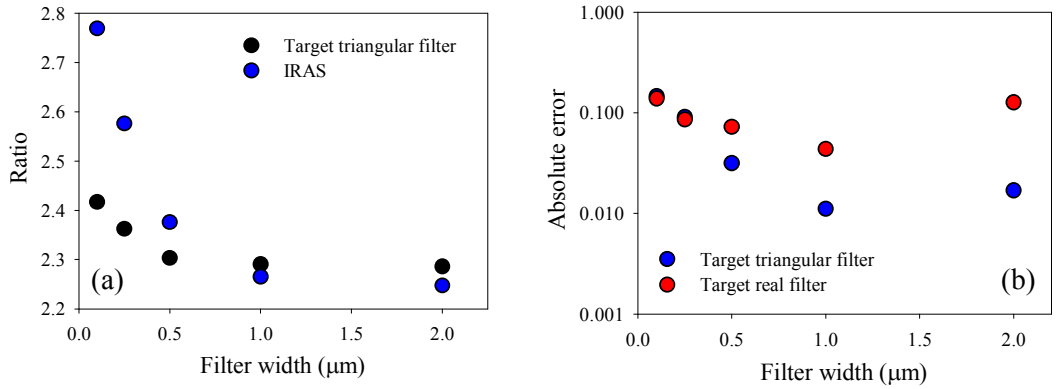

Figure 7.16 – (a) Ratios computed using IRAS and target triangular filters with filter width at T_{BB} = 800 °C and (b) absolute error between computed ratios for target triangular filters and target real filters

As expected, the ~1 μm filters resulted in the lowest absolute error between computed ratios. Increase in absolute error as the filters get narrower is a result of the poorer filter reproduction. Also included in Figure 7.16(b) is a similar analysis, but this time using versions of the real filters scaled to the equivalent widths of the triangular filters. Again, these results demonstrate that filter widths down to ~1 μm produce the best results, but with a higher absolute error than the triangular filters for larger filter widths. This will therefore correlate to reduced error in the measured T_{BB}. As the filter width reduces to less than the width of the QDIP spectra, the absolute error becomes similar for both filter shapes, leading to poor reproduction.

7.3.4 Evaluation of QDIP-IRAS using reduced and optimised bias voltages

The implementation of the IRAS has so far been demonstrated with spectral shapes corresponding to 15 bias voltages. However, these same spectral shapes were used for reproduction of both the SWF and the LWF. This is not an ideal scenario; the spectral shapes do not all have strong responsivity for both the SWF and the LWF due to their strong bias voltage dependence. A better option is to select bias voltages corresponding to spectral shapes specific for reproduction of the SWF and LWF

individually. Therefore, each filter will be reproduced using just the spectral shapes which the detector will have the strongest spectral response within the wavelength range of that filter. Naturally, the bias voltages used for each filter reproduction will be different. Figure 7.17 shows the normalised spectral response with bias voltage for both the (a) positive and (b) negative bias polarities for the QDIP.

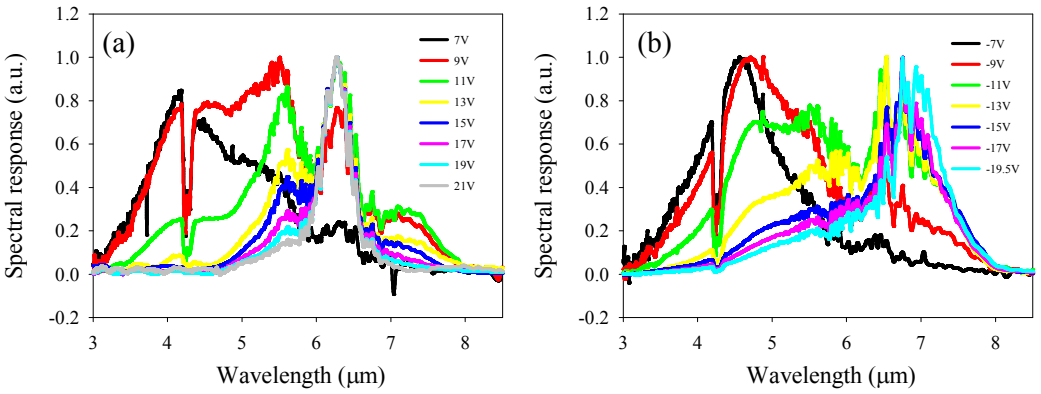

Figure 7.17 – Normalised spectral of QDIP for (a) positive and (b) negative bias polarity

By observation of the spectral response, it is clear that the lower bias voltage spectral shapes in either bias polarity are the most appropriate for the SWF, with the larger bias voltage spectral shapes the most appropriate for the LWF. Due to the large number of potential bias voltage combinations, it was not possible to demonstrate the IRAS with all possible bias combinations. Therefore, manual observation of the spectral shapes was used to deduce the appropriate bias voltage combinations for both the SWF and the LWF. However, *Jang et al.* [6] have performed a more exhaustive search into number and choice of bias voltages used for the IRAS.

Figure 7.18 shows the reproduction of 2 μm triangular filters using spectral shapes corresponding to the SWF and the LWF. These reproductions use (a) 2, (b) 4 and (c) 6 bias voltages for each filter. Appendix I lists the bias voltages used for each filter reproduction. It should be stressed that these combinations are not optimised but are included to demonstrate the effect of spectral shape selection.

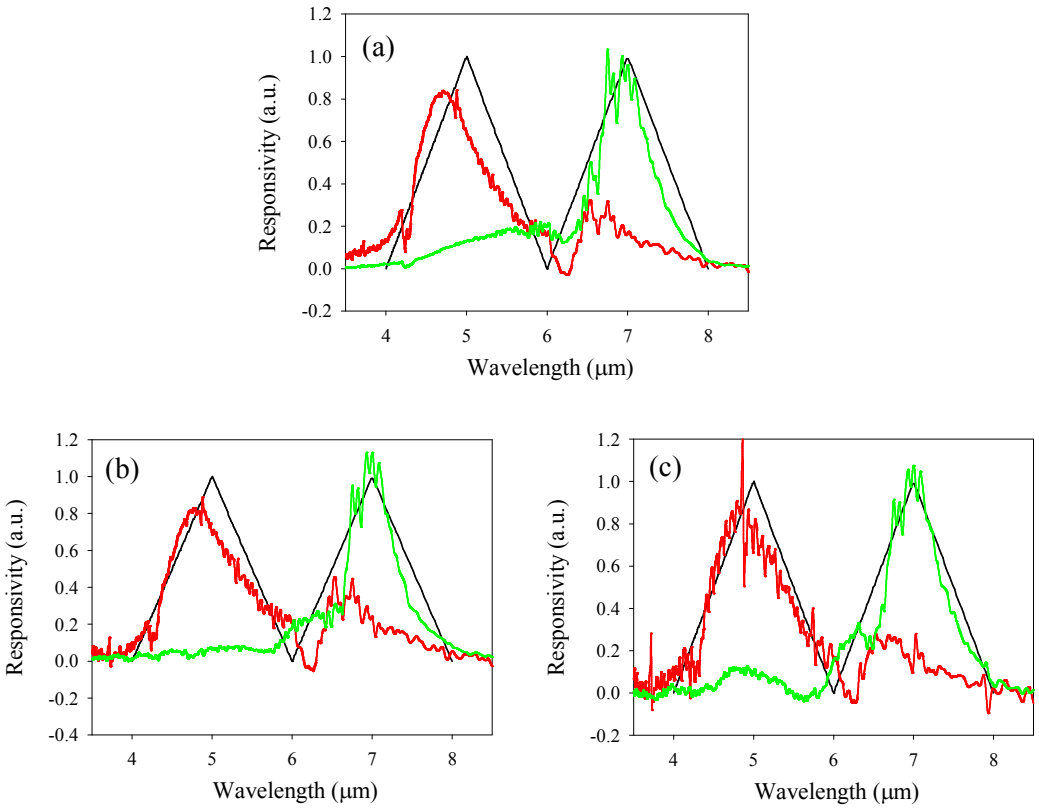

Figure 7.18 – Reproduction of triangular filters at T_{BB} = 800 °C with separate bias voltages specified for the SWF and LWF using (a) 2, (b) 4 and (c) 6 bias voltages for each filter

When using 2 bias voltages, the reproduction of the LWF and SWF are reasonable. As the number of bias voltages increases, the quality of the SWF reproduction increases slightly, whilst that of the LWF does not increase as much. The reasonable reproduction of the LWF with only 2 bias voltages is believed to be due to the QDIP's strong responsivity at longer wavelengths. The lower responsivity of the QDIP at shorter wavelengths leads to the corresponding error in the SWF reproduction. Therefore, more bias voltages or different combinations are required for improved reproduction of the SWF, whilst not for the LWF.

Ratios were computed from the target triangular filters and the IRAS, with Figure 7.19 showing the absolute error between the ratios as a function of bias voltage. Also included is the absolute error when using the original 15 bias voltages.

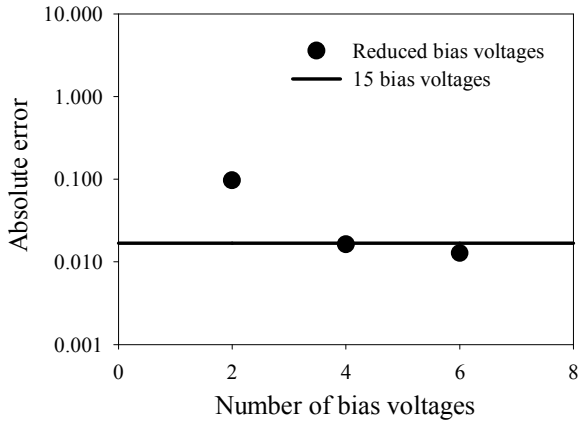

Figure 7.19 – Absolute error between computed ratios for target triangular filters and target real filters with varied number of bias voltages

As the number of bias voltages used in the reproduction increases, the absolute error reduces. As the number of bias voltages increases to 4 and beyond, the absolute error drops below that of the original 15 bias voltages reproduction. These results are not surprising, as it shows that improved performance of the IRAS is achieved by using more bias voltages. However, it is clear also that the use of fewer bias voltages, using spectral shapes suitable for reproduction of the SWF and LWF individually, can demonstrate the same performance or better than using the original 15 bias voltages for both the SWF and the LWF.

7.3.5 Evaluation of QDIP-IRAS using gauze

Ratio radiation thermometers are used for temperature measurement scenarios where the FOV is partially obscured. Therefore, in order to demonstrate this principle, photocurrent measurements were carried out at 77 K for T_{BB} = 600, 700 and 800 ^{o}C with a metal gauze placed between the blackbody source and the QDIP. The gauze blocked ~50 % of the blackbody signal, and hence provided a partially obscured FOV.

Once again, matrix $\boldsymbol{A}$ for each T_{BB} was calculated using responsivities calculated from the measured photocurrent. Using the IRAS and 2 μm triangular filters, triangular filter reproductions were produced for each T_{BB}, using the original 15 bias voltages. Figure 7.20(a) shows this reproduction for T_{BB} = 600 ^{o}C.

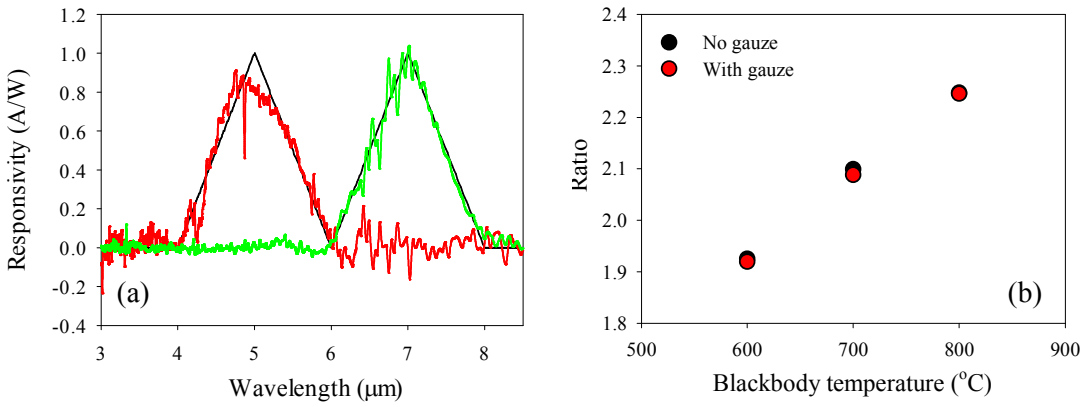

Figure 7.20 – (a) Reproduced filters for T_{BB} = 600 °C with gauze and (b) ratios computed with and without gauze

Again, good reproduction of the triangular filters was achieved. The high responsivity of the QDIP still resulted in a large photocurrent despite the reduced signal. Photocurrents and computed ratios using the target triangular filters and IRAS were calculated, with Figure 7.20(b) comparing these ratios with measurements taken without the gauze. These ratios compare very well with and without the gauze. This therefore successfully demonstrated the use of the QDIP-IRAS as a ratio radiation thermometer with a partially obscured FOV.

7.4 Conclusion

A QDIP-IRAS combination was demonstrated as a versatile longer wavelength ratio radiation thermometer. At 77 K, the QDIP-IRAS demonstrated reasonable reproduction of filter shapes based on real bandpass filters for T_{BB} = 100-800 °C. Computed ratios using the IRAS compared reasonably with ratios computed using the target filters. However, the filter reproductions and computed ratios greatly improved with the use of triangular filters. Reduction in the filter width to 1 μm produced the best filter reproductions and the lowest absolute error for the computed ratios using the IRAS compared with target triangular filters. By optimising the choice of bias voltages for the SWF and LWF individually, fewer bias voltages were required for the IRAS to result in the same level of absolute error as the original unoptimised 15 bias voltages. Finally, successful reproduction of triangular filters and ratios at T_{BB} = 600-800 °C with a gauze placed in front of the blackbody was

also achieved, therefore demonstrating the ratio radiation thermometry principle with an obscured FOV. Although further investigation and developments are required, the QDIP-IRAS combination has been demonstrated as a versatile longer wavelength ratio radiation thermometer.

References

[1] C. H. Tan, P. Vines, M. Hobbs, B. Anderson, M. Hugues, and J. David, Implementation of an algorithmic spectrometer using Quantum Dot Infrared Photodetectors," *Infrared Physics & Technology,* vol. 54, pp. 228-232, 2011.

[2] V. Ryzhii, "The theory of quantum-dot infrared phototransistors," *Semiconductor science and technology,* vol. 11, pp. 759-765, 1996.

[3] H. Lim, S. Tsao, W. Zhang, and M. Razeghi, "High-performance InAs quantum-dot infrared photodetectors grown on InP substrate operating at room temperature," *Applied physics letters,* vol. 90, p. 131112, 2007.

[4] S. Tsao, H. Lim, H. Seo, W. Zhang, and M. Razeghi, "InP-Based Quantum-Dot Infrared Photodetectors With High Quantum Efficiency and High-Temperature Imaging," *IEEE Sensors Journal,* vol. 8, pp. 936-941, 2008.

[5] P. Vines, "Infrared Detection and Spectral Imaging Using Low Strain Quantum Dot Infrared Photodetectors," Dissertation, Department of Electronic and Electrical Engineering, University of Sheffield, Sheffield, 2010.

[6] W.-Y. Jang, M. M. Hayat, J. S. Tyo, R. S. Attaluri, T. E. Vandervelde, Y. D. Sharma*, et al.*, "Demonstration of bias-controlled algorithmic tuning of quantum dots in a well (DWELL) midIR detectors," *IEEE Journal of Quantum Electronics,* vol. 45, pp. 674-683, 2009.

Chapter 8 – Conclusions and future work

8.1 Conclusions

This work has introduced and evaluated various infrared detector technologies which have the potential to form the next generation of detectors for radiation thermometry. These technologies offer benefits over the current generation of detectors in the form of increased sensitivity, uncooled longer wavelength detection, flexible longer wavelength multi-colour detection and the potential for array implementation. This work is therefore the basis for further research and development in order to optimise these technologies for radiation thermometry, demonstrating them to their full potential.

The motivation of increased sensitivity was demonstrated in Chapter 4 by evaluating a Si APD for radiation thermometry. A lower minimum T_{BB} could be measured to satisfy a specific minimum threshold voltage for the Si APD in comparison with a Si photodiode, highlighting the potential of using the more sensitive APD for radiation thermometry. This increased sensitivity enabled measurement of a lower temperature whilst operating at a shorter wavelength, hence removing the need for a longer wavelength detector. Additional excess noise was not added to the thermometer system by using the Si APD. Instead, the Si APD was demonstrated to provide higher SNR and lower temperature error than the Si photodiode, provided that the correct level of gain was used. These benefits applied to both PSD and DD operation of the Si APD, although the use of PSD was shown to measure lower T_{BB} than DD, as well as offering improvement in the SNR and temperature error. The best performance was demonstrated by using the Si APD in combination with PSD, offering significant improvement over the Si photodiode using DD. This work has shown that the more sensitive Si APD is a viable detector technology for radiation thermometry. Its increased sensitivity also provides scope for the Si APD to be demonstrated for longer range radiation thermometry as well as higher speed measurements.

Chapter 5 explored the development of suitable detectors for use in minimally cooled MWIR arrays for radiation thermometry. A MWIR InAs/GaSb T2SL was evaluated

for radiation thermometry; a technology which also has the capability of being developed into longer wavelength multi-colour detectors for ratio radiation thermometry. The uncooled T2SL detector with the nominally undoped absorption region was demonstrated for radiation thermometry, with detection of T_{BB} = 25 ^{o}C with SNR > 1. Cooling of the T2SL demonstrated improvement in both the SNR and temperature error, arising from increased photocurrent and decreased dark current. The measurement of T_{BB} = 50 ^{o}C with a temperature error of ±0.5 ^{o}C could be achieved by cooling the T2SL to 175 K. However, if a temperature error of ±1 ^{o}C were to be deemed satisfactory, this could be achieved by cooling the T2SL to 200 K, and this would therefore be compatible with thermo-electric cooling. The strong temperature dependence of the T2SL indicates that further work needs to be done to fully investigate its causes in order to optimise T2SL for room temperature operation.

Development of the MWIR InAs/GaSb T2SL was taken further in Chapter 6 by evaluating a detector grown on a GaAs substrate for radiation thermometry, with the aim of developing more affordable T2SLs for radiation thermometry arrays. The T2SL showed a high uncooled D* of 8.0×10^{8} cmHz$^{1/2}$/W at a bias voltage of -0.3 V. However, cooling the T2SL resulted in similar photocurrent temperature dependence to the undoped T2SL on GaSb, indicating a temperature dependent mechanism common to both detectors. Therefore, this highlighted potential issues with the quality of T2SL material growth. Further comparison of the two detectors suggested that the T2SL on GaAs contained a higher level of absorption region doping than the T2SL on GaSb, corresponding to its higher dark current and peak responsivity. It was suggested that this higher absorption region doping leads to photoconductive gain, which corresponds to the increased peak responsivity measured with bias voltage increase. Further analysis of the bias polarity dependence of the responsivity of the two detectors gave support to this photoconductor theory, as did cooling to reduce the absorption region doping for the T2SL on GaAs. When evaluated for radiation thermometry at T_{BB} = 50 ^{o}C, the T2SL on GaAs demonstrated improved performance over the T2SL on GaSb due to its higher responsivity. However, operation of the T2SL on GaAs in photoconductive mode did not result in any improvement in performance. The comparison and analysis of the T2SLs on both GaAs and GaSb suggest that it is not the growth of T2SL on GaAs which is the

major challenge for T2SL development; it is the growth of the T2SL material itself regardless of the substrate.

Chapter 7 detailed the development of longer wavelength detectors for ratio radiation thermometry by demonstrating a QDIP in combination with an IRAS. This QDIP-IRAS combination allows for the development of a versatile longer wavelength ratio radiation thermometer. The approach enables the filter wavelengths to be tuned by the IRAS rather than being dictated by fixed filters. The QDIP-IRAS was demonstrated to reproduce filter shapes based on real bandpass filters for T_{BB} = 100-800 ^{o}C, with computed power ratios using the IRAS comparing reasonably well with ratios computed using the target filters. However, filter reproduction and computed ratios using the IRAS were shown to improve greatly with the use of triangular filters; the best reproduction was demonstrated with triangular filters with a width of 1 μm. By reducing the filter width in this way, it allows for minimisation of the wavelength range measured, and thus allows the thermometer to target grey areas in the emitted spectrum of surfaces. Optimisation of the bias voltages used for reproduction of the SWF and LWF individually demonstrated the same level of absolute error as the original unoptimised 15 bias voltages. The QDIP-IRAS was demonstrated with a partially obscured FOV to successfully reproduce triangular filters and ratios for T_{BB} = 600-800 ^{o}C with a gauze in front of the blackbody source. The QDIP-IRAS has therefore been demonstrated to have the potential to be developed further as a versatile ratio radiation thermometer.

8.2 Future work

This work has evaluated new detector technologies for radiation thermometry which offer potential benefits over the current detector technologies currently used in commercial radiation thermometer systems. However, there are still several areas of further investigation and improvement which needs to take place before each technology is commercially viable. In addition, there are various other ways in which these technologies could be demonstrated to offer benefits for radiation thermometry. Suggested further work is therefore covered here.

The increased sensitivity of Si APDs has been demonstrated to offer benefit to radiation thermometry in terms of measuring lower T_{BB} in comparison to a Si

photodiode. However, in order to further investigate the benefits of the Si APD, a direct comparison with a longer wavelength detector, such as an InGaAs photodiode, should be carried out. No benefit in terms of improvement in the minimum temperature measured would be expected by the Si APD, with the InGaAs photodiode capable of measuring down to 150 ^{o}C [1]. However, the most interesting analysis to perform would be a comparison of the detectors' ability to cope with target objects of unknown emissivity at temperatures which conventional Si photodiodes are unable to measure. Due to the shorter wavelength response of the Si APD, it would be expected to lead to reduced error compared with the longer wavelength InGaAs for the measurement of the same target object temperature.

The limitation of Si APDs for measurement of lower temperature target objects is the fact that its spectral range is within that of the visible light spectrum. Where this is not a problem for measurement scenarios which are completely shielded from any background signals, it leads to challenges for measurements where sufficient shielding from the background cannot be achieved. However, InGaAs APDs, which have a spectral response of 0.9-1.7 μm, do not have this problem. Therefore, it is proposed that an InGaAs APD should be explored for radiation thermometry and compared with an InGaAs photodiode. It is expected that improvement will be achieved by using the InGaAs APD compared to the simple InGaAs photodiode. Importantly, the longer wavelength InGaAs material will not be affected by background visible wavelengths, so the APD's increased sensitivity will be better utilised.

Taking the APD principle further, Geiger mode operation Si and InGaAs single photon avalanche diodes (SPADs), which have the ability to breakdown upon detection of a single photon of light, should be investigated as even more sensitive detectors for radiation thermometry. SPADs are used for applications which require detection of very weak optical signals. In radiation thermometry this translates to the potential measurement of lower temperatures. The principle of single photon radiation thermometry has been demonstrated with the use of a photomultiplier tube [2], with the target temperature related to the photon count rate. However, such investigations were mainly focused on the development of the first photoelectric detectors for radiation thermometry. SPADs for radiation thermometry have the potential to measure even lower temperatures than APDs whilst still maintaining

shorter wavelength operation. Investigations should involve identifying a relationship between the photon count rate and the target temperature, and linking these results to Planck's Law.

An uncooled MWIR InAs/GaSb T2SL was successfully demonstrated to detect T_{BB} = 25 ^{o}C. However, characterisation of the detector and evaluation of its performance for radiation thermometry highlighted areas where improvement is required, as demonstrated by its significantly improved performance with cooling. The exact reasons for this improvement are not fully understood, although it is believed that cooling of the T2SL leads to increased carrier lifetime and diffusion length due to a reduction in recombination pathways [3]. Therefore it is proposed that a full investigation into the causes of this temperature dependence takes place. Other authors have performed similar investigations into carrier lifetime within T2SLs [3][4]. Once these processes are better understood, investigations should be focused on improving the growth of T2SLs. Such investigations should aim to reduce trap defects which may be a cause of the reduced carrier lifetime at high temperature. If this is successful and optimised, it would be expected to lead to increased photocurrent and better performance at room temperature, making such detectors very attractive for radiation thermometry.

Highlighting further the challenges of MWIR InAs/GaSb T2SL growth, investigations need to take place to optimise the absorption region doping, as well as gain better control of it. In this work, two T2SLs were grown with non-intentional doping, but resulted in vastly different results. One detector behaved like a photodiode, whilst the other like a photoconductor with suspected photoconductive gain. Whilst work needs to be done to try and minimise the absorption region doping to maximise the depletion width, investigations should also take place with the aim of maximising the absorption region doping to investigate the T2SL's photoconductive behaviour further. Investigations should involve attempting to quantify the level of this photoconductive gain for T2SLs with highly doped absorption regions, and compare against T2SLs with reduced absorption region doping.

The major attraction of MWIR InAs/GaSb T2SLs is their wavelength tunability. In theory, the peak detection wavelength can be tuned to correspond with narrow

bandpass filters which are required for specific temperature measurement applications in the MWIR. Demonstration of T2SLs grown for specific applications would lead to optimised performance for each application. This would therefore demonstrate the T2SL to its full potential, and offer improved performance over a detector without an optimised spectral response.

Another big attraction of this T2SL wavelength tunability is that it can be combined with the ability to grow one detector on top of another to develop multi-colour T2SL detectors. This wavelength tunability enables a wide range of wavelength combinations to be grown, whilst growth of wider bandgap semiconductors on top of the T2SL extends this capability from the visible to the MWIR spectral regions. Such a flexible approach would be very attractive for ratio radiation thermometry.

Once the above investigations and developments have been successfully demonstrated and optimised for a single pixel, investigation into the growth of linear and 2D arrays should take place. For successful use as arrays, optimised etching and passivation techniques are required to ensure that small T2SL pixels do not suffer from surface leakage current. Once an array has been successfully demonstrated on a GaSb substrate, the next step would be to repeat this on a GaAs substrate in order to reduce the cost. The major challenge is the growth of T2SLs in general, rather than the growth on GaAs, although this is not without its challenges. Once all these developments have taken place, it should be possible to demonstrate high operating temperature single- and multi-colour T2SL arrays for radiation thermometry.

The QDIP-IRAS combination was successfully demonstrated as a ratio radiation thermometer at 77 K. Although cryogenically cooled detectors are not impossible for such applications, with some facilities having access to liquid nitrogen supplies, it is not desirable due to the added cost and size of such an approach. Therefore, efforts are required to develop QDIPs which operate above 200 K, therefore making them compatible with thermo-electric cooling. QDIPs have been reported with operating temperatures above 200 K [5][6][7], so this is indeed possible. For example, growth of smaller QDs will lead to reduced dark current, longer carrier lifetime and therefore higher temperature operation.

The IRAS was demonstrated in this work using a QDIP at 77 K. However, characterisation of the QDIP at different operating temperatures demonstrated a

strong temperature dependence, particularly in its D*. This analysis should be repeated at different operating temperatures, and therefore different D* values. This will allow an assessment of the effect of noise on the filter and ratio reproduction, as well as offering indications of the performance expected if thermo-electrically cooled QDIPs could be fully realised but with lower D*.

In order for the IRAS to reproduce narrower filters widths, QDIPs will need to be developed with a narrower spectral response, accompanied with a wider spectral shape. Growth of QDIPs with narrower spectral responses have been achieved [8][9], so this is possible. Like operating temperature, this development is essential for the QDIP-IRAS to be viable. Successful reproduction of narrower filters is required to make it easier to target grey areas in the radiated emission of target objects.

The QDIP-IRAS has been suggested and demonstrated as a versatile ratio radiation thermometer. However, its versatility should be fully demonstrated. For example, an analysis of the QDIP-IRAS's ability to compute ratios using multiple filter combinations should be carried out. An assessment of the best filter combinations should be performed, highlighting the combinations that are most suitable for implementing the IRAS in practice. Due to the wavelength dependence of the QDIP's responsivity, there are expected to be better filter combinations than others. Those combinations deemed suitable for use with the IRAS should therefore be identified. Once identified, the QDIP-IRAS should be demonstrated by measuring the temperature of target objects with a known wavelength dependent emissivity.

References

[1] H. Yoon, C. Gibson, V. Khromchenko, and G. Eppeldauer, "SSE-and noise-optimized InGaAs radiation thermometer," *International Journal of Thermophysics,* vol. 28, pp. 2076-2086, 2007.

[2] P. Coates and J. Andrews, "Measurement of thermodynamic temperatures with the NPL photon-counting pyrometer," *Temperature, Its Measurement and Control in Science and Industry,* vol. 5, pp. 109-114, 1982.

[3] B. M. Nguyen, D. Hoffman, E. K. Huang, S. Bogdanov, P. Y. Delaunay, M. Razeghi*, et al.*, "Demonstration of midinfrared type-II InAs/GaSb superlattice photodiodes grown on GaAs substrate," *Applied Physics Letters,* vol. 94, p. 223506, 2009.

[4] B. C. Connelly, G. D. Metcalfe, H. Shen, and M. Wraback, "Direct minority carrier lifetime measurements and recombination mechanisms in long-wave infrared type II superlattices using time-resolved photoluminescence," *Applied Physics Letters,* vol. 97, p. 251117, 2010.

[5] P. Bhattacharya, X. Su, S. Chakrabarti, G. Ariyawansa, and A. Perera, "Characteristics of a tunnelling quantum-dot infrared photodetector operating at room temperature," *Applied Physics Letters,* vol. 86, p. 191106, 2005.

[6] S. F. Tang, S. Y. Lin, and S. C. Lee, "Near-room-temperature operation of an InAs/GaAs quantum-dot infrared photodetector," *Applied Physics Letters,* vol. 78, p. 2428, 2001.

[7] H. Lim, S. Tsao, W. Zhang, and M. Razeghi, "High-performance InAs quantum dot infrared photodetectors grown on InP substrate operating at room temperature," *Applied physics letters,* vol. 90, p. 131112, 2007.

[8] S. Tsao, H. Lim, H. Seo, W. Zhang, and M. Razeghi, "InP-Based Quantum-Dot Infrared Photodetectors With High Quantum Efficiency and High-Temperature Imaging," *IEEE Sensors Journal,* vol. 8, pp. 936-941, 2008.

[9] H. Lim, S. Tsao, W. Zhang, and M. Razeghi, "High-performance InAs quantum-dot infrared photodetectors grown on InP substrate operating at room temperature," *Applied physics letters,* vol. 90, p. 131112, 2007.

Appendices

Appendix A: Details of detectors evaluated in thesis

Commercial detectors evaluated in thesis:

Si photodiode – Hamamatsu model S2386-45K

Si APD – Hamamatsu model S2384

Wafer numbers of detectors evaluated in thesis:

T2SL1 – L12-132

T2SL2 – L12-136

T2SL3 – L12-137

T2SL4 – R7-07

QDIP – VN1485

Appendix B: Derivation of $\%/^{o}C$ from Wien Approximation

Differentiate Wien Approximation, equation A.1 with respect to *T*, to give equation A.2.

$$L_\lambda = \frac{c_1}{\lambda^5} \exp\left(\frac{-c_2}{\lambda T}\right) \tag{A.1}$$

$$dL_\lambda = \frac{c_1 c_2}{\lambda^6 T^2} \exp\left(\frac{-c_2}{\lambda T}\right) dT \tag{A.2}$$

Divide equation A.2 by equation A.1 to give equation A.3.

$$\frac{dL_\lambda}{L_\lambda} = \frac{c_2 dT}{\lambda T^2} \tag{A.3}$$

$(dL_\lambda/L_\lambda)/dT$ gives $\%/^{o}C$, which can be expressed as in equation A.4.

$$\%/°C = 100 \times \frac{c_2}{\lambda T^2} \tag{A.4}$$

Appendix C: Operation of helium cooled cryostat

This section outlines the procedure for preparing the helium cooled cryostat for photocurrent, noise, spectral response and radiation thermometry measurements, as well as shutting it down.

1. Solder packaged detector sample to wires within the cryostat chamber, remove cap from header and screw header into contact with the cryostat cold finger using washer and screws.
2. Turn cryostat water supply on. This is required to ensure the cryostat does not overheat whilst in operation; the cryostat cannot work without it.
3. Place top of cryostat chamber in place on top of cryostat.
4. Ensure that vacuum pump air release valve is closed and then turn vacuum pump on, whilst also turning the Pirani gauge for the cryostat on. Once the pressure on the gauge displays below 4×10^{-2} torr, the cryostat can start being cooled. Note, the pressure will fall to this level within 5-10 minutes. This is a good opportunity to perform a room temperature IV sweep to confirm that the detector is working as expected, and that it is connected properly inside the cryostat.
5. The temperature controller can be turned on whilst waiting for the pressure to fall. The controller will display two temperatures, A and B. One of these reads the detector temperature, whilst the other reads the cold finger temperature.
6. When the pressure is correct, the cryostat can now be turned on to start the cooling process. It usually takes ~1 hour for the temperature to fall below 77 K. In standard configuration, the cryostat should be able to be cooled to below 30 K, although cooling to this temperature will take longer.
7. In order to stabilise the cryostat to a set temperature, it is recommended that the temperature is controlled by setting the cold finger temperature rather than the detector temperature, and using the “Med” heater setting on the controller. This will ensure a greater level of temperature stability. Note, the temperature will be controlled by the cold finger temperature, but it is the detector temperature which corresponds to the actual temperature of the measurement. At 77 K, the cold finger temperature will be ~10-20 K lower

than the detector temperature. As temperature increases, this difference reduces, with little difference between the temperatures above 200 K. For temperatures above ~160 K, the "High" setting on the temperature controller is required, otherwise the cryostat will stop warming up.

8. Once the temperature has stabilised, the measurement can be performed. The measurement can be repeated at different temperatures by setting the temperature controller accordingly. Note, it is recommended to start with the lowest temperature measurements first before moving onto higher temperatures, as this will save time with warming up the cryostat after the measurement.
9. When all the measurements are finished, the cryostat can be warmed up and the system shut down accordingly. It is possible to warm the temperature from 77 to 290 K in 10 minutes with the "High" setting, but this is not recommended. It is also possible to simply turn off the cryostat and temperature controller heater, and let it warm up over night. Alternatively, turn off the cryostat and set temperature controller to 290 K and use "Med" setting.
10. Once the cryostat is above ~285 K, turn off the temperature controller heater, pressure gauge and then vacuum pump. Note, ensure that the cryostat is definitely switched off, otherwise the temperature will start to fall again.
11. The pressure within the cryostat chamber needs to return to atmospheric levels before the chamber is opened and the samples retrieved. This usually takes 90 minutes, but this can be monitored by using the temperature controller. The temperature will generally fall back down to below 275 K, and then start rising again. Once above 285 K, it is safe to open the chamber and retrieve the sample. Alternatively, this can be left over night.
12. Once the pressure has returned to atmospheric levels, the air release valve can be opened, the samples removed and the temperature controller and water supply can be turned off.

Appendix D: Performing photocurrent measurements

This section outlines the procedure for performing photocurrent measurements using the setup displayed in Figure 3.3.

1. If performing cooled measurements, follow the procedure outlined in Appendix C for preparing the cryostat for use.
2. Whilst the cryostat is cooling, the blackbody source needs to be switched on, warmed up and allowed to stabilise. When the blackbody source is turned on at the plug socket, so is its fan. This fan is important to stop the blackbody source from overheating. Therefore, ensure that this fan does not get turned off during the measurement, otherwise there is a risk of damage to the blackbody source.
3. The temperature of the blackbody source can be set using the blackbody controller, with its current temperature shown on the display. It will take ~45 minutes for the temperature to warm up and stabilise at its set temperature. Note, this time will be longer if the blackbody source needs to be cooled to a significantly lower temperature.
4. For the photocurrent measurement, the spectrum analyser needs to be configured using the following settings:
    a. Measure – spectrum
    b. Span – 1.56 kHz
    c. Start frequency – 0 Hz
    d. Averaging – on, linear, 400 averages
    e. Seeks – peek
    f. Units – volt RMS
5. The optical chopper can be set to a specific frequency, e.g. 810 Hz. The "peak" on the spectrum analyser will correspond to the photocurrent, modulated at the chopper frequency.
6. In order to alter the gain of the pre-amplifier, the sensitivity setting on the pre-amplifier must be altered. Note, care needs to be taken with regards the to the bandwidth of the pre-amplifier and the chopper frequency to ensure that the measurement is taking place within the pre-amplifier's bandwidth. This

will be different for the “low noise” and “high bandwidth” settings for the pre-amplifier. See the SR570 user guide for more details.

7. The internal bias of the pre-amplifier is used to alter the bias voltage in the measurement up to ±5 V. However, if a greater bias voltage is required, a combination of 9 V batteries can be placed in series with the pre-amplifier as a low noise solution. The actual bias voltage applied to the detector can be monitored using a multi-meter.
8. The spectrum analyser can be replaced with a lock-in amplifier for performing photocurrent measurements, and has a lower noise floor.
9. At the end of the measurement, it is important that the blackbody source is allowed to cool sufficiently before the fan is turned off. This cool down time is generally 4-5 hours, but will be less when lower temperatures are used. A 24 hour timer is used at the plug socket, which will turn the fan off after a pin in the timer rotates to the top. When turning off the blackbody source, ensure that there is at least 5 hours left before the timer switches the fan off. Note, it is the position of the pin on the timer which dictates the time left, not the numbers. Also ensure that the pin’s position will not turn off the timer, and therefore the fan, during the actual measurement to avoid damage to the blackbody source.

Appendix E: Performing noise measurements

This section outlines the procedure for performing noise measurements using the setup displayed in Figure 3.3.

1. If performing cooled measurements, follow the procedure outlined in Appendix C for preparing the cryostat for use.
2. When performing the noise measurements, ensure that the shortest coaxial cables possible are used to reduce excess capacitance in the measurement.
3. For the noise measurement, the spectrum analyser needs to be configured using the following settings:
    a. Measure – PSD (power spectral density)
    b. Span – 100 kHz
    c. Start frequency – 0 Hz
    d. Averaging – on, linear, 400 averages
    e. Seeks – mean
    f. Units – volt RMS
4. The marker on the spectrum analyser should be in the centre of the screen to ensure that the 1/f noise region of the spectrum is not being measured.
5. The internal bias of the pre-amplifier is used to alter the bias voltage in the measurement up to ±5 V. However, if a greater bias voltage is required, a combination of 9 V batteries can be placed in series with the pre-amplifier as a low noise solution. The actual bias voltage applied to the detector can be monitored by using a multi-meter.

Appendix F: Performing spectral response measurements

This section outlines the procedure for performing spectral response measurements using the setup displayed in Figure 3.4. This is an "external" measurement for the FTIR.

1. If performing cooled measurements, follow the procedure outlined in Appendix C for preparing the cryostat for use.
2. Load the "Varian Resolutions Pro" software. Select "File", "New", "Multi-Spectral Document" to open a new document in which all the spectra from this measurement will be saved in raw data form.
3. Select "Collect" and then "Rapid-Scan" to start setting up the measurement parameters. Set the following for detector characterisation (external FTIR measurements):
    a) On the "Electronics" tab, select the following:
        i. Speed – 5 kHz
        ii. Filter – 1.2
        iii. UDR – 2
        iv. Resolution – 8 cm^{-1}
        v. Sensitivity – 1
        vi. Scans to collect – 128 (select fewer for a faster measurement, with less scans measured to be averaged)
    b) On the "Optics" tab, select the following:
        i. IR source – mid-IR
        ii. Beam – external
        iii. Detector – detector characteristics
4. Click "Setup" to reach the interferogram screen. If the "Interferogram" option on the right hand side of the screen is not selected, select it.
5. The beam from the FTIR now needs to be focused onto the detector inside the cryostat using a parabolic mirror. The parabolic mirror is specified for focusing upon a target 10 cm away, and is required to perform the measurement. Note, there will be a red laser spot from the FTIR which will be focused onto the detector. This is not the beam from the FTIR, but is

merely for guidance purposes. Its position does not correspond to the focused beam from the FTIR, and is in a different position.

6. Once the FTIR beam is incident upon the detector, an interferogram should appear on the screen. This needs to be maximised by adjusting the alignment of the FTIR beam on the detector. If the alignment improves during adjustment, the interferogram will get bigger. Note, the pre-amplifier may start overloading, making the interferogram disappear from the screen. This is due to the signal being too large for the selected sensitivity. If it does overload, increase the sensitivity setting until the interferogram reappears.
7. Once the alignment is optimised and the interferogram maximised, the measurement can take place. To do this, click "scan". The FTIR will then measure the data for the number of scans that has been selected for the measurement. This can be repeated at the required number of bias points.
8. The internal bias of the pre-amplifier is used to alter the bias voltage in the measurement up to ±5 V. However, if a greater bias voltage is required, a combination of 9 V batteries can be placed in series with the pre-amplifier as a low noise solution. The actual bias voltage applied to the detector can be monitored by using a multi-meter. Note, the sensitivity setting on the pre-amplifier should be noted down in order to relate the spectral intensity for spectra which use different sensitivity settings.
9. Once all the spectra have been collected, the data can be extracted, however this must be performed one spectra at a time. To do this, highlight the spectra inside the document, then click "File", "Export Spectrum" and then save it is a .csv file. This will produce a .csv file giving the spectral intensity as a function of wavenumber in cm^{-1}.

There are times when an "internal" measurement needs to be performed by the FTIR. This is generally used for measuring the transmission spectra of spectral targets, as well as the transmission of bandpass filters. Its measurement procedure is as follows.

1. Load the "Varian Resolutions Pro" software. Select "File", "New", "Multi-Spectral Document" to open a new document in which all the spectra from this measurement will be saved in raw data form.

2. Select “Collect” and then “Rapid-Scan” to start setting up the measurement parameters. Set the following for internal FTIR measurements:
    a) On the “Electronics” tab, select the following:
        i. Speed – 5 kHz
        ii. Filter – 1.2
        iii. UDR – 2
        iv. Resolution – 8 cm^{-1}
        v. Sensitivity – 1
        vi. Scans to collect – 32 (fewer measurement generally required for internal measurements)
    b) On the “Optics” tab, select the following:
        i. IR source – mid-IR
        ii. Beam – internal
        iii. Detector – mid-IR DTGS
3. Click “Setup” to reach the interferogram screen. If the “Interferogram” option on the right hand side of the screen is not selected, select it.
4. Open up the FTIR chamber, check there is nothing inside to block the internal FTIR beam. A scan should be performed for the empty FTIR chamber to measure the background to be removed from the measurement. To do this, click “scan”, and the FTIR will then measure the background response of the FTIR.
5. Open up the FTIR chamber and place in the object to be measured. Click “scan” to perform the measurement of the spectral transmission of the object. Repeat this for further objects if necessary.
6. The background needs to be removed from the measured spectral transmission of each object. For each transmission spectra, click on it and then click “Transforms”, “Ratio”. Search for the document containing the spectra, and single-click on it. On the right hand side of the window, click on the background spectra and click “Open”. This gives the absorbance spectra. To display the transmission spectra, click “Transforms”, “%Transmittance”.
7. Once all the spectra have been collected, with the background accounted for, the data can be extracted. However, this must be performed one spectra at a time. To do this, highlight the spectra inside the document, then click “File”,

"Export Spectrum" and then save it is a .csv file. This will produce a .csv file giving the spectral intensity as a function of wavenumber in cm^{-1}.

Appendix G: Transimpedance amplifier circuit

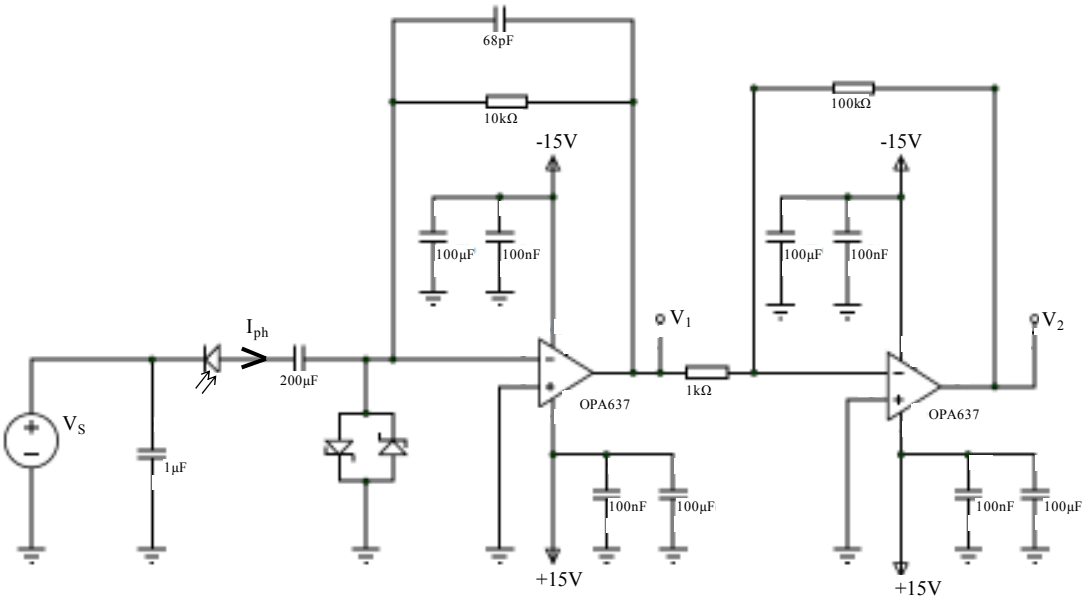

Figure A.1 – Transimpedance amplifier circuit discussed in section 3.3.1

Appendix H: Performing radiation thermometry measurements

This section outlines the procedure for performing radiation thermometry measurements using the setups displayed in Figure 3.8 and Figure 3.9.

1. If performing cooled measurements, follow the procedure outlined in Appendix C for preparing the cryostat for use.
2. The blackbody source needs to be switched on, warmed up allowed to and stabilise. When the blackbody source is turned on at the plug socket, so is its fan. This fan is important to stop the blackbody source from overheating. Therefore, ensure that this fan does not get turned off during the measurement, otherwise there is a risk of damage to the blackbody source.
3. The temperature of the blackbody source can be set using the blackbody controller, with its current temperature shown on the display. It will take ~45 minutes for the temperature to warm up and stabilise at its set temperature. Note, this time will be longer if the blackbody source needs to be cooled to a significantly lower temperature.
4. With the setup aligned accordingly, with the focusing lens aligned with the centre of the blackbody aperture, adjust the detector's position so that optimum alignment is found. Monitor the output voltage on the spectrum analyser to help with this alignment.
5. When fully aligned, the measurement can take place. Open Labview program "thermometry_PSD.vi" for PSD measurements. Under "Path", define the directory where the measurements will be saved, as well as the filename as a .csv or .txt file.
6. Make sure "GPIB" is selected as "8" to correspond to the lock-in amplifier, and set the "Settling time" as appropriate to the time constant used (generally > 5 times the time constant, therefore 5 s if a time constant of 1 s is used).
7. Click "Run" to start the program, and "Stop" to stop it. The number of sample points used is counted by the program under "Count".
8. The sampling rate of the program can be changed by going to "Operate", "Step into" and then adjusting the "time delay" in the program. The default setting is 50 ms, but this can be altered accordingly.
9. This can all be repeated at different blackbody temperatures.

10. At the end of the measurement, it is important that the blackbody source is allowed to cool sufficiently before the fan is turned off. This cool down time is generally 4-5 hours, but will be less when lower temperatures are used. A 24 hour timer is used at the plug socket, which will turn the fan off after a pin in the timer rotates to the top. When turning off the blackbody source, ensure that there is at least 5 hours left before the timer switches the fan off. Note, it is the position of the pin on the timer which dictates the time left, not the numbers. Also ensure that the pin's position will not turn off the timer, and therefore the fan, during the actual measurement to avoid damage to the blackbody source.

Appendix I: QDIP bias combinations

QDIP bias voltage combinations demonstrated in section 7.3.4 with optimised bias voltages for SWF and LWF individually.

Number of bias voltages	Bias voltages used for SWF	Bias voltages used for LWF
2	-9 and 9 V	-17 and -19.5 V
4	-9, -7, 7 and 9 V	-19.5, -17, 19, 21 V
6	-9, -8, -7, 7, 8, 9 V	-19.5, -17, -15, 17, 19, 21 V

Table A.1 – QDIP bias voltage combinations demonstrated for optimised bias voltages for SWF and LWF individually